

A Very Sensitive 21cm Survey for Galactic High-Velocity H I

Felix J. Lockman

*National Radio Astronomy Observatory¹, P.O. Box 2, Green Bank, WV, 24944;
jlockman@nrao.edu*

Edward M. Murphy

*University of Virginia, Department of Astronomy, P.O. Box 3818 University Station,
Charlottesville, VA 22903-0818; emm8x@virginia.edu*

Sara Petty-Powell

*The Evergreen State College, Physics and Astronomy, 2700 Evergreen Parkway NW,
Olympia, WA 98502*

and

Vincent J. Urick²

Bloomsburg University, Physics Department, 400 East 2nd St., Bloomsburg, PA 17815

ABSTRACT

Very sensitive H I 21cm observations have been made in 860 directions at $\delta \geq -43^\circ$ in search of weak, Galactic, high-velocity H I emission lines at moderate and high Galactic latitudes. One-third of the observations were made toward extragalactic objects that are visible at optical and UV wavelengths. The median rms noise in the survey spectra is 3.4 mK, resulting in a median 4σ detection level of $N_{HI} = 8 \times 10^{17} \text{ cm}^{-2}$ averaged over the $21'$ beam of the telescope. High-velocity H I emission is detected in 37% of the directions; about half of the lines could not have been detected in previous surveys. The median FWHM of detected lines is 30.3 km s^{-1} . High-velocity H I lines are seen down to the sensitivity limit of the survey implying that there are likely lines at still lower values of N_{HI} . The weakest lines have a kinematics and distribution on the sky similar to that of the strong lines, and thus do not appear to be a new population. Most of the

²Current address: Naval Research Laboratory, Optical Sciences, Code 5652, Building 215, Room 120, 4555 Overlook Ave. SW, Washington, D.C. 20375

emission originates from objects which are extended over several degrees; only a few appear to be compact sources. At least 75%, and possibly as many as 90%, of the lines are associated with one of the major high-velocity complexes. With the increased sensitivity of this survey, the Magellanic Stream is seen to extend at least 10° to higher Galactic latitude than previously thought and to be more extended in longitude as well. Wright’s Cloud near M33 has an extended low- N_{HI} component in the direction of the Magellanic Stream. The bright H I features which have dominated most surveys may be mere clumps within larger structures, and not independent objects. Although there are many lines with low column density, their numbers do not increase as rapidly as N_{HI}^{-1} , so most of the H I mass in the high-velocity cloud phenomenon likely resides in the more prominent clouds.

Subject headings: Galaxy:halo, structure – ISM:H I – Surveys – Magellanic Clouds

1. Introduction

Emission in the 21 cm H I line is seen over a large fraction of the sky at velocities $-500 \lesssim V_{LSR} \leq -100$ km s $^{-1}$ and $+100 \leq V_{LSR} \lesssim +400$ km s $^{-1}$: too large to arise solely from Galactic rotation, yet seemingly not part of the Hubble flow (see Wakker & van Woerden (1997) for a recent review; throughout this work we use the definition that high-velocity H I has $|V_{LSR}| \geq 100$ km s $^{-1}$ in directions where such velocities are not expected from Galactic rotation). These high-velocity clouds were discovered in the 21cm line of H I (Muller, Oort, & Raimond 1963), and for many decades the 21cm line was their primary spectral signature. Surveys of the sky in search of high-velocity H I are thought to be complete at the level of $N_{HI} \geq 2 \times 10^{18}$ cm $^{-2}$ for objects with an angular size of a degree or greater (Wakker 1991). The most prominent southern high-velocity clouds can be associated with the Magellanic Clouds (Mathewson, Cleary, & Murray 1974), and some high-velocity clouds lie in the Galactic halo (van Woerden et al. 1999), but the origin of most of the emission is unknown. It has been suggested that high-velocity clouds result from phenomena as diverse as extensions of the Galactic disk, material accelerated by supernovae or other energetic events, the remnants of a Galactic fountain, condensations in a Galactic halo, infall of debris from satellite galaxies, and objects in the Local Group of galaxies (Oort 1966; Habing 1966;

¹The National Radio Astronomy Observatory is a facility of the National Science Foundation operated under cooperative agreement with Associated Universities, Inc.

Davies 1972; Shapiro & Field 1976; Bregman 1980; Norman & Ikeuchi 1989; Blitz et al. 1999; Kalberla & Kerp 1999; Mallouris et al. 1999). It is probable that high-velocity clouds are a heterogeneous population and all of these possibilities are correct for different subsets of the data.

A number of high-velocity absorption lines have been detected in the ultraviolet toward extragalactic sources (e.g., Savage et al. (1993); Bowen & Blades (1993); Bowen, Blades & Pettini (1995); Lu et al. (1994); Murphy et al. (2000); Gibson et al. (2000)). The UV transitions are much more sensitive to small amounts of neutral gas than the 21cm line: a cloud with $N_{HI} = 10^{18} \text{ cm}^{-2}$ will produce strong Mg II absorption even if the metallicity is only 0.1 solar (Lockman & Savage 1995; Charleton, Churchill, & Rigby 2000). The statistics of the UV absorption lines suggest that high-velocity clouds are more abundant than would be expected from 21cm H I surveys (Savage & Sembach 1996). The extrapolation from the 21cm measurements to lower N_{HI} levels is always uncertain (Wakker 1991), and the UV results are based on relatively few sight lines, but these observations raise the interesting possibility that the Milky Way is surrounded by a mist of high-velocity gas with $N_{HI} \lesssim 10^{18} \text{ cm}^{-2}$ which has escaped detection in previous surveys. This is doubly interesting because the HI disks of other spiral galaxies are truncated at the level of a few 10^{19} cm^{-2} , presumably because of ionization by the extragalactic radiation field (van Gorkom 1991, 1993; Bochkarev & Syunyaev 1977; Maloney 1993; Corbelli & Salpeter 1993). This possible population of clouds with low N_{HI} might have a different distribution and different properties than the denser high-velocity clouds. It might also contain significant mass.

To try to bridge the gap between the sensitivities of the 21cm and the UV measurements, we began in 1992 a very sensitive 21cm H I search for high-velocity lines too faint to have been detected in previous 21cm surveys. Some results from the first third of the data have already been published (Murphy, Lockman, & Savage 1995). Since the beginning of this project there has been renewed interest in the high-velocity cloud phenomenon. There has been an extensive 21cm survey of the southern high-velocity cloud population (Putman et al. 2002). There has been a proposal that most of the clouds are members of the Local Group at a distance $\sim 1 \text{ Mpc}$ (Blitz et al. 1999), and another that some fraction of them are dwarf irregular galaxies which lack bright stars (Braun & Burton 1999, 2000). There have been investigations into the connection between high-velocity clouds and the neutral gas in the local universe (Charleton, Churchill, & Rigby 2000; Zwaan & Briggs 2000; Zwann 2001). While the data presented here bear somewhat on these issues, the main goal of this work has always been to investigate the high-velocity cloud phenomenon at low values of N_{HI} , and that aspect of the data is the focus of this paper.

2. Observations

2.1. Equipment

The observations were made with the 140 Foot (43m) Telescope of the NRAO in Green Bank, WV, during nineteen observing sessions between March 1993 and September 1996. The telescope has an angular resolution of $21'$ at the wavelength of the 21cm H I line. An HFET receiver was operated in dual circular polarization mode and had a total system temperature at zenith of about 20 K in each channel. The spectrometer was the NRAO Model IV 3-level autocorrelator, which provided a 512 channel spectrum in each polarization. Spectra were taken by position-switching using a 10 MHz bandwidth for a total velocity coverage $-1000 \leq V_{LSR} \leq +800$ km s⁻¹ and an effective velocity resolution of 5.0 km s⁻¹. About 100 of the directions were reobserved using frequency-switching at 2.5 MHz total bandwidth with an effective velocity resolution of 1.25 km s⁻¹ over 450 km s⁻¹. The good velocity resolution of the spectra insures that lines will always be present in several channels, minimizing the possibility that narrow-band interference would be mistaken for an actual H I feature.

2.2. Selection of Directions

Long integrations in search of faint high-velocity clouds can be done in any direction, though we wished to concentrate on moderate and high Galactic latitudes where the high-velocity clouds are most clearly distinguished from phenomena in the Galactic disk. One-third of the survey directions were toward extragalactic objects which are bright in the optical and UV, in the hopes that spectra at these wavelengths might someday be obtained to complement the radio data. These directions are listed in Table 1. Many bright QSOs and AGN have been observed in H I as part of another project (Murphy, Sembach, & Lockman, in preparation) and were not repeated here. Only a few of the sources have significant radio continuum emission, and none were strong enough, at the 140 Foot Telescope, to cause the H I to appear in absorption.

Each observation toward an extragalactic object was accompanied by two flanking observations, of similar sensitivity, in directions offset $\pm 6^m 52^s = \pm 1^\circ 7 \cos(\delta)$ in right ascension, making “triples” of measurements across the sky (some high-declination directions are offset by twice this amount). The flanking directions were used as reference spectra for position-switched observations, they provide independent samples of the high-velocity sky, and they give some indication of the angular size of detected lines. Directions are identified by the name of the extragalactic object, with the suffix “+” or “-” to show flanking positions. A

high-velocity line might be present in any or all of these spectra. The observations were made as far south as declination $-43^{\circ}3$; the median declination is $+17^{\circ}$. We emphasize that the H I lines detected in this survey have nothing to do with the background objects, most of which have a redshift well outside the velocity coverage of the survey.

2.3. Observational Procedure

The observations consisted of a basic cycle in which a total power HI spectrum was measured for 6 minutes at each direction of a triple: the “–”, source (S), and the “+” positions. This procedure was repeated at least six times for a total of no less than 36 minutes integration at each location. During data reduction, the total power spectra were combined to form position-switched pairs using each direction in a triple as either “signal” or “reference” with respect to the other two. This procedure effectively cancels all stray radiation in the spectra and much of the normal, low-velocity Galactic disk H I, and usually gives excellent instrumental baselines. The 6 minute integration period, together with the $6^m 52^s$ separation of the positions in right ascension, meant that the telescope tracked over the same azimuth and elevation for each position in a triple (when allowance for observing overhead is included) helping to insure good instrumental baselines. Previous surveys have used special “emission-free” directions for reference (Hulsbosch & Wakker 1988) or have modeled the bandpass (Barnes et al. 2001), but these techniques do not always give the very flat baselines needed to detect very weak lines. The disadvantage of using nearby reference positions, however, is that a high-velocity cloud may be extended over several degrees and thus cover all three locations of the triple. These situations were resolved by making frequency-switched measurements, or by choosing an alternate reference position as described below. In all, total-power H I spectra were measured in 860 directions, which sample a total area of 60 square degrees.

About 100 directions were observed in frequency-switched as well as position-switched modes. Some of the frequency-switched spectra were taken concurrently with the position-switched data, and others were taken subsequently to restore emission which extended over an entire triple. The frequency-switched spectra have integration times between 20 minutes and several hours. Unlike the position-switched spectra, the frequency-switched spectra can contain complete information on low-velocity H I, but they also contain stray radiation (§2.6).

2.4. Data reduction

The spectra were calibrated by bootstrapping to standard regions S6 and S8, and a correction for atmospheric opacity at 21cm was applied (Williams 1973). The frequency-switched spectra were corrected for stray radiation (see §2.6) using the method of Kalberla, Mebold, & Reich (1980) as applied to the 140 Foot Telescope by Murphy, Sembach, & Lockman (in preparation). A low-order polynomial was fit to the spectra to establish the instrumental baseline. The partial cancellation of strong, low-velocity Galactic H I emission in the position-switched spectra often produced ringing which was suppressed by smoothing with a Hanning function.

The position-switched spectra were examined for emission, and in cases where only one spectrum of a triple showed high-velocity lines, the other two spectra were combined into a single reference spectrum to reduce the noise. In many cases where high-velocity gas was detected at all locations in a triple, a frequency-switched spectrum was obtained in one of the directions and used to resolve ambiguities and restore the other two spectra.

Frequency-switched data were not available for all directions that had extended high-velocity emission, so it was sometimes necessary to rereduce the data using a reference spectrum taken many degrees away. Because most directions observed in this survey did not have detectable high-velocity H I, it was usually possible to find a set of suitable spectra taken on the same day for use as an alternate reference. A spectrum formed from an alternate reference, however, invariably has a poorer instrumental baseline than one formed from the members of the same triple.

H I emission at $|V_{LSR}| > 100 \text{ km s}^{-1}$ is found in two forms: spectral components well-separated from bright disk emission, and extended wings on the lower-velocity emission which cannot be described by a Gaussian function. We call these two cases “components” and “wings”. Occasionally a spectrum shows a clear H I component whose LSR velocity at the line peak is slightly less than the 100 km s^{-1} cutoff adopted as the definition of high-velocity gas. In this case we fit a Gaussian function to the line if it has significant emission at $|V_{LSR}| > 100 \text{ km s}^{-1}$ and if it is likely that the Gaussian parameters have physical meaning. Wings are characterized only by the first and zeroth moments of the velocity-weighted brightness temperature. Several lines were decomposed into multiple components when the peaks of the components were clearly resolved, if this procedure was reasonable given the noise in the data.

The quality of the data is generally excellent. There were a handful of spectra that showed some interference (see the example in §3.2), but it was usually so weak, narrow-band, and infrequent that it did not materially affect the measurements. The worst problems came

from occasional bad instrumental baselines caused when observations were made too close to the Sun, and, in one entire observing session, by a problem in one half of the autocorrelator which caused a kink in the baseline more than 100 km s^{-1} wide. In most cases no attempt was made to salvage the bad data, it was simply removed from the survey with the consequence that the affected directions had somewhat less sensitivity than the rest. A few spectra show residual effects of this problem.

2.5. Sensitivity and Detection Limits

The distribution of the rms noise in the emission-free baseline regions of the final position-switched spectra, which include both smoothed and unsmoothed data, is shown in Figure 1. The median value of σ_b is 3.4 mK. The long tail to high rms is caused by a few directions where radio continuum increased the total system temperature, a few directions with short integrations, and a few directions where the baseline quality was not good because of equipment problems or solar interference. Table 2 summarizes the parameters of the spectra, and gives the number of spectra in the final data set derived from each mode of observing. The frequency-switched spectra are not as homogeneous as the position-switched spectra because their integration times vary considerably. The factor of two difference between σ_b of the smoothed and unsmoothed frequency-switched data shown in Table 2 is a fluke caused by small numbers of smoothed spectra which included several very long integrations.

In order to determine our subjective ability to recognize weak lines in noisy spectra, simulated data were created containing Gaussian functions of random intensities at random velocities. These were analyzed as if they were real data. This effort showed that lines with a peak intensity $\geq 3\sigma_b$ were nearly always detected, and at this level there were virtually no noise features mistakenly identified as lines. We therefore assume that a line with $T_{pk} \geq 3\sigma_b$ in any spectrum is real. The lines detected in the survey under this criterion have peak brightness temperatures between 8 and 2052 mK with a median of 57 mK.

Although the simulations suggest that all lines with $T_{pk} \geq 3\sigma_b$ will be detected, to estimate the completeness of the survey we adopt a more conservative limit of $4\sigma_b$, which is $T_{pk} = 14 \text{ mK}$ for the median value of σ_b . A line of this peak brightness temperature whose width is 30 km s^{-1} has $N_{HI} = 8 \times 10^{17} \text{ cm}^{-2}$, and this value is therefore adopted as the median completeness level of the survey for emission which fills the antenna beam. A line at this brightness will be $\geq 3\sigma_b$ for more than 70% of the observations.

The survey is a factor of three to eight times more sensitive than that of Hulsbosch

and Wakker (1988), depending on whether the H I cloud being observed is larger than 35' or smaller than 21', respectively. The survey is a factor of 1.1 to 2 times more sensitive to broad lines than the Southern survey of Putman & Gibson (1999) for clouds with a size $< 15'$ and $> 21'$, respectively, and has a greater advantage for narrow lines, because the Southern survey used a relatively coarse velocity resolution of $\Delta v = 26.4 \text{ km s}^{-1}$, which will substantially dilute the peak signal in nearly half of the directions.

2.6. Stray Radiation as a Source of Error

Stray radiation is 21cm H I emission which is received through an antenna sidelobe, rather than through the main beam. The sidelobe may lie tens of degrees away from the direction that the telescope is pointed. Stray radiation can be a significant component of high-latitude 21cm spectra, and it often appears as spurious wings on a profile which may extend more than 100 km s^{-1} from the line center (e.g., Kalberla, Mebold, & Reich (1980); Lockman, Jahoda, & McCammon (1986)). Figure 2 shows a 140 Foot frequency-switched spectrum toward Ton 34 to illustrate the effect. The curve drawn through the data is an estimate of the stray component calculated using the method described by Murphy, Sembach, & Lockman (in preparation). In this spectrum, there is 2.4×10^{18} and $6.7 \times 10^{17} \text{ cm}^{-2}$ of stray emission at $V_{LSR} \leq -100$ and $V_{LSR} \geq +100 \text{ km s}^{-1}$, respectively.

Figure 3 shows the average amount of stray radiation that was removed from the ~ 100 frequency-switched observations in the survey, expressed as an equivalent N_{HI} integrated over $|V_{LSR}| \geq V'$ for various values of V' . The stray radiation at positive and negative velocities is distinguished by different symbols. In this sample, which should be typical of the northern sky, stray radiation is more significant at negative velocities because Galactic rotation produces a general preponderance of negative velocity H I at positive declinations, some of which leaks in through sidelobes to produce the stray wings. For a similar telescope in the southern hemisphere the proportions will most likely be reversed.

Stray radiation can mimic high-velocity H I at the level of a few 10^{18} cm^{-2} (the stray component at lower velocities can be orders of magnitude larger). The frequency-switched spectra in the survey were corrected by calculating the amount of stray radiation expected in each spectrum from a model of the all-sky response of the 140 Foot Telescope convolved with all-sky surveys of H I (Murphy, Sembach, & Lockman, in preparation). The calculated stray spectrum, which applies in a particular direction at a particular time, is then subtracted from the observed data. This technique has some limitations, for the far sidelobe pattern of a large conventional radio telescope cannot be determined to high precision, but it does reduce the effects of stray radiation in frequency-switched spectra by at least an order of

magnitude (e.g., Kalberla, Mebold, & Reich (1980)).

Sidelobes which are responsible for stray radiation are quite broad, so the stray component of H I spectra taken closely in position and time will be quite similar, and will be eliminated in the usual position-switching difference technique. But in directions where high-velocity gas is spatially extended, and the reference spectrum must be taken some distance away, cancellation of the stray radiation will not be complete. This may result in a residual which is either positive or negative at a given velocity. In our data, faint wings on spectra reduced with an alternate reference when there are no frequency-switched data should be viewed with caution. These are identified by the note “A” in the data table.

3. Results

3.1. The Data Table

Detections of high-velocity H I are summarized in Table 3. Directions are identified by the common name of the extragalactic source upon which they were centered, with a “–” or “+” suffix to indicate flanking directions in a triple. Thus the directions labeled Q 022+0015–, Q 022+0015, and Q 022+0015+ have $\alpha(B1950) = 00^h15^m18^s, 00^h22^m10^s,$ and $00^h29^m02^s,$ respectively, and all have essentially the same declination: $\delta(B1950) = +00^\circ15'44''$. The positions in the Table are those which were actually observed, and may differ from cataloged source positions by small amounts. Information in the Table is derived from unsmoothed, position-switched observations using a member of the same triple as the reference spectrum unless otherwise indicated. About 15% of the entries come from frequency-switched observations.

Line parameters were derived by fitting a Gaussian function. The line peak, T_{pk} , is a beam-averaged brightness temperature. Peak temperatures and widths are uncorrected for instrumental broadening, which can be significant for the narrowest lines (see §3.6). The error estimates on the line parameters (given in parentheses) are one standard deviation. The quantity σ_g is the rms of the Gaussian fit with respect to the data, and σ_b is the rms noise in the part of the spectrum used to determine the instrumental baseline. The quantities N_{HI} and $\langle V \rangle$ are described in §3.1.1. If a detected line could be associated with a known galaxy its name is given in the Table, and line parameters are listed without error estimates. These objects are discussed in §3.5.

The notes to Table 3 indicate if an alternate reference position was used for a position-switched spectrum (“A”), if the line parameters were derived from frequency-switched (“F”) or Hanning-smoothed (“H”) data, or if the detection is uncertain (“U”). Many of the “uncer-

tain” lines are wings near $\pm 100 \text{ km s}^{-1}$ on position-switched spectra that had to be reduced with an alternate reference position.

3.1.1. Description of Wings and other Components

Some spectra have emission at $|V_{LSR}| > 100 \text{ km s}^{-1}$ which is blended with lower velocity emission and cannot be described meaningfully by a Gaussian function. These blended lines will be called “wings”. Table 3 gives the zeroth and first moments of the wings, N_{HI} and $\langle V \rangle \equiv \int N_{HI}(v) v dv / \int N_{HI}(v) dv$, both calculated from $\pm 100 \text{ km s}^{-1}$ to a velocity where the emission becomes undetectable. The quantity $\langle V \rangle$ contains information on the shape of the wing past $\pm 100 \text{ km s}^{-1}$, and also, by its sign, shows the side of the profile on which the wing is found.

The N_{HI} and $\langle V \rangle$ columns in Table 3 are also used occasionally to describe H I emission in a spectrum which is not necessarily a wing, but cannot be modeled by a Gaussian function either. A specific example is discussed in §3.2. To distinguish this circumstance from a wing, the following convention has been adopted. If there is an entry for N_{HI} in Table 3 and no Gaussian parameters *in the same row*, this signifies that the entry is a wing whose N_{HI} has been counted separately from other components which may occur in that spectrum. For example, the spectrum labeled 4C 49.48+ described on rows 2 and 3 of Table 3 contains two spectral components: a Gaussian (row 2) and a wing (row 3). They are both at negative velocity. The total N_{HI} at $V_{LSR} < -100 \text{ km s}^{-1}$ in this direction is the sum of the N_{HI} in the two entries, or $1.35 \times 10^{19} \text{ cm}^{-2}$. If, however, a value for N_{HI} is given on a row which also contains information about a Gaussian component, then that value of N_{HI} includes the emission in the Gaussian, and in any other Gaussian which has the same sign of velocity. This circumstance is rarer, but occurs, for example, toward Mrk 380– in rows 86 and 87 of Table 3. Here the total N_{HI} on the negative velocity side of the line is $4.87 \times 10^{19} \text{ cm}^{-2}$, which includes the two Gaussian components, and additional emission not contained in either. The spectrum in this particular direction is illustrated in §3.2 and discussed further there.

3.1.2. Table of Gaussian Components

The lines detected in this survey that are well described by a Gaussian function are given in Table 4. The H I column density N_{HI} was calculated under the optically thin assumption: $N_{HI} = 1.823 \times 10^{18} T_{pk} 1.065 \Delta v$. It includes all emission in the component, even that which

lies at $|V_{LSR}| < 100 \text{ km s}^{-1}$. Table 4 contains no line wings or other components which could not be represented by a Gaussian, and it does not contain lines that are associated with known galaxies or galaxy groups.

3.2. Sample Spectra

The spectra shown in Figures 4, 5, and 6 illustrate the types of H I lines that have been detected. Only the central velocities of the spectra are shown.

Figure 4 shows position-switched data containing some of the weaker lines detected in the survey. The lower two spectra have been Hanning smoothed. The spectrum in the upper panel contains two blended high-velocity H I lines near -300 km s^{-1} and the Gaussian functions that were fit to them. The lines have $N_{HI} = 8.3 \times 10^{17}$ and $1.5 \times 10^{18} \text{ cm}^{-2}$. Position-switching to a nearby reference has canceled most emission at $|V_{LSR}| < 100 \text{ km s}^{-1}$.

The spectrum in the central panel of Fig. 4 has emission from a high-velocity cloud at $V_{LSR} \approx -400 \text{ km s}^{-1}$, together with a double-peaked H I line from the galaxy UGC 64 which serendipitously lies in this direction at $+300 \text{ km s}^{-1}$. Low-velocity H I emission is confused because of cancellation in the position-switching, but the negative signal near $V_{LSR} \sim -100 \text{ km s}^{-1}$ is actually an emission wing in the reference spectrum (4C 40.01+), with a total $N_{HI} = 2.5 \times 10^{18}$ between -150 and -100 km s^{-1} (see row 10 of Table 3). The lower panel of Figure 4 shows a spectrum with a high-velocity H I line at -327 km s^{-1} that has $\Delta v = 30 \text{ km s}^{-1}$, the median width of the lines detected in this survey.

Figure 5 shows two Hanning smoothed, position-switched spectra from the survey which illustrate profile wings and emission which cannot be described by a Gaussian function. The spectrum in the upper panel has a line at $+145 \text{ km s}^{-1}$ with $N_{HI} = 1.25 \times 10^{18} \text{ cm}^{-2}$. It has $\Delta v = 23 \text{ km s}^{-1}$, and is well separated from the rest of the emission. This spectrum also contains a second component whose peak is near $+85 \text{ km s}^{-1}$ with an extension past $+100 \text{ km s}^{-1}$. This line may have been partly canceled in the position-switching, so its true shape is uncertain, and it is listed in Table 3 as a wing. The total N_{HI} at $V_{LSR} > 100 \text{ km s}^{-1}$ in this direction is the sum of the wing (Table 3 row 205) and the Gaussian component (row 206). This spectrum also shows some residual instrumental baseline structure at positive velocities.

The lower panel of Figure 5 shows a more complex spectrum. The high-velocity H I in this part of the sky extends over many degrees, so reference spectra were chosen from a triple that was about 12 degrees distant. The spectrum is thus noted “A” in Table 3. The two Gaussians fit to the data give a reasonably accurate representation of much, but by no

means all, of the high-velocity emission. While a third Gaussian component could have been fit near -240 km s^{-1} , its properties would not have been well constrained, so a total integral for all the emission at $V_{LSR} < -100 \text{ km s}^{-1}$ was calculated instead and is given in row 86 of Table 3. In the convention adopted for Table 3, whenever a value for N_{HI} is listed in the same row as a Gaussian component, that component, and all others on the same side of the profile, are included in the value of N_{HI} . Thus the total N_{HI} at negative velocities toward Mrk 180– is $4.87 \times 10^{19} \text{ cm}^{-2}$, comprised of two Gaussians and the additional emission (see §3.1.1).

Figure 6 shows representative frequency-switched spectra after their correction for stray radiation. The top spectrum is unsmoothed at a channel width of 1.25 km s^{-1} and has $\sigma_b = 42 \text{ mK}$. The component shown with the Gaussian fit is listed in Table 3 even though its velocity at line peak is only 84 km s^{-1} , because much of it lies at $V_{LSR} < -100 \text{ km s}^{-1}$ and it is well separated from normal Galactic disk H I.

Spectra in the lower three panels of Fig. 6 were taken $\pm 0^\circ.8$ on either side of, and toward, the galaxy Markarian 205. The high-velocity line toward Mrk 205– has a width $\Delta v = 14.6 \text{ km s}^{-1}$ and the spectrum shows a rare example of radio interference near $+40 \text{ km s}^{-1}$. The high-velocity H I seen directly toward Mrk 205 has been decomposed into two Gaussians with $\Delta v = 7.1$ and 18.0 km s^{-1} . This direction provides an example of the multiple component (core-halo) structures found in some high-velocity spectra (Cram & Giovanelli 1976). The spectrum toward Mrk 205+, the only one in this Figure which is Hanning smoothed, contains a weak line with $\Delta v = 4 \text{ km s}^{-1}$, the narrowest in this survey. Even narrower lines have been observed in this particular high-velocity cloud at an angular resolution of one arcmin (Braun & Burton 2000). The emission feature at -140 km s^{-1} in the Mrk 205+ spectrum may be an artifact of the stray-radiation removal process as it could not be detected in the more sensitive position-switched data. There are several features in other frequency-switched spectra that may also be artifacts of stray radiation. They are not included in the data tables.

3.3. Observed Directions

Although some directions as far south as $\delta = -43^\circ.3$ have been observed, southern declinations are undersampled compared to northern declinations. The distribution of the observations in Galactic latitude is shown in Figure 7, with a curve proportional to the amount of sky at each latitude with $\delta \geq -30^\circ$. The curve is a reasonable approximation to the distribution except at $|b| < 20^\circ$, where there are fewer observations than would be found in a uniform sample. This is a consequence of our observation toward UV and optically

selected extragalactic targets, which are unlikely to be found in directions of high extinction and thus avoid the Galactic plane.

3.4. Notes on Specific Spectra

Table 3 includes lines in three directions (rows 58, 377, and 378) which have $T_{pk} < 3\sigma_b$ and therefore fall below our limit for a claimed detection. They all have $T_{pk} \approx 7$ mK and values of N_{HI} in the range $4 - 6 \times 10^{17}$ cm⁻², among the lowest in the survey. Although these lines are not used in any analysis, they appear to be real and have been included in the Table.

Table 3 also contains three lines with $T_{pk} > 3\sigma_b$ which we suspect are spurious, likely to be an instrumental artifact of some undetermined sort, even though they are above our detection limit. These have the smallest values of N_{HI} in the survey. Two of the lines are toward Mrk 992 (rows 38 and 39). With LSR velocities of -492 and $+465$ km s⁻¹, these have the second most negative, and the most positive, velocity of any line in the entire survey. The positive velocity line lies almost 200 km s⁻¹ beyond the next-highest velocity line, and it sits in an area of longitude-velocity space occupied only by galaxies that are part of the Hubble flow (see §4). It strikes us as improbable that one spectrum should contain two such extreme lines, and such weak lines, though scrutiny of the data gives us no reason to reject them outright.

The line toward PKS 0859 – 14+ (row 128) has $V_{LSR} = -696$ km s⁻¹. This is almost 200 km s⁻¹ more negative than our secure detections, and, at $T_{pk} = 10.3$ mK and $N_{HI} = 3.8 \times 10^{17}$, the line is among the weakest in the survey. Moreover, most high-velocity H I at its longitude and latitude has positive LSR velocity, not negative. Examination of the raw data, however, give us no reason to reject this line and it has been kept in the survey.

The nominal limit for detection of a line, $T_{pk} > 3\sigma_b$, was relaxed for one line in the group from 4C50.43– which has $T_{pk} = 2.8\sigma_b = 3.1\sigma_g$. This direction was observed using frequency-switching, the line appears in many channels, and it is most likely real.

3.5. Galaxies

In at least twelve directions H I lines were detected which can be attributed to a known galaxy in the antenna beam (this does not count the Magellanic Stream, which is discussed in §6.1). The galaxy M31 was detected in two separate spectra. An example of H I emission from a galaxy is shown in Figure 4. In Table 3, galaxies are identified by a note and their

peak line temperature and velocity are estimated directly from the data, not from a Gaussian fit. For galaxies, the approximate total velocity extent is given in place of Δv , and, to avoid any possible confusion with high-velocity clouds, the errors on the measured quantities are set to zero. Lines from galaxies are not included in any analysis of the survey results.

It is also likely that gas in the M81/M82 system was detected in the survey. The three directions associated with 0959 + 68W1 lie along the southern edge of the M81/M82 group, which contains several gas-rich galaxies as well as H I distributed throughout the group, probably the result of a tidal interaction (Appleton, Davies, & Stephenson 1981; Yun, Ho, & Lo 1994). We detect H I in the direction of 0959+68W1+ at the edge of the galaxy group, implying that gas in the group is more extensive than was previously known at the level of a few 10^{18} cm^{-2} .

3.6. Line Width

The distribution of measured line widths is shown in Figure 8, after correction for the channel width of the spectrometer. The median corrected value, $\Delta v = 30.3 \text{ km s}^{-1}$, is marked with an arrow. There is no correlation between Δv and the quantities V_{LSR} , Galactic latitude, or signal-to-noise ratio of the line. There is a tendency for the broadest lines to have a lower peak antenna temperature than the average. Some of the the broadest lines are probably blends of separate emission clouds in the antenna beam (see also Mirabel (1981); Braun & Burton (2000)). Many of the narrow lines would have been substantially diluted in some previous surveys made at a velocity resolution of $15\text{--}20 \text{ km s}^{-1}$, leading to a significant undercounting of this component of high-velocity gas.

Only 1% of the lines detected here have a width $\leq 10 \text{ km s}^{-1}$. Colgan, Salpeter, & Terzian (1990), in observations with a $4'$ beam, found that 6% of their lines were this narrow, and that they originated in localized regions of median size $\sim 10'$. This suggests that narrow lines may be underrepresented even in the current observations because of beam smearing.

4. The Sky Coverage of High-velocity H I

4.1. All High-Velocity H I

The goal of this survey was to determine the fraction of the sky which is covered by high-velocity H I. Figure 9 shows an Aitoff projection in Galactic coordinates, with solid symbols

marking directions with detected high-velocity gas, either Gaussian components or wings, and open circles marking directions with no detection. The organization of the observations into “triples” is apparent here, as is the zone of avoidance along the Galactic equator and the region at high longitudes which is below the horizon at Green Bank. Figure 10 shows the detections divided into wings and Gaussians components, where the wings are emission lines blended with lower-velocity gas. Some of the wings lie at distinctly low latitude and may be extensions of the Galactic disk rather than emission from discrete clouds.

Figure 11 shows the percent of the sky covered by high-velocity H I as a function of $\log(N_{HI})$. For this accounting, the total amount of H I at $|V_{LSR}| > 100 \text{ km s}^{-1}$ in each spectrum was summed over both positive and negative velocity, and the normalization is the total number of directions observed. The arrow marks the adopted median completeness limit of the survey, $8 \times 10^{17} \text{ cm}^{-2}$. For comparison, the dashed lines show the percentage sky coverage from the Hulsbosch & Wakker (1988) survey, derived from the statistics on peak line temperatures of Wakker (1991), under the assumption that the lines in that survey had $\Delta v = 30.3 \text{ km s}^{-1}$, the median from our survey. The nominal completeness level of the Hulsbosch & Wakker (1988) survey is $2 \times 10^{18} \text{ cm}^{-2}$, shown by a dashed arrow. The Wakker compilation does not include any emission from the Magellanic Stream, which, from our data, would add $\sim 4\%$ to the total area under the dashed curve.

There is general agreement between the Hulsbosch-Wakker data and the current survey for $N_{HI} \geq 6 \times 10^{18} \text{ cm}^{-2}$, but below this level we have found many H I lines that are too weak to have been detected before. Our data are consistent with a constant number of high-velocity H I lines, per logarithmic interval in N_{HI} , from $10^{18.6} \text{ cm}^{-2}$ down to the sensitivity limit of the survey, and the sudden decrease in the number of lines at that limit suggests that there may be many high-velocity H I clouds at even lower N_{HI} .

Of the 860 directions observed, 37% (316), show some high-velocity H I. There are 242 directions, or 28% of the total, that have high-velocity H I which can be characterized by a Gaussian component well-separated from the disk emission. If the abundance of high-velocity lines in the decade of N_{HI} below the completeness limit is similar to that in the decade above the limit, it would imply that about 60% of all sight-lines on the sky will intersect a high-velocity H I cloud with $N_{HI} \geq 10^{17} \text{ cm}^{-2}$.

4.2. The Gaussian Components

The 309 high-velocity H I lines in the survey that were fit with Gaussian functions come from 242 directions. The distribution of their column densities (from Table 4) is shown

in Figure 12 with a solid curve for all the data and a dashed curve for only the higher velocity lines. To first order, the curves are simply scaled copies of each other, suggesting that there is no strong relationship between the velocity of lines and their N_{HI} . This topic is discussed further in a following section. Table 5 summarizes the measured values of N_{HI} for the components. A given direction will contribute more than once to Table 5 if it contains multiple lines (§5.3). The median N_{HI} of the Gaussian high-velocity lines is $3.5 \times 10^{18} \text{ cm}^{-2}$.

5. Kinematics of High-velocity Gas

5.1. Kinematics of the Components and Wings

Figure 13 shows the velocity of the lines, wings and galaxies as a function of longitude. The upper panel shows V_{LSR} , and the lower panel shows velocities with respect to the Galactic center, where $V_{GCSR} \equiv V_{LSR} + 220.0 \sin(l) \cos(b)$. In general, the galaxies (marked with open stars) are part of the Hubble flow and occupy a different place in this diagram than most high-velocity clouds. A significant part of the LSR velocity of high-velocity gas arises in the rotation of the Galaxy, as shown by the more even distribution of points about zero V_{GCSR} than about zero V_{LSR} . The appropriate velocity reference frame for high-velocity H I will be considered further in the next section.

Figure 14 shows the LSR velocity of the galaxies and the Gaussian high-velocity components from Table 4 vs. their total hydrogen column density. The weakest lines have velocities similar to the stronger lines, though no line with $N_{HI} > 10^{19.5} \text{ cm}^{-2}$ has a very high velocity. Not too much weight should be placed on the three points with the lowest N_{HI} , as their accuracy is suspect (§3.4). Previous surveys have found that high-velocity H I is confined within $-465 \leq V_{LSR} \leq +420 \text{ km s}^{-1}$ (Wakker 1991; Morras et al. 2000). The current detections, with the exception of a few suspect lines, lie within the same range, indicating that the newly-discovered faint high-velocity H I lines are not a kinematically distinct population, but have the same general velocity bounds as the brighter lines.

Negative velocities dominate our detections, in part because of selection effects – many known high-velocity clouds with positive velocity are at very negative declinations below the survey limit – but also because there are a number of lines with large negative velocity around longitude 100° . Many of these arise in the Magellanic Stream.

5.2. Kinematics of the Integrated Emission

The upper panel of Figure 15 shows a composite spectrum made by summing all the emission in the Gaussian components from Table 4. The vertical dashed lines mark the limit of the definition of high-velocity gas in the LSR frame. This Figure does not include the emission in wings, so it is incomplete near ± 100 km s⁻¹, but apart from this, it is directly proportional to the likelihood of observing high-velocity H I at a given LSR velocity in the northern sky as determined by the survey data. The cross shows the mean velocity of the emission and $\pm 1\sigma$. In these data negative LSR velocities are dominant and the emission extends to a much greater negative than positive LSR velocity. The two lower panels show the emission summed in the Galactic Center Standard of Rest (defined in the previous section) and in the Local Group Standard of Rest: $V_{LGSR} \equiv V_{GCSR} + 40\sin(\ell)\cos(b) - 62\cos(\ell)\cos(b)$ km s⁻¹ (Braun & Burton 1999).

High-velocity H I emission in the northern sky is predominantly at negative LSR velocities, but when the components are averaged with respect to the Galactic Center, they are remarkably symmetric, with a mean velocity near zero and a substantially reduced dispersion. The extreme velocities have nearly identical magnitude. When the emission is further reduced to the Local Group Standard of Rest it has a somewhat broader extent and is skewed to positive velocity. Table 6 gives the mean and standard deviation of the composite spectra and also the mean and standard deviation of the H I line velocities with no weighting by the amount of H I in the line. Unlike the total emission, the velocities of the line peaks have a negative mean in all three reference systems.

It has been known for some time that the Galactic Center standard of rest is more appropriate for high-velocity H I than the LSR (Giovanelli 1980; Wakker 1991). There have been recent suggestions that the Local Group Standard of Rest is even more appropriate, in that the mean velocity of a selected group of high-velocity clouds is nearer zero, and their dispersion about the mean smaller, in that system (Blitz et al. 1999; Brüns et al. 2000; Braun & Burton 2000). The integrated emission, which we believe is a more robust indicator than counts of lines or clouds, does not support the Local Group Standard, and indicates that the GCSR system is preferred (see also the analysis of a different population in Putman et al. (2002)). In the GCSR system, the integrated emission has a mean velocity near zero and a dispersion smaller than in the other two systems.

5.3. Directions with Multiple Components

Some of the sample spectra shown in Figures 4, 5, and 6 contain several high-velocity H I lines. In the entire survey, 180 directions have a single line, 57 (or 24%) have two, and 5 have three, not counting wings. The separation of these components in velocity is shown in Figure 16. The median separation is 48 km s^{-1} , similar to the separation of the two lines in the upper panel of Fig. 4. Given that the median value of the linewidth is 30 km s^{-1} , many of the blends would not be resolved at a velocity resolution much coarser than that used here. The location of directions with multiple lines is shown in Figure 17. Most multiple lines do not seem to be chance superpositions of unrelated clouds, but are found toward high-velocity complexes such as Complex A and the Magellanic Stream, and reflect their internal velocity structure (e.g., Mirabel (1981); Wayte (1989); Murphy et al. (2000); Richter et al. (2001)).

The H I lines from some high-velocity clouds have two components at a similar velocity, one broad and one narrow (Cram & Giovanelli 1976; Braun & Burton 2000). This has been interpreted as evidence for a core-halo thermal structure in the clouds (Ferrara & Field 1994; Wakker & van Woerden 1997). Lines like this are rare in the survey. They would be listed as multiple components with a very small velocity separation; as Fig. 16 shows, this is seen in only a few percent of the spectra. The best core-halo example is Mrk 205 (Fig. 6), which has been studied at high angular resolution by Braun & Burton (2000).

6. Association with High-Velocity Cloud Complexes

The high-velocity H I sky is dominated by large complexes that have ordered velocities over large areas (Giovanelli 1980; Wakker & van Woerden 1991). Some complexes, like the Magellanic Stream (MS) and Complex C, are certainly physical associations with a distinct pattern of abundances and likely a single origin (e.g., Richter et al. (2001)). Others, like the Outer Arm (OA) complex, may be part of the Galactic warp (Habing 1966; Davies 1972; Verschuur 1975; Haud 1992). Some high-velocity clouds have been grouped into broadly-defined “populations” such as those at “extreme-negative” (EN) or extreme positive velocities (Wakker & van Woerden 1991), which may be merely collections of unrelated objects.

All of the Gaussian components of Table 4 have been examined for their possible association with a known high-velocity H I complex using the definitions of Wakker & van Woerden (1991) as a guide, and the results are given in the final column. There is some ambiguity in the identifications because the boundaries of the complexes are not sharp, and

are not well known at the sensitivity limits of the survey. Lines from a “population” are identified (parenthetically), but for statistical purposes are not included with lines from the complexes. The upper panel of Figure 18 shows the high-velocity H I lines detected in this survey coded by velocity interval, illustrating their association with large complexes. There is a high probability of membership in a complex for 232 of the 309 lines, or 75%, while for another 47 lines (15%) an association is possible.

The lower panel of Figure 18 shows lines detected in the survey which could not be assigned to a complex, and Figure 19 shows V_{LSR} vs. N_{HI} for the lines from Table 4, where open symbols are used to mark lines not obviously associated with a known high-velocity H I complex. The vast majority of lines at all values of N_{HI} are associated with a complex. The lines not in complexes do not have peculiar kinematics, and are distinguished mainly in that they have lower N_{HI} than the average. There are indications in our data that many complexes are more extensive than previously suspected. Several specific examples are discussed below.

6.1. An Extension of the Magellanic Stream

The dominant feature of the southern high-velocity H I sky is the Magellanic Stream. It has been studied by Mathewson and many others (Mathewson, Cleary, & Murray 1974; Haynes 1979; Mirabel 1981; Morras 1985; Wayte 1989; Putman 2000). The Magellanic Stream is a coherent structure extending more than 100° across the sky from the Magellanic clouds. Figure 20 shows the survey data for $b \leq 0^\circ$ with emphasis on the Stream. It has been proposed that nearly all of the very negative-velocity emission below the Galactic plane at these longitudes comes from the Stream (Mirabel 1981), although we have not made this assignment in Table 4. Filled stars show lines that are noted “MS*” in Table 4. These lie beyond the traditional borders of the Stream but are most probably an extension of it, in view of the location and kinematics of the lines and the recent theoretical work on the expected extent of the Stream (Gardiner & Noguchi (1996); Gardiner (1999) and references therein).

A number of the lines which we believe are part of the Stream lie on the same great circle as the main feature, but about 10° past its traditional tip near $b = -40^\circ$ (Wayte 1989). The lines typically have an N_{HI} of a few 10^{18} cm^{-2} . Other filled stars in Fig. 20 mark a group of lines possibly part of the Stream at a similar latitude but higher longitude than the main section. They have the very high negative velocities characteristic of the Stream, and theoretical models suggest that the Stream may be distended in this direction (Gardiner 1999). Lines which are suggestive of the Stream because of their location and high negative

velocity are marked “MS?” in Table 4 and shown as open stars in Fig. 20.

There are directions near the MS where we find no high-velocity H I emission at all (Fig. 9), but there is other evidence which suggests that the Stream may have considerable extent at levels below our sensitivity limit. Toward PKS 0003+15 at $\ell, b = 107^\circ 3 - 45^\circ 3$ (entry 128 in Table 4) we find a line with the velocity of the MS, but somewhat outside its traditional borders. About 5° away, Gibson et al. (2000) have detected Mg II in absorption at a similar velocity toward the galaxy III Zw 2, also in our survey, but that direction does not have high-velocity H I emission to a beam-averaged 3σ limit of $N_{HI} = 4.5 \times 10^{17} \text{ cm}^{-2}$ for an assumed line width of 30 km s^{-1} . This implies an abundance ratio $N_{MgII}/N_{HI} \leq 2 \times 10^{-5}$, and $[\text{Mg II}/\text{H I}] \geq -0.22$ for the Magellanic Stream in this direction, using solar abundances from Anders & Grevesse (1989). This abundance is consistent with that of the LMC and marginally consistent with the SMC, but the need for a correction for ionization or dust depletion, the possibility of substantial angular structure in the H I, and the fact that the H I column is only an upper limit, make interpretation of this ratio problematic (see Gibson et al. (2000)). Higher angular resolution 21cm H I observations toward III Zw 2 are needed to resolve this issue, but in any case, the Magellanic Stream probably covers considerably more area than even our measurements suggest.

A leading arm stretching out from the Magellanic Clouds opposite the Stream has been discovered (Putman et al. 1998; Putman 2000). Its extent is not yet certain, but there have been suggestions that it encompasses most of the positive-velocity emission in complex WD and population EP because of the kinematics and metallicity of the gas (Mathewson, Cleary, & Murray 1974; West et al. 1985; Lu et al. 1994, 1998; Sembach et al. 2001).

6.2. An Extension of Wright’s Cloud near M33

Wright’s cloud was discovered in H I emission close to galaxy M33. It covers more than 5° in right ascension at velocities near -400 km s^{-1} (Wright (1974, 1979), see also Fig. 5 of Blitz et al. (1999)). This object has been detected in the survey (noted ‘Wr’ in Table 4) up to $3^\circ 5$ beyond the known boundaries of the cloud, suggesting that it is extended to lower right ascension (and lower Galactic longitude) at levels $N_{HI} \leq 2 \times 10^{18} \text{ cm}^{-2}$. Some of the weak lines have the same multi-component structure found in the strong lines, and their velocity varies almost linearly with position, merging smoothly with the velocity of the main cloud. Thus Wright’s cloud, like the Magellanic Stream, has a significantly increased extent at low column densities. With the new data, the linear size of this cloud is $> 0.15 d$ kpc, where d is its distance in kpc. If it is at the distance of M33, it must be more than 100 kpc across.

Wright’s cloud has a velocity similar to parts of the Magellanic Stream $\sim 25^\circ$ away, but differs in velocity from the extension of the Stream which lies closer and at a more similar Galactic latitude.

6.3. Complex L

Complex L is a small group of clouds lying in a line near $\ell, b = 347^\circ + 34^\circ$ (Wakker & van Woerden 1991). We have detected H I with a similar latitude and V_{LSR} at several positions about 10° away in longitude. This emission is quite distinct from the other H I in the area. The lines all have $N_{HI} \leq 4 \times 10^{18} \text{ cm}^{-2}$ and are listed as “L?” in Table 4.

6.4. The Edges of the Complexes

Figure 21 shows the distribution on the sky of the Gaussian high-velocity lines divided at the median $N_{HI} = 3.5 \times 10^{18} \text{ cm}^{-2}$ into high- N_{HI} and low- N_{HI} groups. No distinction is made for the velocity of the lines. In many instances the low- N_{HI} lines cluster around their brighter counterparts suggesting that they trace the indistinct edges of the dense concentrations. This is particularly true for the Magellanic Stream ($60^\circ \lesssim \ell \lesssim 120^\circ; b \lesssim -30^\circ$), but is also seen in the W Complexes, and Complexes C, A, and M as well. One conspicuous exception is the Outer Arm (OA) Complex where 95% of the lines are quite bright at $N_{HI} > 10^{19} \text{ cm}^{-2}$, and no lines have $N_{HI} < 2 \times 10^{18} \text{ cm}^{-2}$. This lends weight to considerations that the OA Complex is not properly part of the high-velocity cloud phenomenon, but is somehow part of the warped Galactic disk (e.g., Habing (1966); Haud (1992)).

7. Angular Structure of the Emission

7.1. Nature of the low- N_{HI} Lines

Do the weakest lines in the survey result from beam dilution of small, bright H I clouds, or do they actually arise in broadly-distributed low- N_{HI} gas? A definitive answer cannot be supplied from the survey data alone, but there are suggestions that both circumstances are being observed. Table 7 lists some representative directions where a high-velocity H I line has been detected in all three position of a triple, and at least one direction has $N_{HI} \leq 2.0 \times 10^{18} \text{ cm}^{-2}$. The angular separation between each of the measurements is given in the last column. The first four entries in the Table show strong gradients in the observed N_{HI} , suggesting that

the lowest values might arise from beam smoothing, e.g., at the sharp edge of a bright cloud. This is already known to the case for Mrk 205, where high angular-resolution measurements show H I concentrations of 10^{21} cm^{-2} with sizes of a few arc-min (Braun & Burton 2000).

The final four entries in Table 7 show more modest variations in N_{HI} with angle, and there are directions, e.g., toward B2 0051+29, which give the impression of an extended region of low column density. This behavior is the rule rather than the exception in our survey. If a line is seen at two adjacent positions in a triple and one has $N_{HI} \leq 2 \times 10^{18} \text{ cm}^{-2}$, then the majority of the time its neighbor will have $N_{HI} \leq 4 \times 10^{18} \text{ cm}^{-2}$. Directions with low N_{HI} are most often found near other directions with low N_{HI} . The examples of extended low- N_{HI} emission come from several complexes indicating that the phenomenon is not an isolated one.

7.2. Angular Extent of the Emission

The data in each triple can be used to make generalizations about the angular extent of the objects detected in the survey. For each Gaussian in Table 4, we examined adjacent directions to see if emission was present at a similar velocity. After eliminating lines which might be confused with nearby wings, the survey gives some information on angular size for 163 emission lines. The results are summarized in Table 8, which shows how often high-velocity emission is extended over several positions in a triple. About 40% of the lines are seen at more than one position, and only 7% arise from objects which appear isolated in the survey data, in that they are found only at the center position of a triple and not at the edges. These are candidate compact high-velocity clouds (Braun & Burton 1999) and are listed in Table 9. Most are associated with complexes and thus are probably knots in larger clouds, and not isolated, compact objects.

Lines seen only at the edge of a triple, i.e., at either the ‘+’ or ‘-’ positions, are three times more frequent than lines seen only at the center position. This suggests that the vast majority of the lines detected in this survey come from objects whose extent is more than a few degrees. This is consistent with the results of Colgan, Salpeter, & Terzian (1990), who measured a number of high-velocity clouds and found a median size $\sim 2^\circ$ down to a few 10^{18} cm^{-2} .

8. Mass

The mass of high-velocity gas is uncertain because of our ignorance of the distance to most of the complexes, but it is possible to estimate the relative importance of the faintest lines to the total. The mass of an H I cloud has the proportionality $M \propto N_{HI}\Omega d^2$ where Ω is the solid angle and d is the distance. The high degree of association of the low N_{HI} lines with the giant complexes, both in kinematics and spatially, suggests that there is no relationship in general between N_{HI} and d , i.e., that the faint lines are located at the same distance as the bright lines which define the traditional complexes. The survey data do not give reliable estimates of Ω , but we will assume that the angular size is proportional to the frequency of occurrence of lines in the survey. The incremental H I mass in a range of column density is thus proportional to the total number of lines detected in that range times the average column density: $M_i \propto n\langle N_{HI} \rangle_i = \Sigma N_{HI_i}$. This quantity is given in Column 4 of Table 5, and is expressed as a percentage of the total N_{HI} in Column 5. Each interval of N_{HI} above 10^{19} cm^{-2} makes a significant contribution to the total (see also Putman (2000a)), but below this, the number of lines does not increase as fast as N_{HI}^{-1} , and their contribution to the total mass becomes insignificant.

Figure 22 shows the cumulative distribution of the numbers of detected lines (dashed curve) and the total N_{HI} that they contain (solid curve) above various values of $\log(N_{HI})$. About 80% of the total column density is contained in lines with $N_{HI} > 10^{19} \text{ cm}^{-2}$ and only 10% in lines with $N_{HI} \leq 5 \times 10^{18} \text{ cm}^{-2}$, even though most of the detected lines lie at the lower column densities. The same general results are found if specific complexes, like the OA or MS, are excluded from the data. We conclude that the vast majority of faint lines does not contribute significantly to the total mass of high-velocity H I. Of course, this does not exclude the possibility that there are some high-velocity clouds which are not associated with the complexes and lie at a much greater distance thus containing significant mass (e.g., Braun & Burton (1999); Sembach et al. (1999); Burton, Braun, & Chengalur (2001)).

9. Summary Comments

The high-velocity H I emission detected in this survey covers 37% of the sky, and lines are found down to the median completeness limit of $8 \times 10^{17} \text{ cm}^{-2}$ and below. There is a nearly constant covering fraction per unit $\log(N_{HI})$ from $N_{HI} = 10^{19} \text{ cm}^{-2}$ down to the limit of the survey, and there is no indication of a cutoff in the high-velocity H I population at low N_{HI} . Extrapolating this trend to still lower N_{HI} implies a covering fraction near 60% for $N_{HI} \geq 10^{17} \text{ cm}^{-2}$. It is clear that the limiting N_{HI} of the high-velocity cloud phenomenon has yet to be established.

High-velocity H I emission lines can be characterized as either “wings” or “Gaussian components”, the difference being whether they are blended with lower-velocity emission and thus have uncertain properties (the wings), or can be fit by a Gaussian function whose parameters are likely to be meaningful (the components). There are 309 detected Gaussian components, found in 28% of the survey directions. Much of our analysis concentrates on the components (Table 4) because they have accurate velocities and their values of N_{HI} do not depend critically on the precise velocity definition of a “high-velocity” line. However, the Gaussian components are only part of the high-velocity H I phenomenon.

The vast majority of the weak lines detected in the survey seem related both spatially and kinematically to the lines known from previous work. Weak lines are not found outside the V_{LSR} range of the strong lines, and there is no evidence that the weak lines merge into the Hubble flow. The integrated emission of the high-velocity components is skewed to negative LSR velocities but has a mean near zero when motion of the LSR about the Galactic Center is removed.

Most of the lines detected in this survey, at all values of N_{HI} , are associated with complexes like the Magellanic Stream and Complex C. The fraction of association may be as high as 90%. At the sensitivity of the survey the Magellanic Stream appears to extend at least 10° to higher Galactic latitude than previously thought, and, near its tip, broadens in longitude as well. Low- N_{HI} lines associated with known complexes can be found far outside their traditional boundaries, e.g., in the Magellanic Stream and Wright’s cloud. The covering fraction of the sky increases as lower N_{HI} lines are measured mainly because the size of individual clouds grows. Our data thus suggest that, at the sensitivity level of the survey, most high-velocity clouds do not have sharp edges in H I.

Compact high-velocity clouds have received recent scrutiny because they may be at a larger distance than the principle complexes (Braun & Burton 1999; Burton, Braun, & Chengalur 2001). There are a few low- N_{HI} lines which appear spatially isolated in the survey data (Table 9), but the majority of the emission appears to be extended, and in some directions it is extended at low N_{HI} . It would be quite valuable to observe these with higher angular resolution to see if the material is clumped or remains fairly smooth.

Despite the abundance of low- N_{HI} lines, their numbers are not sufficient to contribute substantially to the mass of high-velocity H I unless, against the evidence, they are located far beyond the bright clouds. This was the conclusion also of Colgan, Salpeter, & Terzian (1990), and Murphy, Lockman, & Savage (1995). In a set of compact, isolated, high-velocity clouds mapped at high angular resolution, the extended halos contain most of the H I flux (Burton, Braun, & Chengalur 2001). In this respect the compact clouds may have a different structure than the more general high-velocity emission.

In contrast to spiral galaxies, whose H I disks have sharp edges and do not increase in size as observational sensitivity is increased (van Gorkom 1993), the area covered by high-velocity H I clouds is a strong function of the sensitivity of the observations (cf the current results with those of Giovanelli (1980), Wakker (1991), and Colgan, Salpeter, & Terzian (1990)). And yet, the high-velocity emission seems so concentrated into complexes that observation in only a few directions may easily produce misleading impressions about its global properties (e.g., Bowen, Blades & Pettini (1995)). For this reason we believe that many more sight-lines must be studied in the UV before it can be determined if there is a statistical excess in the occurrence of, e.g., Mg II high-velocity lines compared to 21cm high-velocity lines.

If the bright H I lines which constitute the “classic” high-velocity cloud population are merely the peaks in a more extended medium, then the validity of statistical analyses based on cloud counts must be called into question. A clumpy cloud may be counted several times if observations are not sensitive enough to reveal the gas between the clumps. Until there is a better way of specifying the boundaries of a cloud than a noise level set by instrumentation, we believe that statistical analyses of cloud counts are in danger of giving misleading results.

There are high-velocity clouds which are predominantly ionized at $\sim 10^4$ K, there are clouds with a significant component of mass at $T \sim 3 \times 10^5$ K, and there may even be clouds which are sources of soft X-ray emission (Sembach et al. 1995; Weiner & Williams 1996; Tufte, Reynolds & Haffner 1998; Kerp et al. 1999; Sembach et al. 1999, 2000). This suggests that the observed low- N_{HI} lines in some directions might arise in a trace neutral component of an otherwise ionized cloud. The gas toward III Zw 2, where there is high-velocity Mg II absorption (§6.1) but no detectable 21cm H I line, may be in a similar state. These considerations reinforce the view that bright H I clumps are merely one aspect of the high-velocity cloud phenomenon.

We thank the staff of the 140 Foot Telescope for their efforts throughout this project, and in particular the supervisor, George Liptak. The 140 Foot Telescope was retired in July 1999 after 26 years of service. We also thank Blair Savage, Brent Tully, Phil Maloney and John Hibbard for information, comments, and assistance. The referee made several stimulating comments which improved the paper significantly. The research of S.P-P. and V.J.U. at NRAO was supported by the NSF under an REU program grant.

REFERENCES

Anders, E., & Grevesse, N. 1989, *Geochim. Cosmochim. Acta*, 53, 197

- Appleton, P. N., Davies, R. D., & Stephenson, R. J. 1981, MNRAS, 195, 327
- Barnes, D.G. et al. 2001, MNRAS, 322, 486
- Blitz, L., Spergel, D.N., Teuben, P.J., Hartmann, D., & Burton, W.B. 1999, ApJ, 514, 818
- Bochkarev, N.G., & Syunyaev, R.A. 1977, Soviet Astronomy, 21, 542
- Bowen, D.V., & Blades, J.C. 1993, ApJ, 403, L55
- Bowen, D.V., Blades, J.C., & Pettini, M. 1995, ApJ, 448, 662
- Braun, R., & Burton, W.B. 1999, A&A, 341, 437
- Braun, R., & Burton, W.B. 2000, A&A, 354, 853
- Bregman, J.N. 1980, ApJ., 236, 577
- Brüns, C., Kerp, J., Kalberla, P.M.W., & Mebold, U. 2000, A&A, 357, 120
- Burton, W.B., Braun, R., & Chengalur, J.N. 2001, A&A, 369, 616
- Charleton, J.C., Churchill, C.W., & Rigby, J.R. 2000, ApJ, 544, 702
- Colgan, S.W.J., Salpeter, E.E., & Terzian, Y. 1990, ApJ, 351, 503
- Corbelli, E., & Salpeter, E.E. 1993, ApJ, 419, 104
- Cram, T.R., & Giovanelli, R. 1976, A&A, 48, 39
- Davies, R.D. 1972, Nature, 237, 88
- Ferrara, A., & Field, G.B. 1994, ApJ, 423, 665
- Gardiner, L.T., & Noguchi, M. 1996, MNRAS, 278, 191
- Gardiner, L.T. 1999, in Stromlo Workshop on High Velocity Clouds, ed. B.K. Gibson & M.E. Putman, ASP Conference Ser. Vol. 166, p. 292
- Gibson, B.K., Giroux, M.L., Penton, S.V., Putman, M.E., Stocke, J.T., & Shull, J.M. 2000, AJ, 120, 1830
- Giovanelli, R. 1980, AJ, 85, 1155
- Habing, H.J. 1966, Bull. Astron. Inst. Netherlands, 18, 323
- Haud, U. 1992, MNRAS, 257, 707

- Haynes, M.P. 1979, *AJ*, 84, 1173
- Hulsbosch, A.N.M., & Wakker, B.P. 1988, *A&AS*, 75, 191
- Kalberla, P.M.W., Mebold, U., & Reich, W. 1980, *A&A*, 82, 275
- Kalberla, P.M.W., & Kerp, J. 1999, in *Stromlo Workshop on High Velocity Clouds*, ed. B.K. Gibson & M.E. Putman, ASP Conference Series Vol. 166, p. 155
- Kerp, J., Burton, W.B., Egger, R., Freyberg, M.J., Hartmann, D., Kalberla, P.M.W., Mebold, U., & Pietz, J. 1999, *A&A*, 342, 213.
- Lockman, F.J., Jahoda, K., & McCammon, D. 1986, *ApJ*, 302, 432
- Lockman, F.J., & Savage, B.D. 1995, *ApJS*, 97, 1
- Lu, L., Savage, B.D., & Sembach K.R. 1994, *ApJ*, 426, 563
- Lu, L., Savage, B.D., Sembach, K.R., Wakker, B.P., Sargent, W.L.W., & Osterloo, T.A. 1998, *AJ*, 115, 162
- Mallouris, C., Lanzetta, K.M., Burks, G.S., & York, D.G. 1999, in *Stromlo Workshop on High Velocity Clouds*, ed. B.K. Gibson & M.E. Putman, ASP Conference Series Vol. 166, p. 138
- Maloney, P. 1993, *ApJ*, 414, 41
- Mathewson, D.S., Cleary, M.N., & Murray, J.D. 1974, *ApJ*, 190, 291
- Mirabel, I.F. 1981, *ApJ*, 250, 528
- Morras, R. 1985, *AJ*, 90, 1801
- Morras, R., Bajaja, E., Arnal, E.M. & Pöppel, W.G.L. 2000, *A&AS*, 142, 25
- Muller, C.A., Oort, J.H., & Raimond, E. 1963, *C.R. Acad. Sci. Paris*, 257, 1661
- Murphy, E.M., Lockman, F.J., & Savage, B.D. 1995, *ApJ*, 447, 642
- Murphy, E.M. et al. 2000, *ApJ*, 538. L35
- Norman, C.A., & Ikeuchi, S. 1989, *ApJ*, 345, 372.
- Oort, J.H. 1966, *Bull. Astr. Inst. Neth.*, 18, 421
- Putman, M.E. 2000, *PASA*, 17, 1

- Putman, M.E. 2000a PhD Thesis, Australian National Univ.
- Putman, M.E. et al., 1998, *Nature*, 394, 752
- Putman, M.E., & Gibson, B.K. 1999, *PASA*, 16, 70
- Putman, M.E., et al. 2002, *AJ*, (in press)
- Richter, P., Sembach, K.R., Wakker, B.P., Savage, B.D., Tripp, T.M., Murphy, E.M., Kalberla, P.M., & Jenkins, E.B. 2001, *ApJ*, 559, 318
- Savage, B.D., et al., 1993, *ApJ*, 413, 116
- Savage, B.D., & Sembach, K.R. 1996, *ARAA*, 34, 279
- Sembach, K.R., Savage, B.D., Lu, L., & Murphy, E.M. 1995, *ApJ*, 451, 616
- Sembach, K.R., Savage, B.D., Lu, L., & Murphy, E.M. 1999, *ApJ*, 515, 108
- Sembach, K.R. et al. 2000, *ApJ*, 538, L31
- Sembach, K.R., Howk, J.C., Savage, B.D., & Shull, J.M. 2001, *AJ*, 121, 992
- Shapiro, P.R., & Field, G.B. 1976, *Ap.J.*, 205, 762
- Tufte, S.L., Reynolds, R.J., & Haffner, L.M. 1998, *ApJ*, 504, 773
- van Gorkom, J.H. 1991, in *Atoms, Ions and Molecules: New Results in Spectral Line Astrophysics*, ed. A.D. Haschick & P.T.P. Ho, ASP Conference Ser. Vol 16, p. 1
- van Gorkom, J. 1993, in *The Environment and Evolution of Galaxies*, ed. J.M. Shull & H.A. Thronson, Kluwer, p. 345
- van Woerden, H., Schwarz, U.J., Peletier, R.F., Wakker, B.P., & Kalberla, P.M.W. 1999, *Nature*, 400, 138.
- Verschuur, G.L. 1975, *ARAA*, 13, 257
- Wakker, B.P. 1991, *A&A*, 250, 499
- Wakker, B.P., & van Woerden, H. 1991, *A&A*, 250, 509
- Wakker, B.P., & van Woerden, H. 1997, *ARAA*, 35, 217
- Wayte, S.R. 1989, *Proc. ASA*, 8, 195

Weiner, B.J., & Williams, T.B. 1996, *AJ*, 111, 1156

West, K.A., Pettini, M., Penston, M.V., Blades, J.C., & Morton, D.C. 1985, *MNRAS*, 215, 481

Williams, D.R.W. 1973, *A&AS*, 8, 505

Wright, M.C.H. 1974, *A&A*, 31, 317

Wright, M.C.H. 1979, *ApJ*, 233, 35

Yun, M.S., Ho, P.T.P., & Lo, K.Y. 1994, *Nature*, 372, 530

Zwann, M.A. 2001, *MNRAS*, 325, 1142

Zwaan, M.A., & Briggs, F.H. 2000, *ApJ*, 530, L61

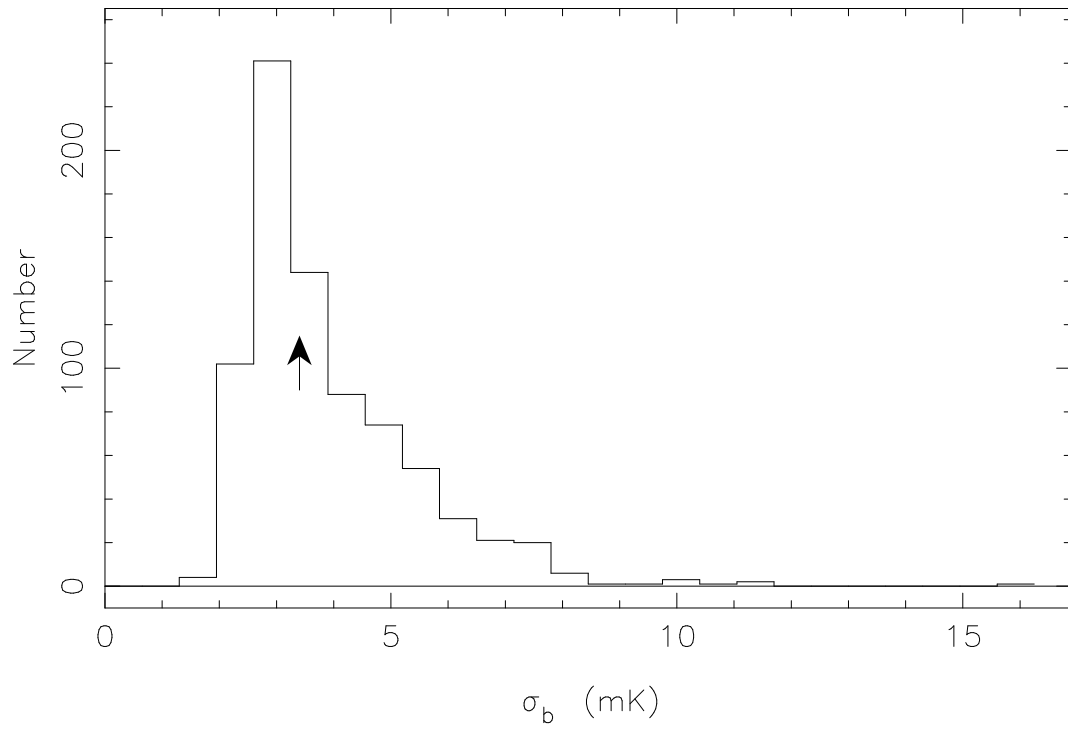


Fig. 1.— The distribution of the rms baseline noise in the final position-switched spectra. The median value, 3.4 mK, is shown with an arrow.

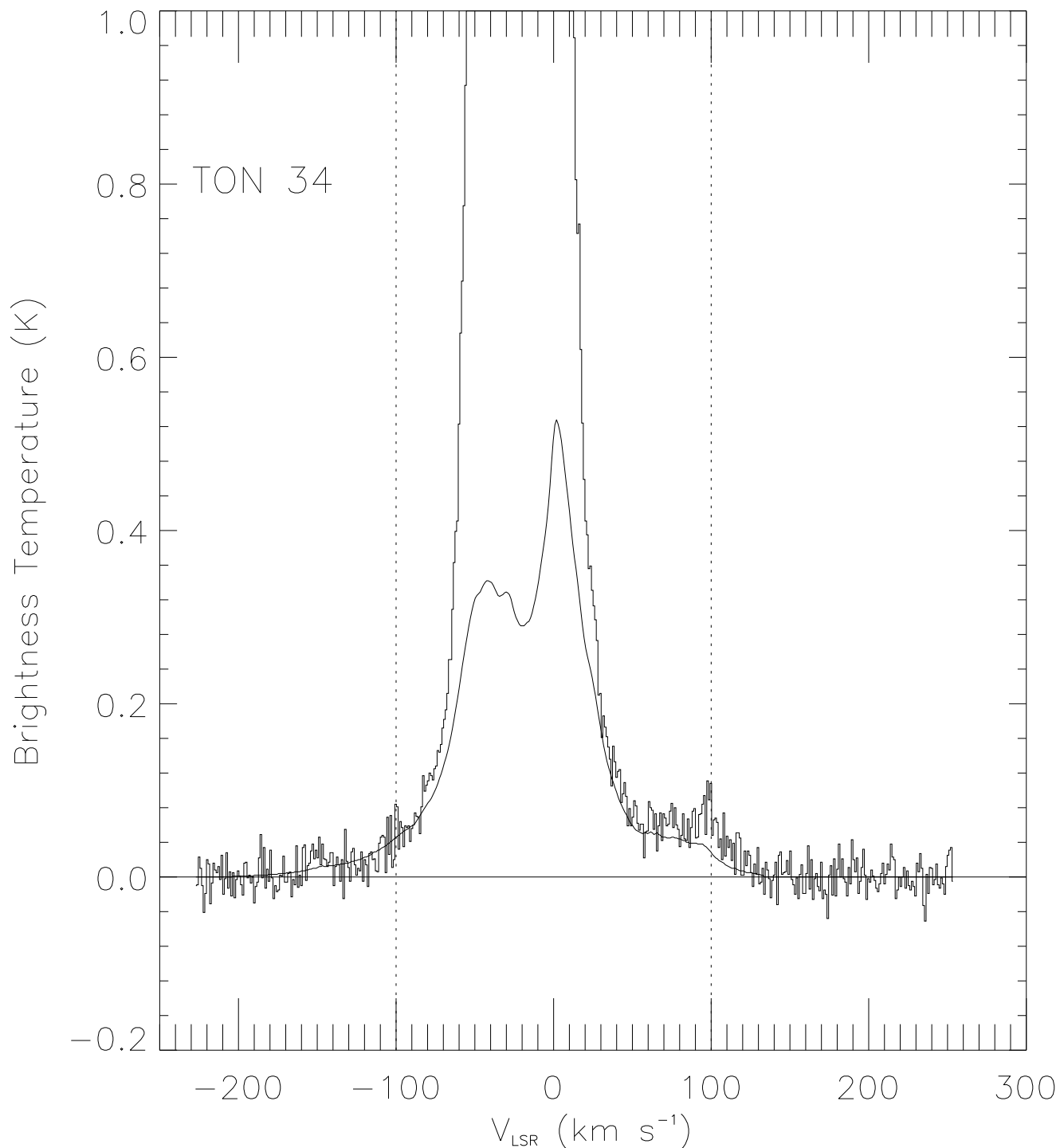


Fig. 2.— A portion of a frequency-switched H I spectrum toward Ton 34 at $\ell, b = 203^{\circ}0, +56^{\circ}5$ illustrating stray radiation. Superimposed on the observed 140 Foot spectrum is a smooth curve showing the amount of the detected signal attributed to stray radiation which has entered the telescope’s sidelobes. The long wing to positive velocity is almost entirely spurious, though more sensitive position-switched data show that the small excess emission above the stray near $V = +100 \text{ km s}^{-1}$ is actually real. The observations have been clipped at 1.0 K for display; the corrected peak T_b of the line is 4.5 K.

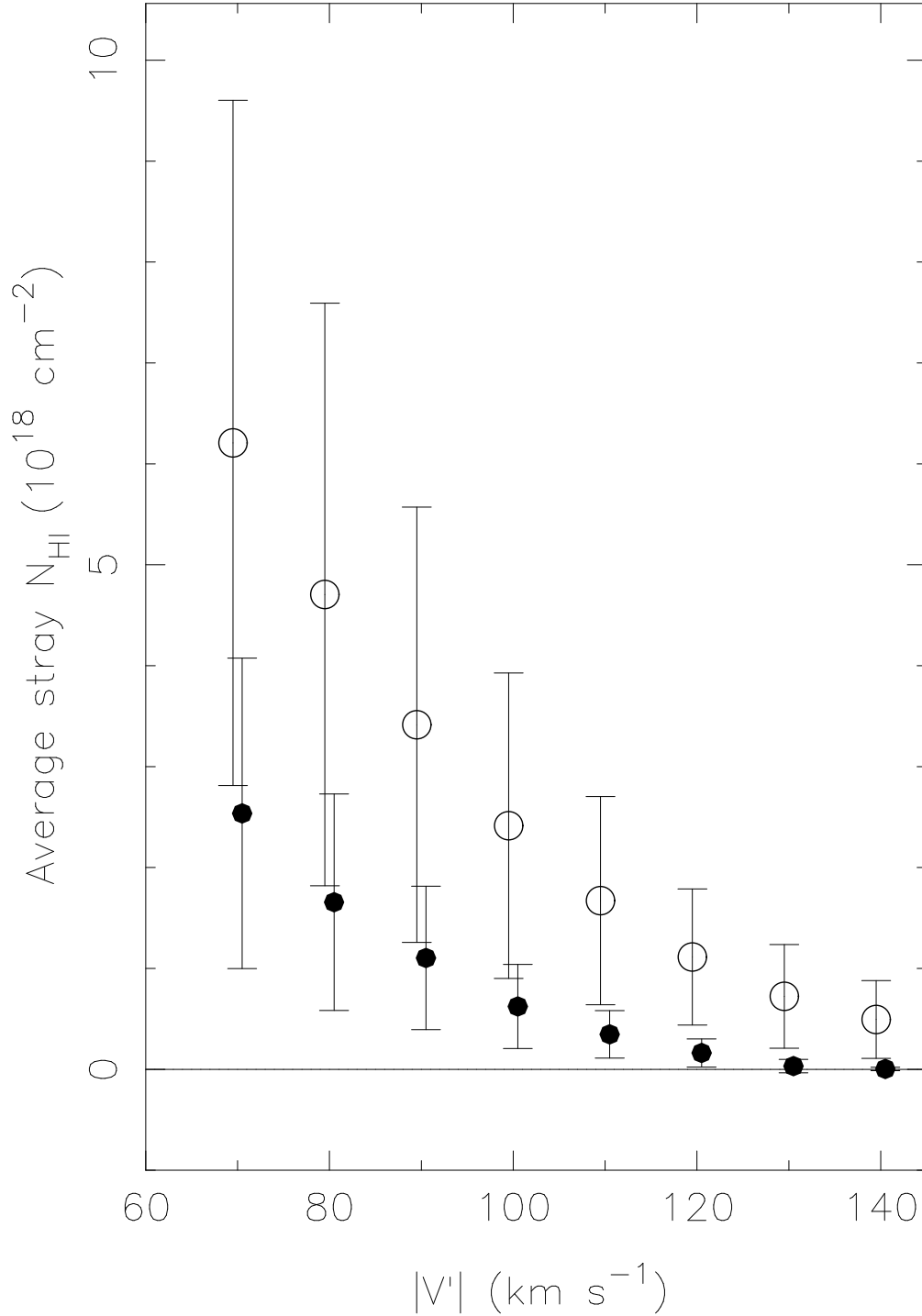


Fig. 3.— The average amount of stray radiation, expressed as an equivalent N_{HI} , that was removed from the ~ 100 frequency-switched spectra in the survey. For each value of V' the Figure shows the amount of stray radiation at greater (or lesser) LSR velocities. Stray radiation at negative velocities is indicated with an open circle; at positive velocities with a filled circle. This Figure shows that the average frequency-switched spectrum in the survey had a spurious wing at $V_{LSR} < -100$ km s $^{-1}$ with $N_{HI} \sim 2 \times 10^{18}$, and a spurious wing at $V_{LSR} > +100$ km s $^{-1}$ with $N_{HI} \sim 0.6 \times 10^{18}$ cm $^{-2}$.

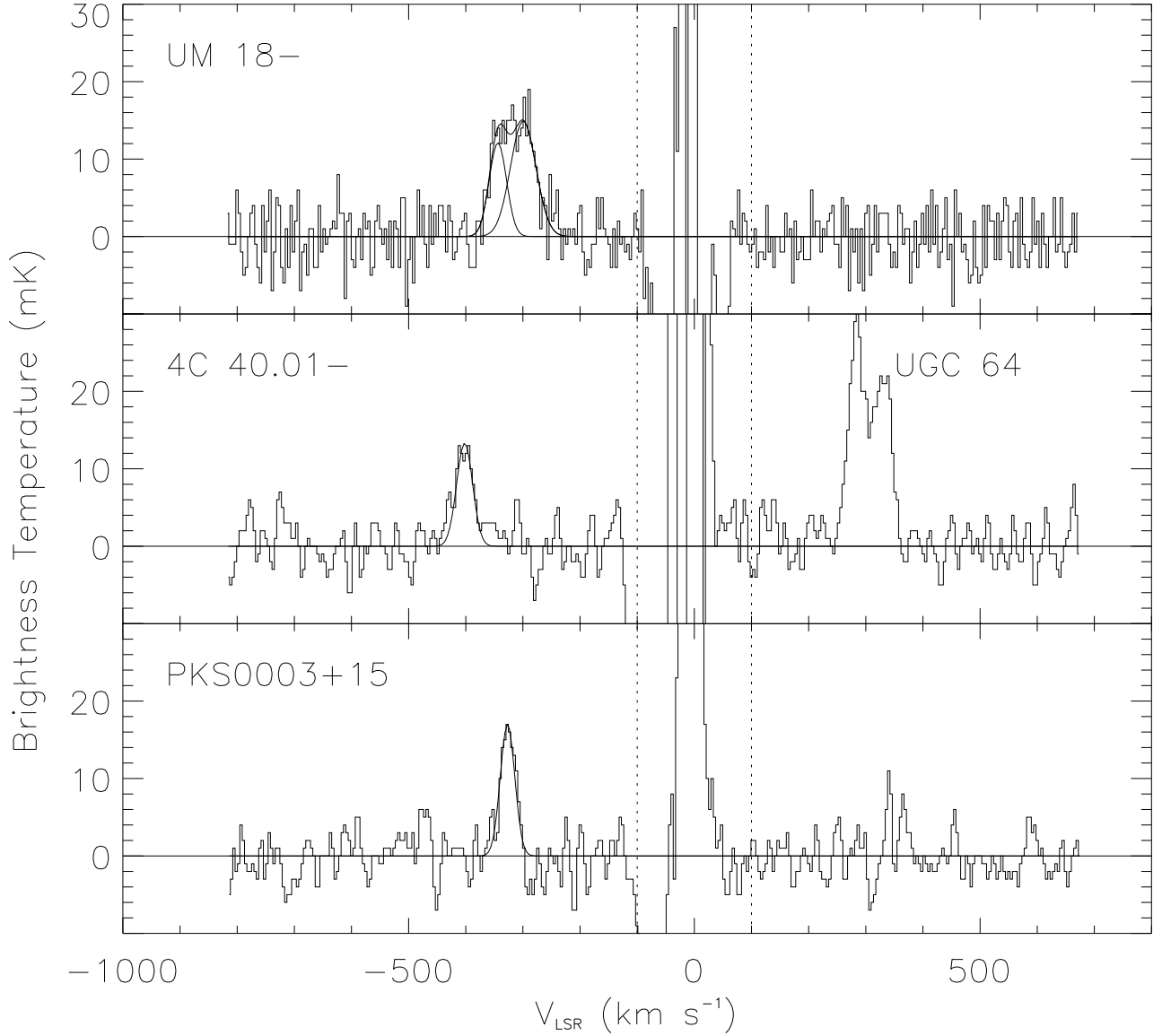


Fig. 4.— Sample position-switched spectra showing the data quality and examples of the weaker H I emission lines detected in the survey. Vertical lines at ± 100 km s $^{-1}$ mark the adopted limits for high-velocity gas. Emission at $|V_{LSR}| < 100$ km s $^{-1}$ is often nearly canceled in the position-switching. The lower two spectra have been Hanning smoothed. The top panel shows two lines separated by 44 km s $^{-1}$ near -300 km s $^{-1}$ with $N_{HI} = 8.3 \times 10^{17}$ and 1.5×10^{18} cm $^{-2}$. The central panel has a line from a high-velocity cloud at -400 km s $^{-1}$ with $N_{HI} = 8.5 \times 10^{17}$ cm $^{-2}$, and, near $+300$ km s $^{-1}$, H I emission from the galaxy UGC 64 which lies serendipitously in the antenna beam. In the lower panel, the line at $V_{LSR} = -327$ km s $^{-1}$ has a FWHM of 30 km s $^{-1}$, equal to the median of all detected lines, and $N_{HI} = 9.8 \times 10^{17}$ cm $^{-2}$. The rms noise in the spectra is 3.5 mK, 2.7 mK, and 2.4 mK, upper to lower. The median completeness level of the survey is 8×10^{17} cm $^{-2}$, similar to the N_{HI} in most of the high-velocity lines shown here.

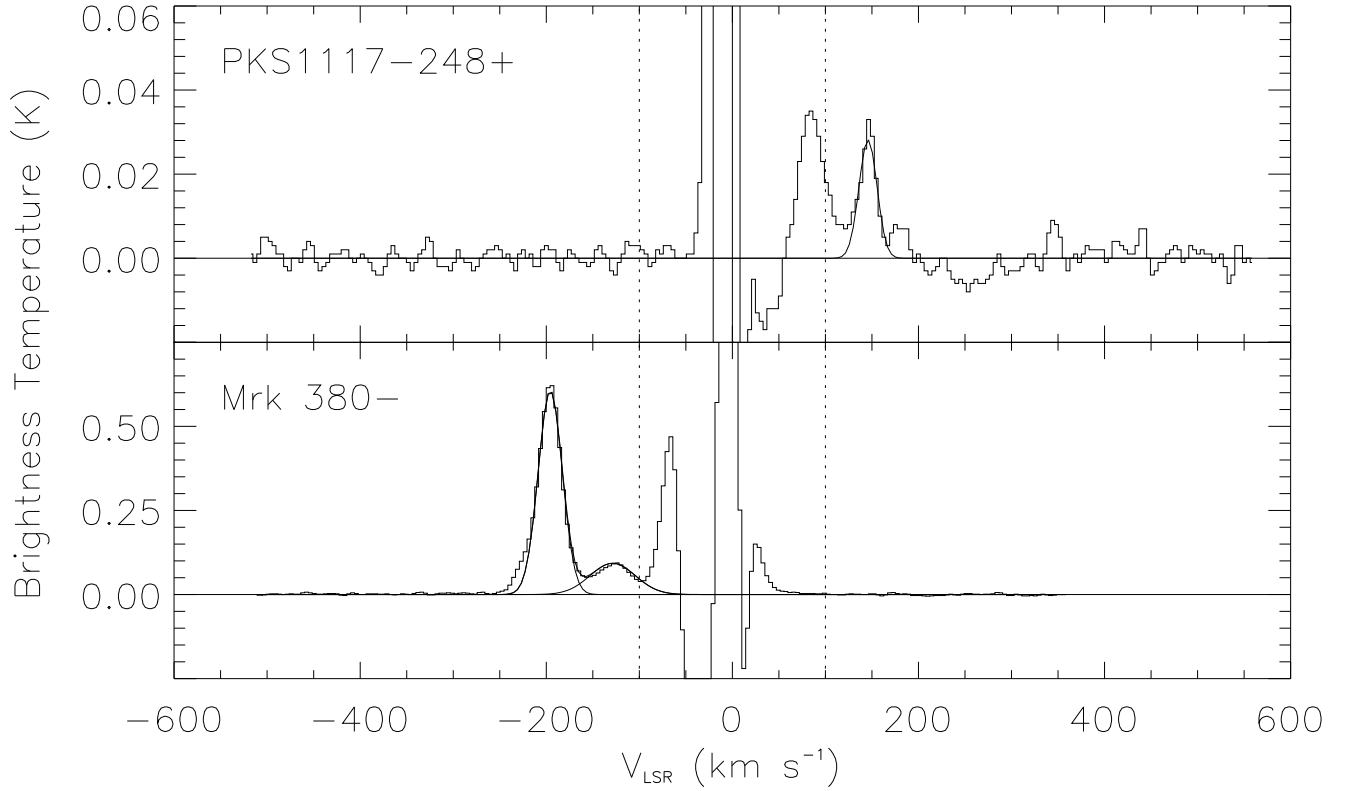


Fig. 5.— The central portions of two smoothed spectra showing wings and blended lines. The temperature scales differ by more than an order of magnitude. The upper panel has a Gaussian component at $+145 \text{ km s}^{-1}$ with $N_{HI} = 1.25 \times 10^{18} \text{ cm}^{-2}$ and additional emission at a lower velocity which is treated as a “wing” because its shape at $V_{LSR} \lesssim 80 \text{ km s}^{-1}$ arises from cancellation in the position-switching and hence Gaussian parameters would have no physical significance. In the lower panel the H I at $V < -100 \text{ km s}^{-1}$ is treated as two individual Gaussians plus some additional emission. The rms noise in the upper spectrum is 2.2 mK; in the lower spectrum it is 3.5 mK. An instrumental problem caused the apparent absorption in the upper panel at $+250 \text{ km s}^{-1}$ (see §2.4).

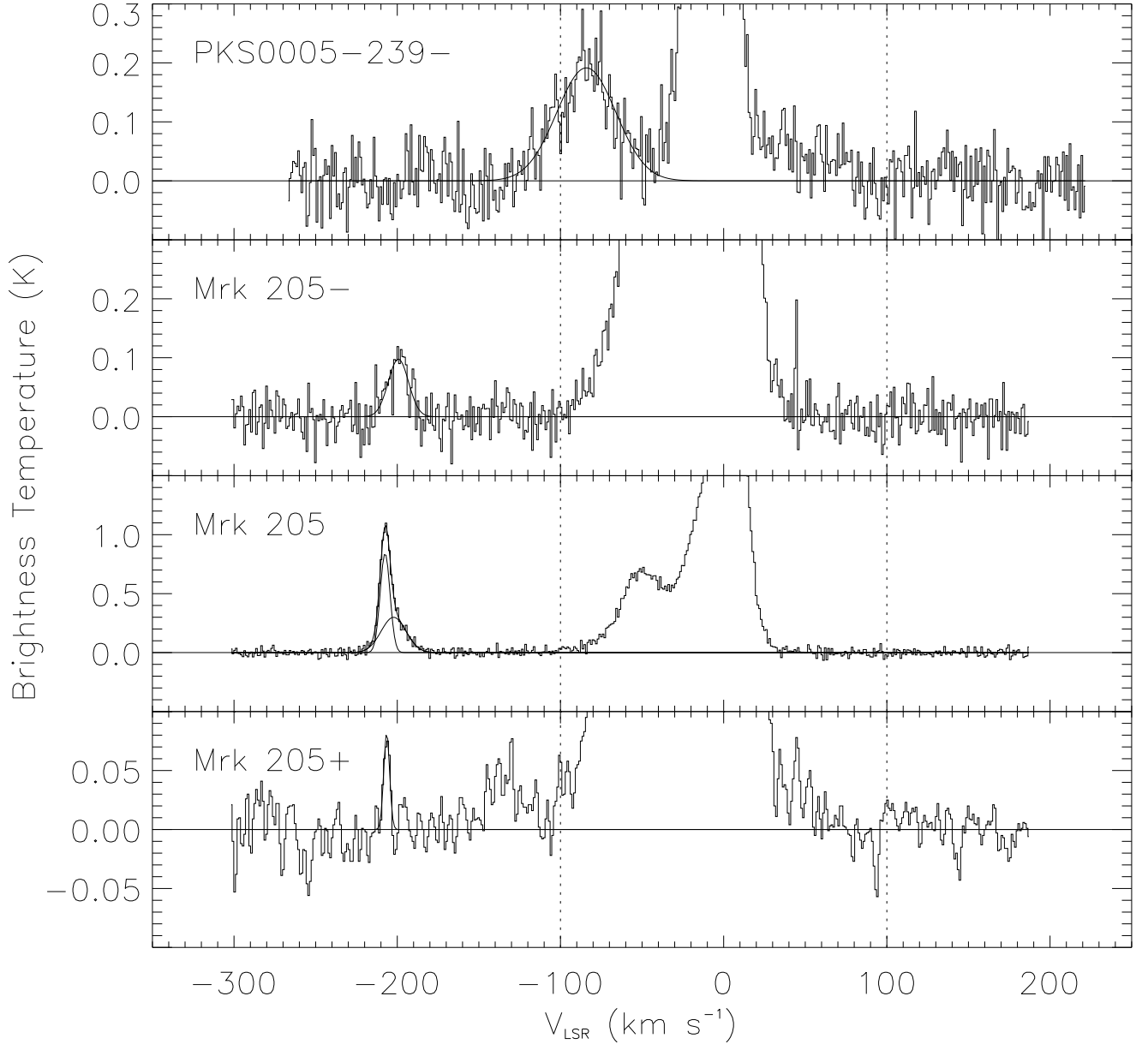


Fig. 6.— Representative frequency-switched spectra. Only the bottom one has been smoothed. All have been corrected for stray radiation. There is weak interference in the Mrk 205– spectrum near +40 km s⁻¹. The apparent emission at -140 km s⁻¹ toward Mrk 205+ could not be confirmed in the position-switched data and may be residual stray radiation which the deconvolution process did not remove. The line toward Mrk 205+ is the narrowest in the survey, with $\Delta v = 4.2 \pm 0.8$ km s⁻¹, and $N_{\text{HI}} = 6.7 \times 10^{17}$.

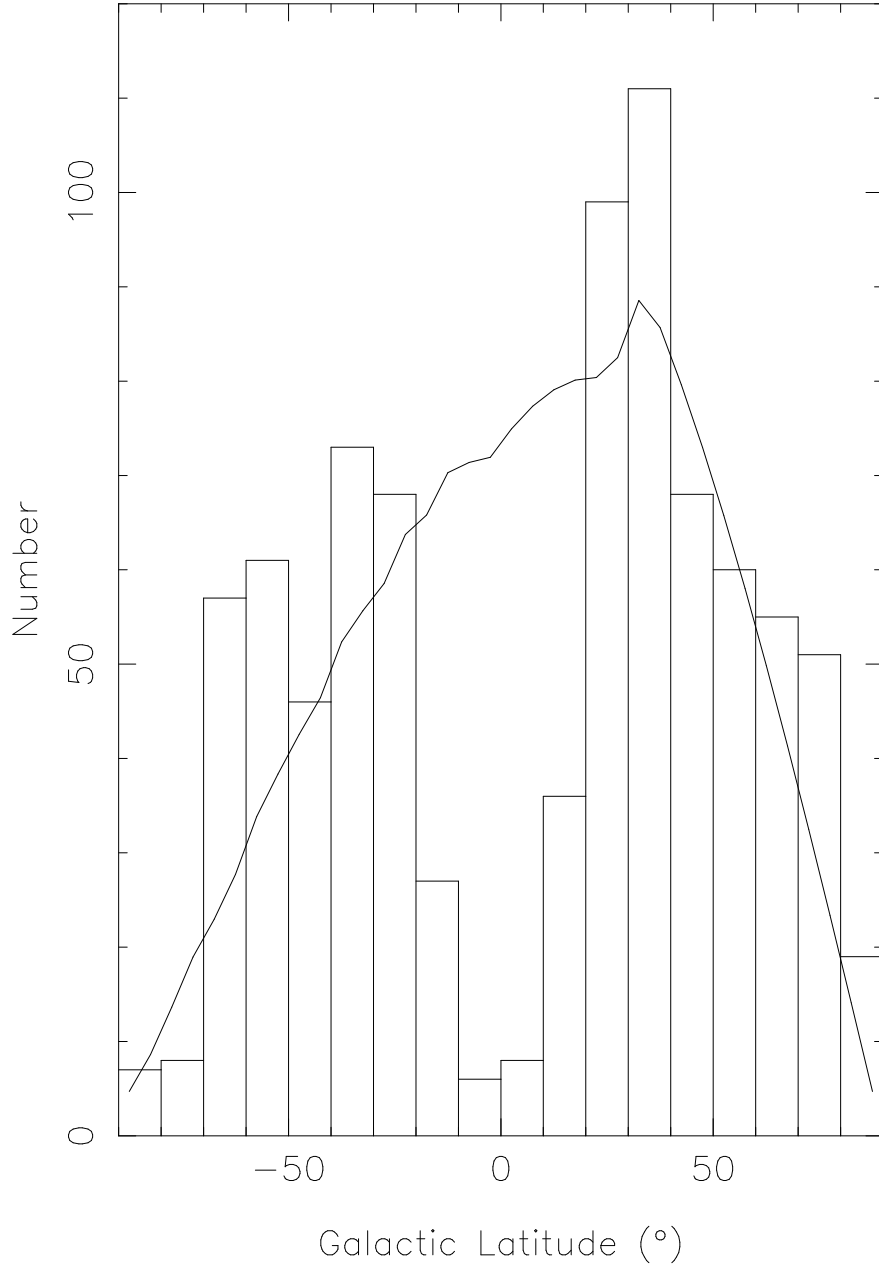


Fig. 7.— The distribution of observed Galactic latitudes, with a curve proportional to the fraction of the sky at each latitude which lies at $\delta \geq -30^\circ$. The survey has reasonably uniform coverage in latitude except at $|b| < 20^\circ$, where the selection criterion produces a bias against directions with high extinction.

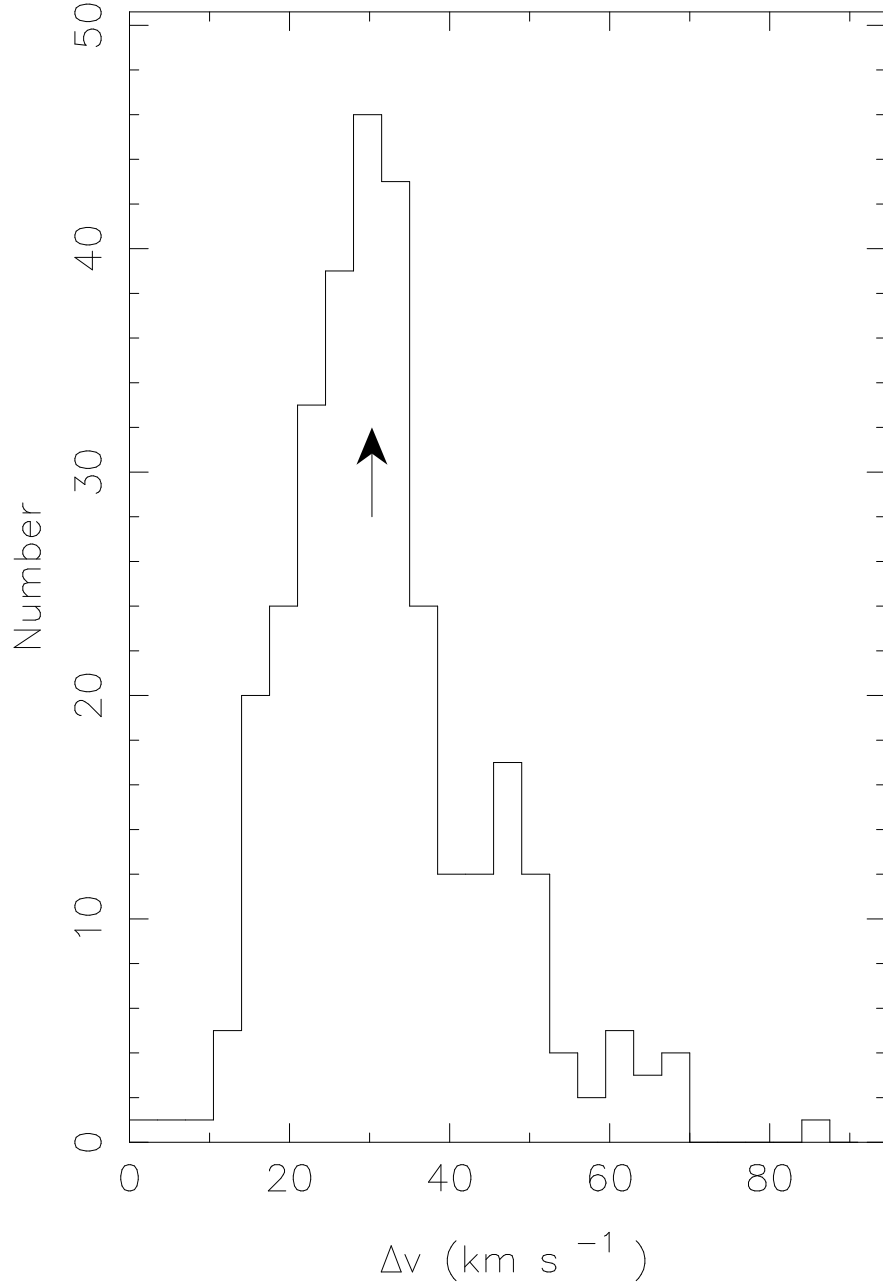


Fig. 8.— The distribution of linewidths after correction in quadrature for the width of the spectrometer channels. The median value of 30.3 km s^{-1} is marked with an arrow.

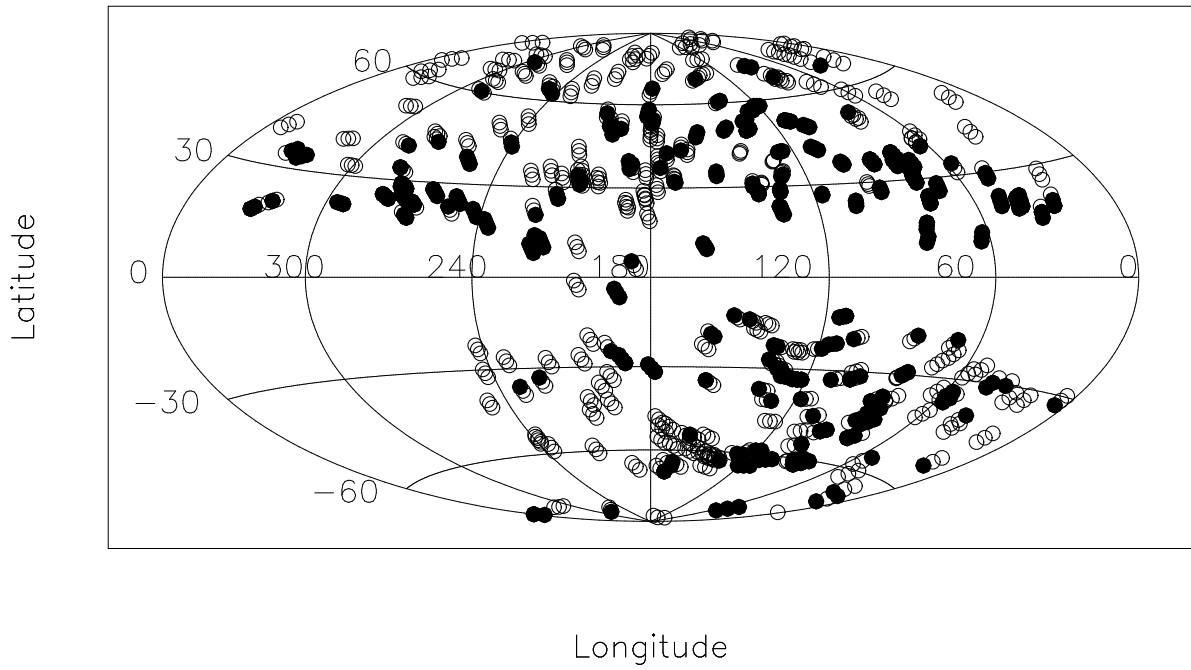


Fig. 9.— The survey directions in an Aitoff projection centered on $\ell, b = 180^\circ, 0^\circ$. Open symbols mark directions without high-velocity H I, filled symbols mark detections of H I at $|V_{LSR}| > 100 \text{ km s}^{-1}$.

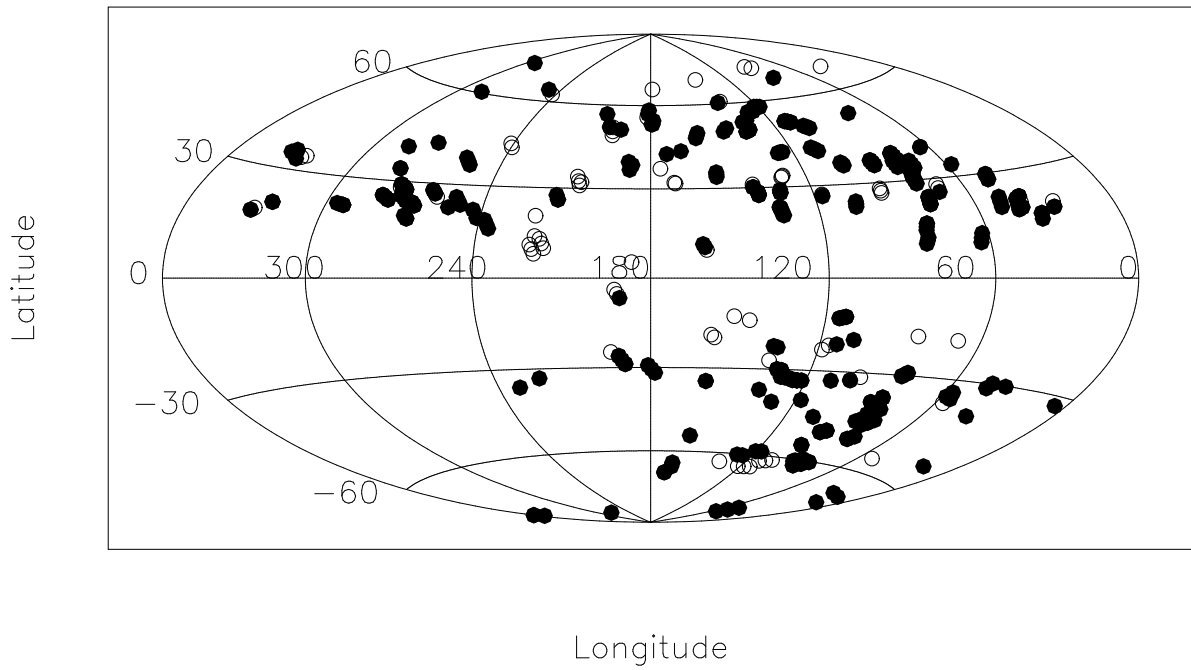


Fig. 10.— An Aitoff projection centered on $\ell, b = 180^\circ, 0^\circ$ showing directions where high-velocity H I was detected. Open symbols identify lines that are wings blended with low-velocity emission, and solid symbols identify H I lines well-separated from low-velocity emission which can be characterized by a Gaussian function.

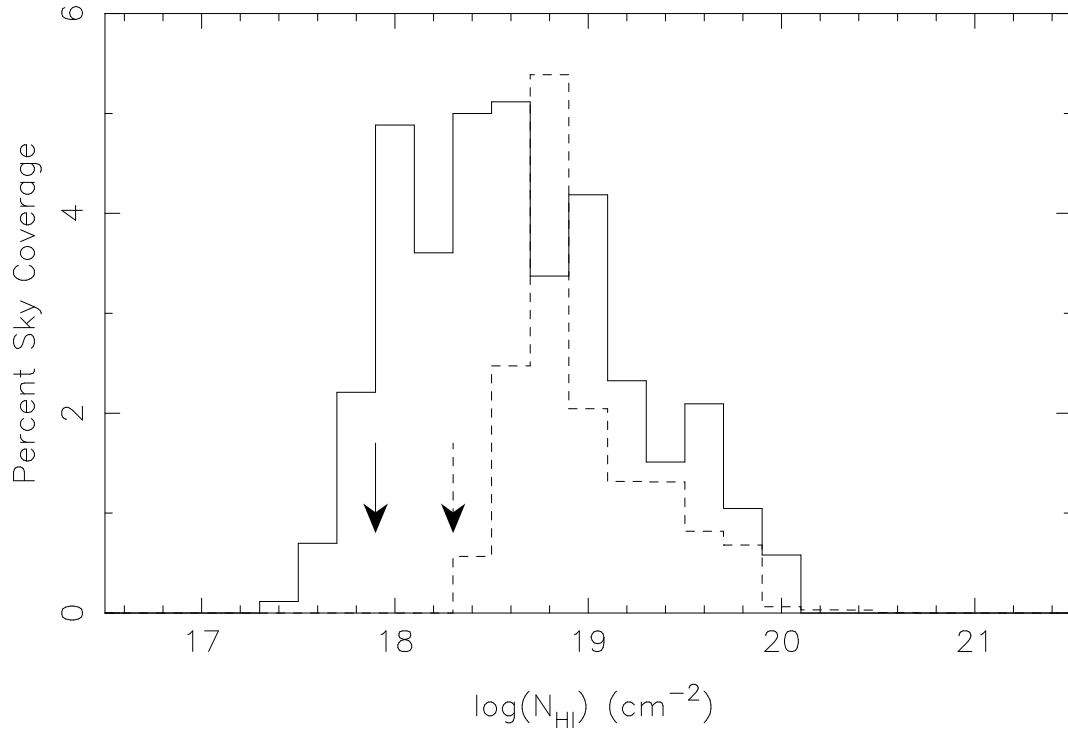


Fig. 11.— The solid line is the percentage of the sky covered by high-velocity H I emission in each interval of $\log(N_{HI})$ from the data of this survey. The solid arrow marks the estimated median completeness limit of the survey: $8 \times 10^{17} \text{ cm}^{-2}$. The dashed line is the percentage sky coverage derived from the compilation of Wakker (1991) and the dashed arrow is the estimated completeness level of that compilation. Summed over all values of N_{HI} , 37% of the sky is covered with detectable high-velocity H I.

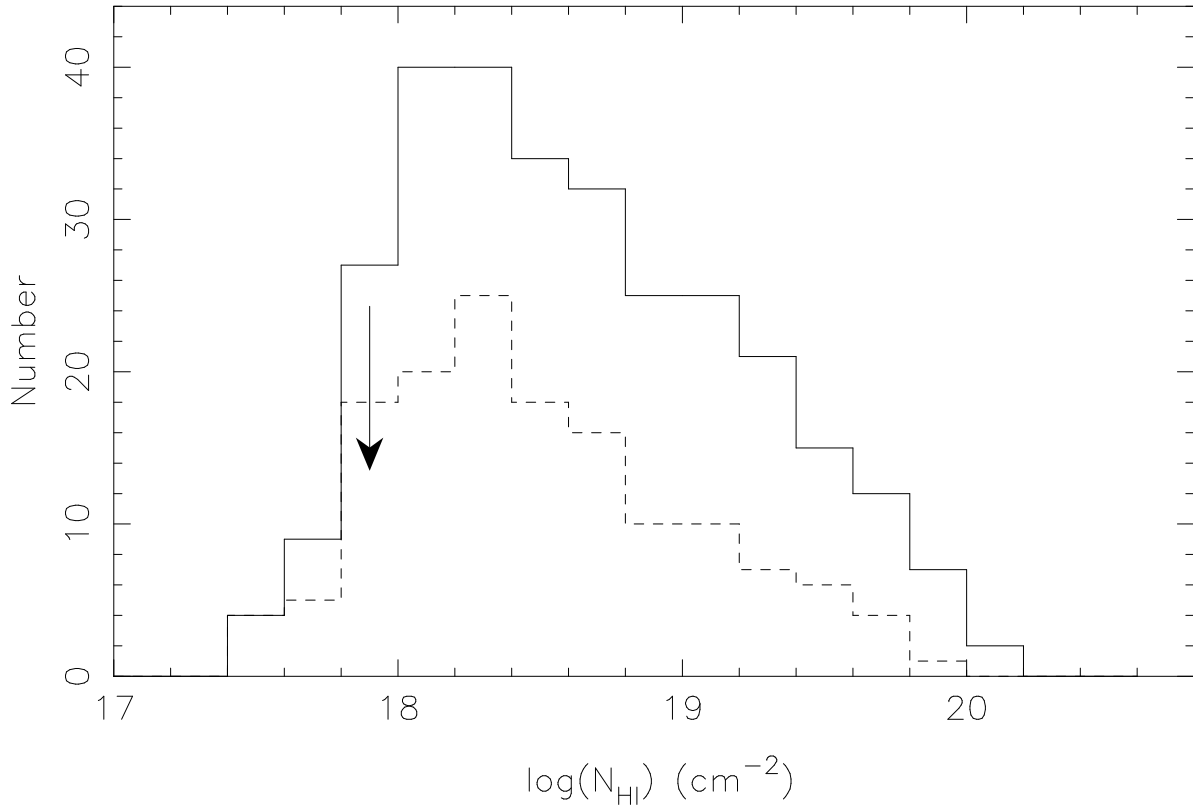


Fig. 12.— The number of Gaussian high-velocity H I lines detected in the survey as a function of their $\log(N_{HI})$. The solid curve is for all lines with $|V_{pk}| \geq 100 \text{ km s}^{-1}$, and the dashed curve is for the higher velocity lines with $|V_{pk}| \geq 150 \text{ km s}^{-1}$ only. The arrow shows the completeness level of the survey.

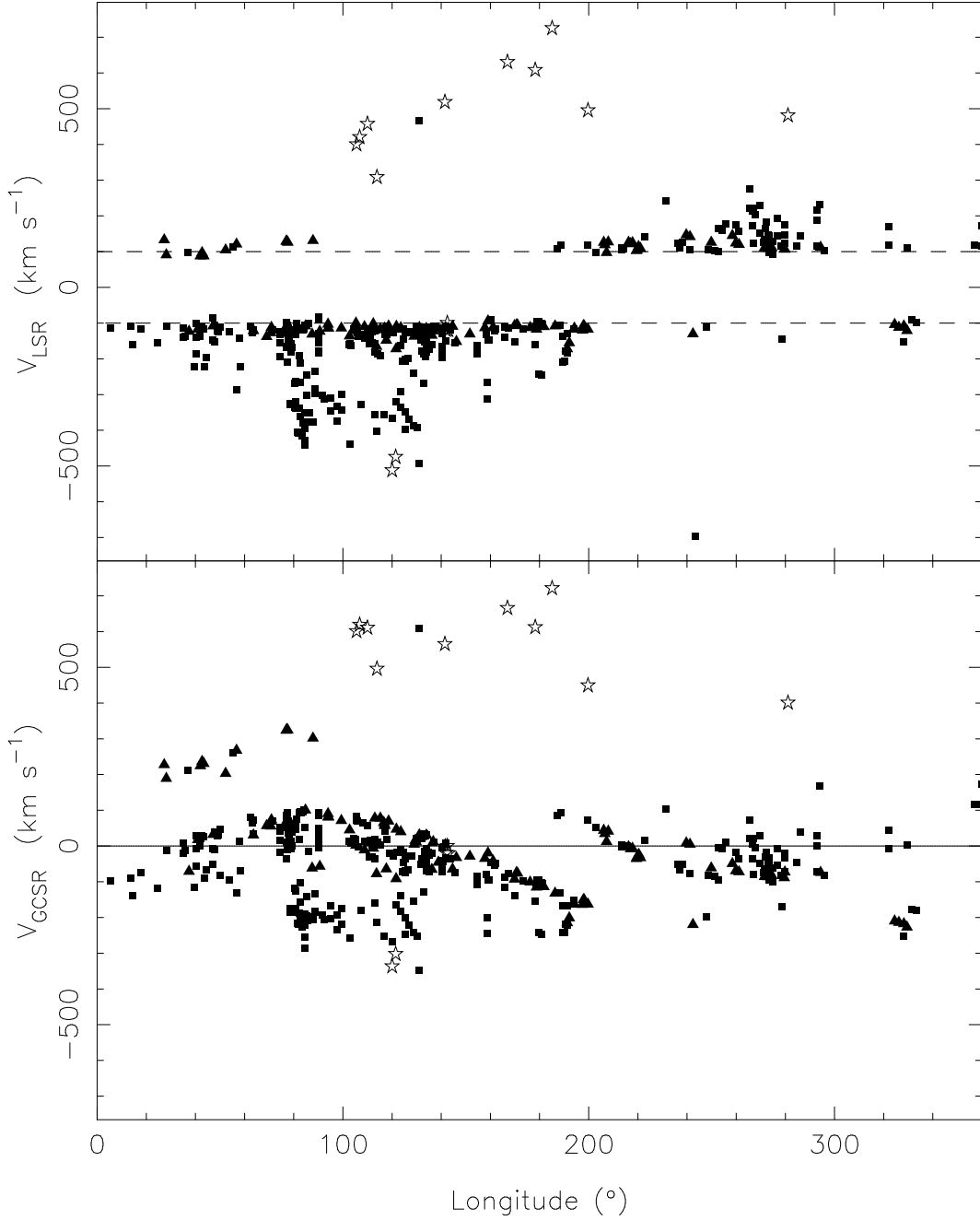


Fig. 13.— Velocity of high-velocity H I lines with respect to the LSR, and to the Galactic Center, plotted against Galactic longitude. Filled squares are Gaussian components, filled triangles are line wings, and open stars are known galaxies which were detected by accident during the survey. The dashed lines in the upper panel are at $\pm 100 \text{ km s}^{-1}$ and show the adopted V_{LSR} limit for high-velocity gas. There is a distinct transition between the high-velocity H I clouds and the positive-velocity galaxies which are part of the Hubble flow (the filled squares at $V_{LSR} = +465$ and -700 km s^{-1} are from very weak lines which may not be real). Much of the pattern of $V_{LSR}(\ell)$ is due to Galactic rotation.

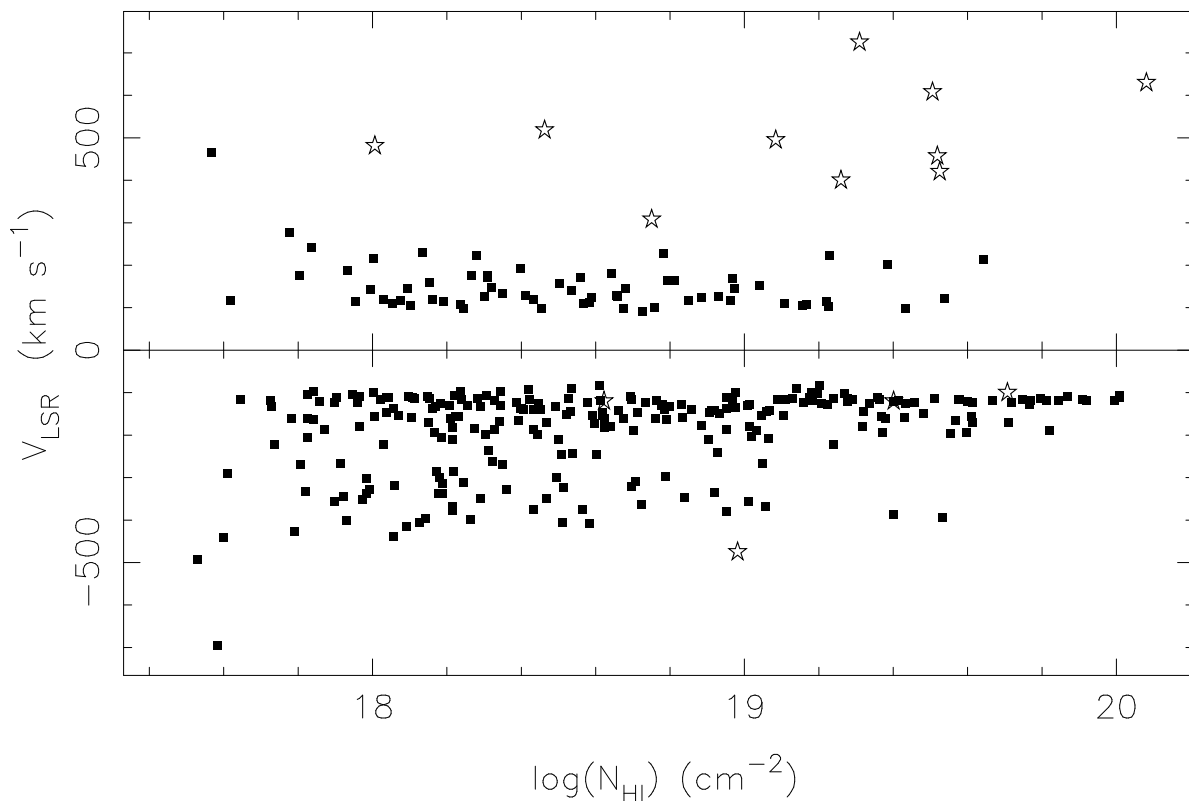


Fig. 14.— The LSR velocity of the Gaussian component high-velocity H I lines (Table 4) vs. their N_{HI} , where galaxies detected in the survey are shown as open stars. The weakest lines have kinematics similar to all but the very strongest lines. Values of N_{HI} for the galaxies are lower limits because the observations were not necessarily centered on those objects. There is a distinct separation between the high-velocity H I lines and the lines from galaxies which, apart from M31 at $V_{\text{LSR}} \approx -500 \text{ km s}^{-1}$, are part of the Hubble flow.

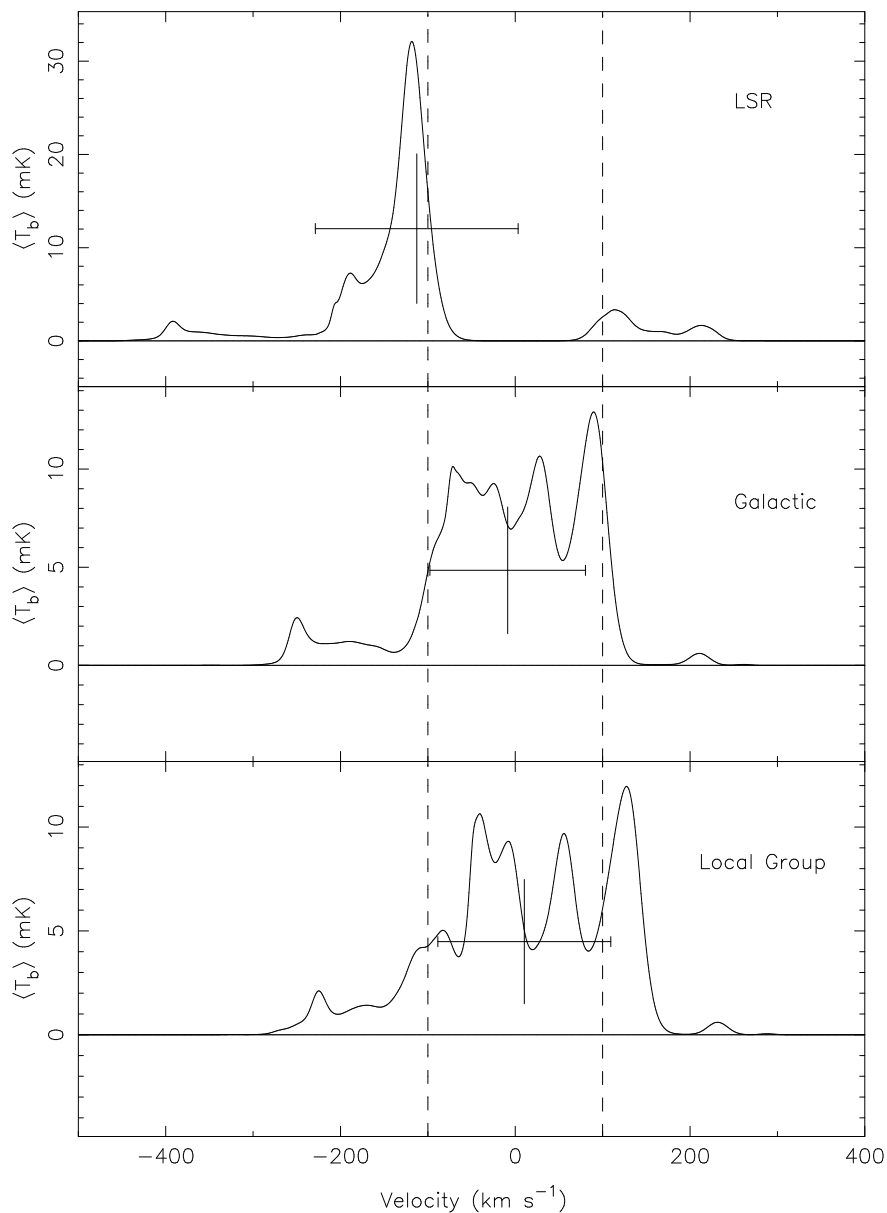


Fig. 15.— The total 21cm H I emission of the high-velocity Gaussian components summed with respect to the LSR (top panel), with respect to the Galactic Center standard of rest (center panel), and with respect to the Local Group standard of rest (lower panel). The dashed lines are at ± 100 km s⁻¹. The cross in each spectrum is centered at the mean velocity of the emission and the horizontal bar is ± 1 standard deviation about the mean. The most negative velocity emission comes from the Magellanic Stream. The emission summed in the Galactic Center system has a mean velocity closest to zero and the smallest dispersion of the three (see Table 6).

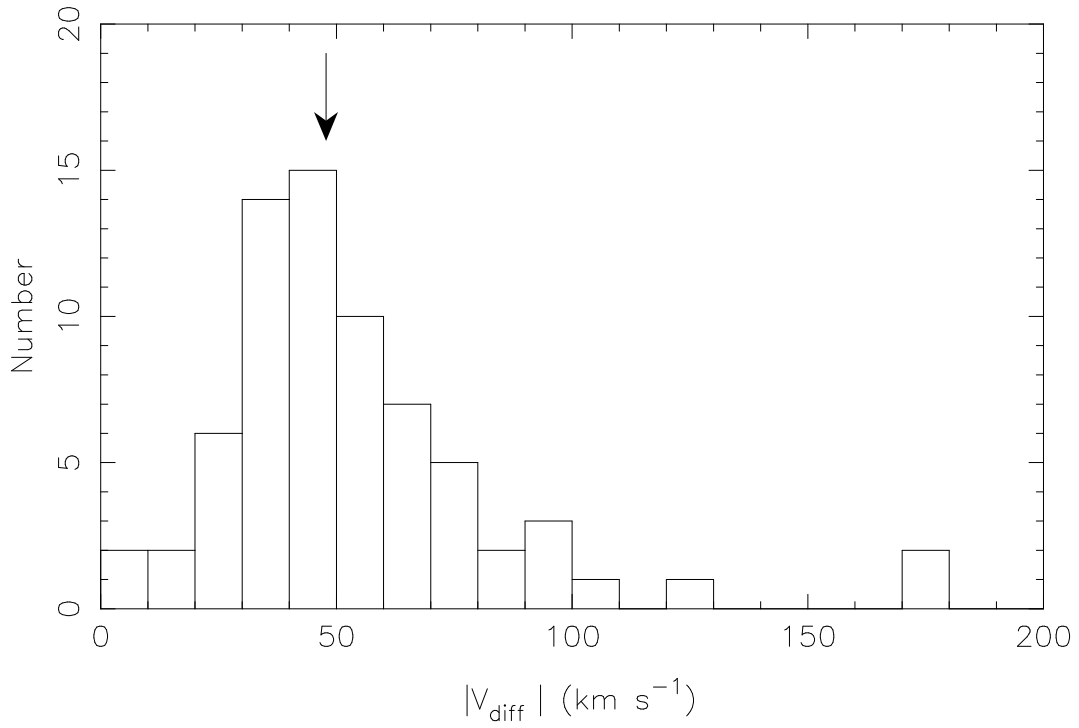


Fig. 16.— The distribution of the difference in V_{LSR} between high-velocity lines which appear in the same spectrum. The arrow marks the median, 48 km s⁻¹. There are few lines with very small values of $|V_{diff}|$, which might be seen from clouds having a core-halo structure.

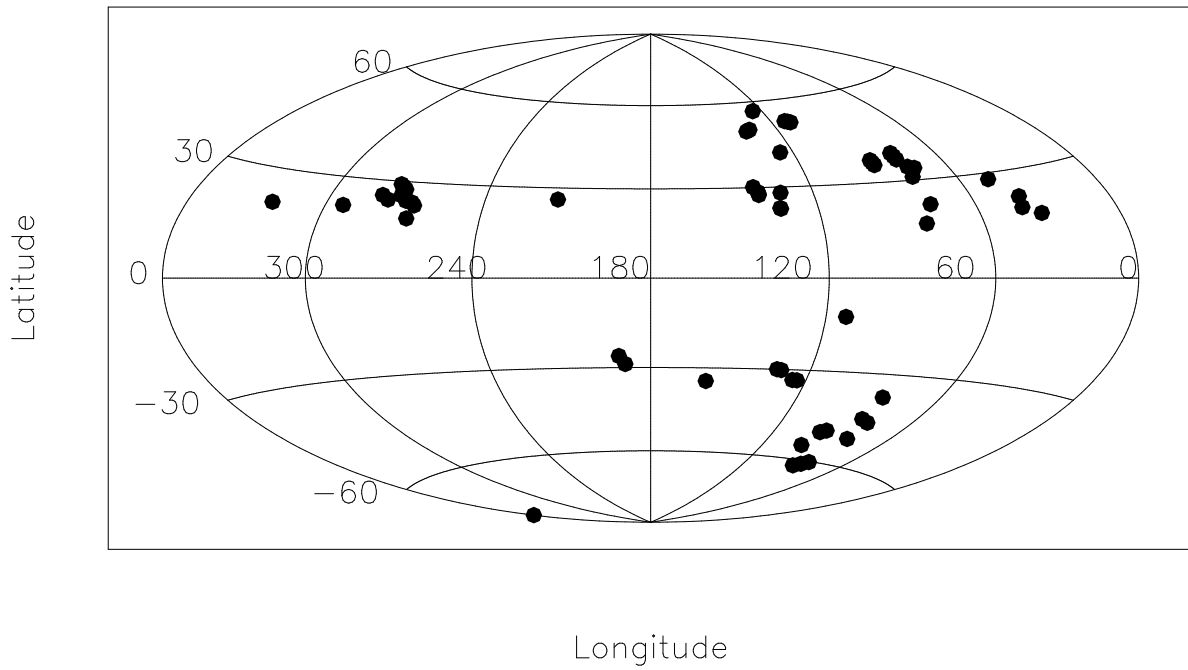


Fig. 17.— The location of directions with multiple high-velocity H I lines in a single spectrum. Most of the multiple lines appear to arise from internal structure in large high-velocity complexes. The Magellanic Stream, Complex C, Complex A, and Wright's Cloud are all represented here.

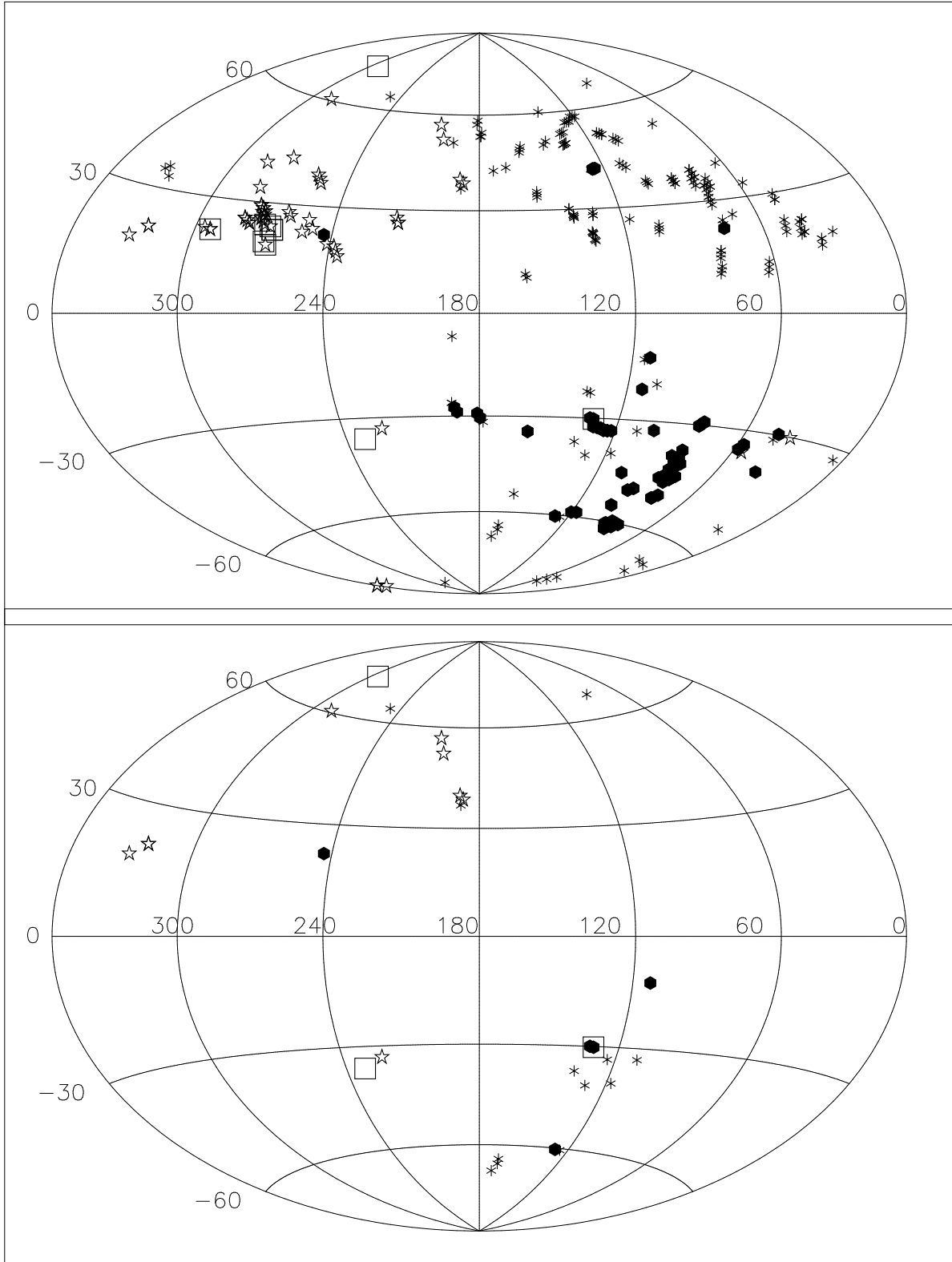


Fig. 18.— Upper panel: All high-velocity Gaussian components. Filled symbols mark lines with $V_{LSR} < -200 \text{ km s}^{-1}$, asterisks mark V_{LSR} in the range -200 to -100 km s^{-1} , open stars $+100$ to $+200 \text{ km s}^{-1}$, and open rectangles $> +200 \text{ km s}^{-1}$. The association of lines into coherent complexes is evident. Lower panel: Same as the upper panel only for lines which could not be assigned to one of the large complexes.

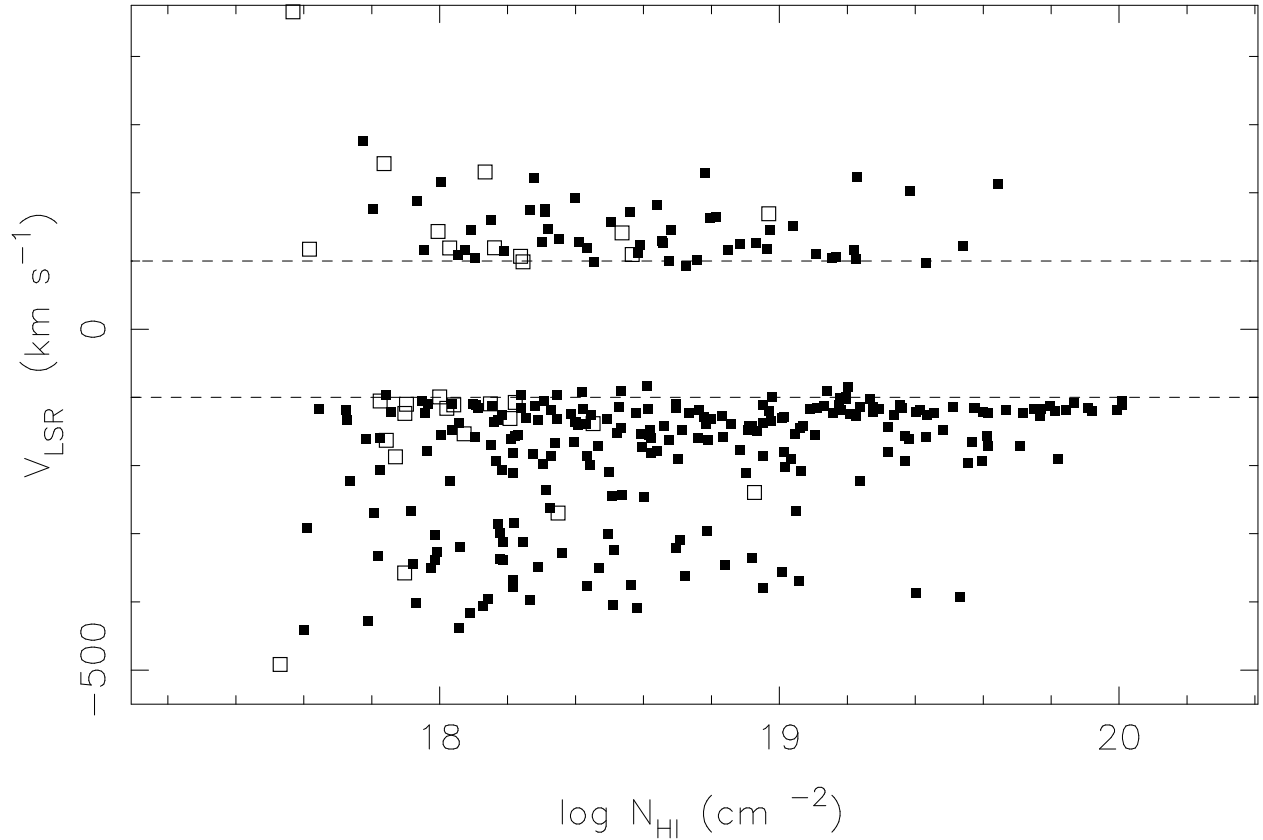


Fig. 19.— The LSR velocity vs. N_{HI} of the Gaussian components from Table 4, where filled symbols identify lines associated or possibly associated with a large high-velocity complex, and open symbols are lines not associated with a known complex. The reality of the lines at +465 and -500 km s^{-1} is suspect, and there is one suspect line with $V_{LSR} \sim -700 \text{ km s}^{-1}$ and $\log(N_{HI}) = 17.6$ which is not plotted (see §3.4).

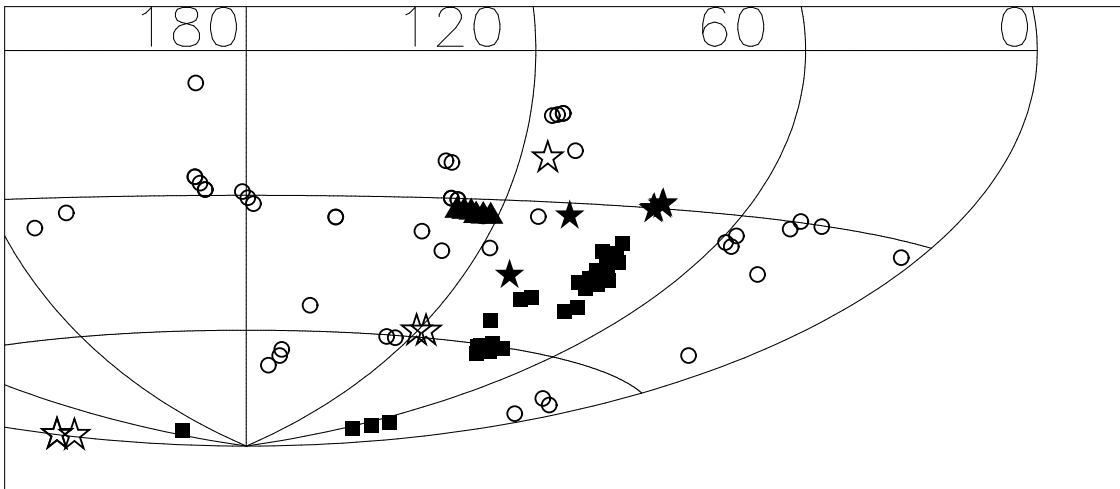


Fig. 20.— An Aitoff projection in Galactic coordinates of high-velocity H I lines near the Magellanic Stream. Lines within the traditional borders of the Stream are filled squares, and those probably unrelated to the Stream because of their velocity are open circles. The lines marked by filled stars show emission detected in this survey which traces an extension of the Stream to higher latitude and longitude. These weak lines, listed as MS* in Table 4, would not have been detected in previous surveys. The open stars are lines which might be part of the Stream, but their association is less certain (MS?). Filled triangles mark lines from Wright’s cloud near M33, which is considerably more extended in our data than in earlier studies.

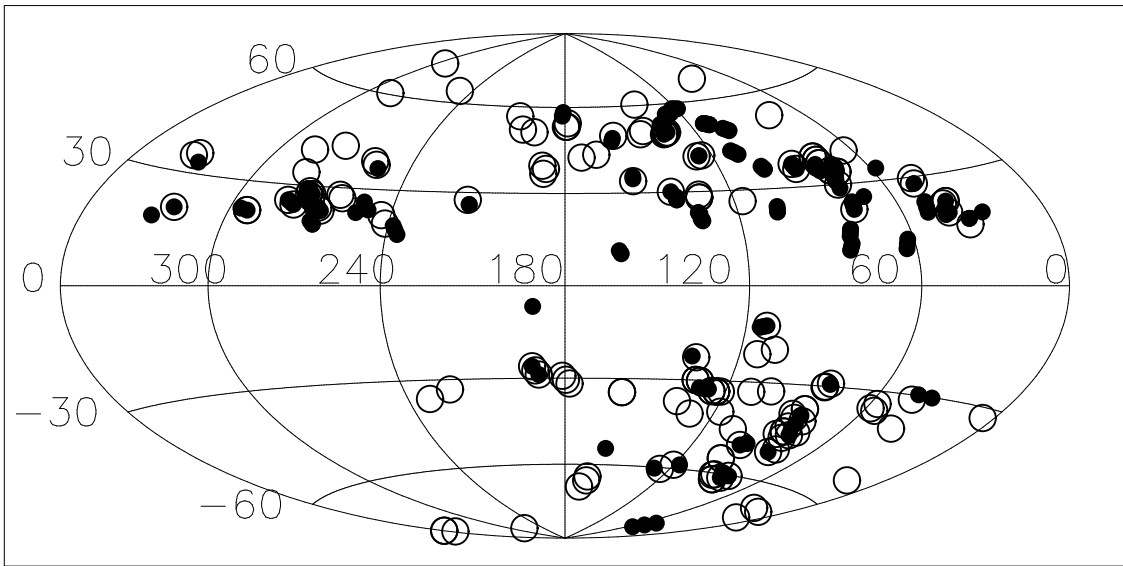


Fig. 21.— All the high velocity lines from Table 4 sorted by their total N_{HI} . The brightest half of the lines ($> 3.5 \times 10^{18} \text{ cm}^{-2}$) are the filled symbols and the faintest half the open symbols. Although there are some chance superpositions of clouds at different velocities, lines in similar parts of the sky tend to have similar velocities (Fig. 18), and in many instances the faint lines surround and connect bright lines.

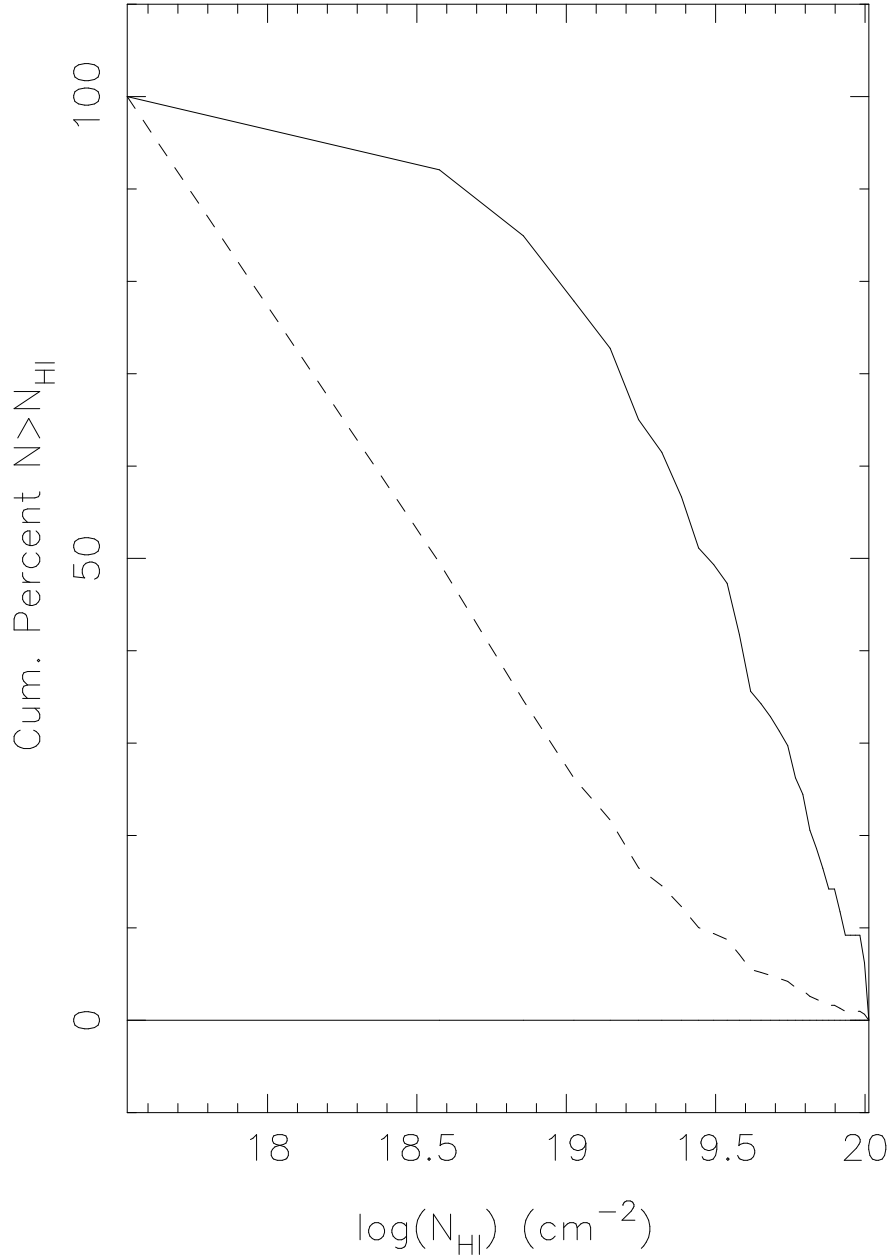


Fig. 22.— The cumulative distribution of the numbers of detected high-velocity lines (dashed curve) and the total N_{HI} that they contain (solid curve) for all lines above the given value of $\log(N_{HI})$. Most of the lines have a low column density, but most of the atoms reside in lines with the highest N_{HI} .

Table 1. Observed Central Positions

Object Name	α (B1950)	δ (B1950)	l	b
UM 18	00 02 46	05 07 29	102.310	–55.612
PKS 0003+15	00 03 25	15 53 08	107.318	–45.325
PKS 0005–239	00 05 27	–23 55 59	50.039	–79.599
III ZW 2	00 07 55	10 42 02	106.970	–50.620
4C 40.01	00 10 54	40 34 57	115.241	–21.444
Q 0022+0015	00 22 10	00 15 44	108.786	–61.597
NAB 0024+22	00 24 38	22 25 24	115.663	–39.830
5C 03.44	00 34 54	39 21 42	120.037	–23.157
PKS 0035–39	00 36 02	–39 16 11	314.979	–77.828
E 0039–0158	00 39 47	–01 58 17	117.646	–64.476
PG 0043+039	00 43 11	03 54 42	120.207	–58.656
PKS 0044+030	00 44 31	03 03 34	120.796	–59.521
Q 0050–253	00 50 18	–25 23 07	131.311	–87.964
B2 0051+29	00 51 02	29 08 54	123.532	–33.450
PHL 909	00 54 32	14 30 00	125.004	–48.078
UM 301	01 00 38	02 05 07	128.892	–60.382
B2 0106+38	01 06 37	38 00 48	126.813	–24.456
0107–3310	01 07 58	–33 06 05	268.477	–82.982
B2 0110+29	01 10 38	29 42 24	128.582	–32.659
E 0111+388	01 11 01	38 51 27	127.673	–23.543
PG 0117+213	01 17 35	21 18 05	131.806	–40.811
II ZW 1	01 19 26	–01 17 57	139.889	–62.900
PKS 0119–04	01 19 56	–04 37 07	142.297	–66.056
MARK 992	01 22 00	31 51 45	131.106	–30.219
PKS 0122–00	01 22 55	–00 21 30	141.157	–61.760
UM 328	01 26 24	–01 35 16	143.721	–62.677
PKS 0130+24	01 30 39	24 12 20	134.980	–37.426
UM 341	01 31 44	00 00 18	145.290	–60.737
3C 48	01 34 50	32 54 21	133.962	–28.719
NAB 0137–01	01 37 44	–01 05 12	148.981	–61.211
B2 0141+33	01 41 18	33 56 55	135.206	–27.412
TEX 0145+386	01 45 26	38 39 11	134.904	–22.642
KUV 0150–074	01 50 41	–07 43 41	162.452	–65.499
PHL 1226	01 51 52	04 33 39	150.795	–54.620
UM 381	01 54 37	–02 02 03	157.563	–60.167
MARK 1014	01 57 16	00 09 12	156.567	–57.939
3C 57	01 59 30	–11 46 59	173.076	–67.262

Table 1—Continued

Object Name	α (B1950)	δ (B1950)	l	b
KUV 0201–08	02 00 58	–08 58 13	169.068	–64.936
NAB 0205+02	02 05 14	02 28 43	157.599	–54.930
0214–033	02 14 57	–03 21 50	167.250	–58.395
PKS 0215+015	02 15 14	01 31 02	162.139	–54.413
B3 0219+443	02 19 06	44 19 21	139.514	–15.377
PKS 0219–164	02 19 38	–16 28 54	190.193	–66.374
PKS 0232–04	02 32 36	–04 15 09	174.461	–56.156
4C 41.04	02 32 46	41 10 15	143.179	–17.339
EX 0240+007	02 40 04	00 43 45	171.065	–51.230
US 3150	02 44 19	–01 12 02	174.427	–51.930
MS 02448+192	02 44 52	19 28 25	157.052	–35.374
S4 0248+43	02 48 18	43 02 55	145.041	–14.401
US 3472	02 57 03	00 25 44	176.180	–48.533
MS 0302–2223	03 02 36	–22 23 28	211.082	–59.387
0316–346	03 16 08	–34 37 28	235.207	–57.846
NGC 1275	03 16 30	41 19 53	150.575	–13.261
DW 0326+27	03 26 56	27 46 03	160.702	–23.074
0330–368	03 30 14	–36 45 00	238.750	–54.867
NRAO 140	03 33 22	32 08 38	158.999	–18.765
MS 03342–361	03 34 15	–36 17 24	237.887	–54.085
3C 95	03 49 10	–14 38 07	205.485	–46.325
3C 94	03 50 04	–07 19 54	196.557	–42.724
MS 03574+104	03 57 27	10 46 48	179.648	–30.496
PKS 0405–12	04 05 28	–12 19 30	204.962	–41.756
3C 110	04 14 49	–06 01 02	199.126	–36.757
PKS 0420–01	04 20 43	–01 27 28	195.289	–33.140
3C 120	04 30 32	05 15 00	190.373	–27.397
S5 0437+78	04 38 00	78 33 24	133.285	20.840
PKS 0439–433	04 39 42	–43 19 01	247.971	–41.387
IR 0450–2958	04 50 33	–29 58 29	231.129	–37.586
PKS 0454–22	04 54 02	–22 03 54	221.982	–34.647
PKS 0454+039	04 54 09	03 56 18	195.163	–23.198
MS 04579–05	04 57 58	–05 55 56	205.145	–27.313
1E 0514–0030	05 14 00	00 30 31	201.080	–20.699
PKS 0514–16	05 14 01	–16 06 23	217.438	–28.108
MS 05217+79	05 21 44	79 18 40	133.783	23.018
Q 0530–379	05 30 49	–37 55 22	242.710	–31.143

Table 1—Continued

Object Name	α (B1950)	δ (B1950)	l	b
MS 05374–28	05 37 26	–28 43 34	232.938	–27.412
3C 147	05 38 43	49 49 46	161.686	10.298
4C 16.14	05 48 25	16 35 58	191.260	–5.211
A 34.09	06 08 01	–35 14 53	242.003	–23.238
3C 154	06 10 44	26 05 31	185.594	4.007
HS 0624+6907	06 24 35	06 07 35	204.747	–2.565
B2 0709+37	07 09 48	37 01 18	180.771	19.958
3C 175	07 10 15	11 51 24	204.783	10.080
MARK 380	07 13 29	74 33 27	140.441	27.956
3C 184 ^a	07 29 23	81 52 42	132.109	28.527
3C 185	07 36 02	–01 57 28	220.226	9.504
PKS 0736+01	07 36 42	01 44 03	216.989	11.380
OI 363	07 38 00	31 19 03	188.637	23.587
3C 186	07 40 57	38 00 34	181.786	26.141
B2 0742+31	07 42 31	31 50 17	188.429	24.662
PKS 0743+006	07 43 21	00 36 58	218.790	12.328
B2 0749+37	07 49 09	37 58 37	182.289	27.694
KUV 07549+42	07 54 53	42 27 44	177.581	29.760
MARK 1413 ^a	07 58 04	73 19 05	141.670	31.096
0804+761	08 04 32	76 11 32	138.280	31.030
MS 08080+484	08 08 01	48 40 28	170.775	32.938
3C 196	08 09 59	48 22 11	171.173	33.236
4CP 62.12	08 21 23	62 07 17	154.556	34.724
MS 08220+030	08 22 06	03 09 50	221.223	22.065
B3 0284+397	08 24 48	39 45 39	181.875	34.848
B2 0827+24	08 27 54	24 21 08	200.021	31.876
0830+112	08 30 36	11 15 31	214.309	27.601
PG 0832+251	08 32 37	25 10 08	199.490	33.147
US 1329	08 33 34	44 36 31	176.141	36.988
4C 19.31	08 36 15	19 32 28	206.130	32.095
PKS 0837–12	08 37 28	–12 03 52	237.172	17.430
CSO 199	08 38 07	35 55 21	187.063	36.836
DW 0839+18	08 39 14	18 46 28	207.275	32.480
TON 951	08 44 34	34 56 10	188.563	37.965
LB 8741	08 47 38	19 05 03	207.777	34.448
US 1867	08 50 14	44 00 29	177.082	39.938
3C 208	08 50 23	14 04 16	213.661	33.158

Table 1—Continued

Object Name	α (B1950)	δ (B1950)	l	b
OJ 287	08 51 57	20 18 01	206.811	35.821
US 2068	08 56 00	46 48 59	173.386	40.940
PKS 0859–14	08 59 55	–14 03 37	242.252	20.721
MS 09063+11	09 06 20	11 11 41	218.798	35.489
SBS 0909+53	09 09 30	53 12 00	164.576	42.414
4C 05.38	09 11 24	05 20 16	225.814	33.875
NGC 2841 UB3	09 18 35	51 11 19	166.944	44.149
PG 0923+201	09 23 06	20 07 09	210.175	42.650
PKS 0925–203	09 25 34	–20 21 43	251.637	21.423
RO2.37	09 31 20	–16 55 41	249.869	24.742
US 737	09 31 51	43 44 39	177.058	47.438
PG 0935+416	09 35 49	41 41 55	180.001	48.342
PG 0946+301	09 46 46	30 09 19	197.831	50.237
PG 0953+415	09 53 48	41 30 00	179.777	51.709
3C 232	09 55 25	32 38 25	194.171	52.322
MARK 132	09 58 08	55 09 07	158.904	48.624
0959+68W1	09 59 09	68 27 49	142.464	41.952
TON 28	10 01 12	29 13 00	200.006	53.218
PKS 1004–217	10 04 25	–21 44 42	259.800	26.776
MS 10067+814 ^a	10 06 37	81 45 23	129.425	33.511
4C 41.21	10 07 26	41 47 24	178.641	54.178
PKS 1009–321	10 09 42	–32 08 45	267.901	19.417
PKS 1011–282	10 11 12	–28 16 30	265.661	22.691
Q 1013+0124	10 13 22	01 24 12	241.172	44.583
Ton 34	10 17 06	27 59 01	202.957	56.507
B3 1019+397	10 19 40	39 47 03	181.380	56.821
PKS 1020–103	10 20 04	–10 22 33	254.161	37.764
PKS 1034–29	10 34 56	–29 18 24	270.951	24.847
4C 06.41	10 38 41	06 25 59	241.113	52.652
S5 1039+81 ^a	10 39 28	81 10 25	128.739	34.736
IRAS 1047–28	10 47 55	–28 07 44	272.971	27.338
PKS 1049–09	10 48 59	–09 02 10	260.186	43.395
PG 1049–005	10 49 18	–00 35 20	252.275	49.878
4C 61.20	10 49 22	61 41 21	144.759	50.366
IRAS 1051–27	10 51 09	–27 22 53	273.248	28.343
3C 249.1	11 00 27	77 15 10	130.393	38.549
PKS 1101–325	11 01 08	–32 35 03	278.115	24.765

Table 1—Continued

Object Name	α (B1950)	δ (B1950)	l	b
MRK 421	11 01 40	38 28 49	179.829	65.029
MC 1104+167	11 04 37	16 44 19	231.392	63.644
PG 1116+167	11 16 30	21 35 44	223.359	68.210
PKS 1117–248	11 17 41	–24 51 41	278.091	33.295
1119+120	11 19 11	12 00 47	244.753	63.938
US 2450	11 24 57	27 11 26	208.775	71.350
PKS 1127–14	11 27 35	–14 32 53	275.279	43.638
1130+106Y	11 30 55	11 09 00	250.753	65.502
PKS 1136–13	11 36 38	–13 34 05	277.524	45.432
3C 263.0	11 37 09	66 04 29	134.159	49.743
PG 1148+549	11 48 42	54 54 16	140.614	60.391
B2 1148+38	11 48 53	38 42 36	167.154	73.114
4C 63.15	11 56 04	63 11 10	132.921	53.185
4C 29.45	11 56 58	29 31 29	199.410	78.374
J 08.06	11 57 07	–19 42 41	286.681	41.243
1202+281	12 02 11	28 10 56	205.958	79.620
PG 1206+459	12 06 26	45 57 19	144.628	69.620
PKS 1207–399	12 06 59	–39 59 27	294.343	21.904
B2 1208+32A	12 08 05	32 13 50	181.959	79.904
PG 1211+143	12 11 45	14 19 54	267.550	74.315
PKS 1216–010	12 16 01	–01 03 14	286.091	60.461
PG 1216+069	12 16 47	06 55 21	281.063	68.143
MARK 205 ^a	12 19 33	75 35 15	125.447	41.673
3C 273	12 26 33	02 19 46	289.948	64.361
HS 1227+453	12 27 03	45 30 16	135.114	71.377
T 1542	12 29 33	20 26 06	269.436	81.740
Q 1230+0947	12 30 54	09 47 54	288.511	71.888
SBS 1234+607	12 34 06	60 47 00	126.296	56.521
PKS 1240–294	12 40 30	–29 26 56	300.790	33.115
PG 1241+176	12 41 41	17 37 29	292.826	80.080
PG 1248+401	12 48 27	40 08 00	123.483	77.266
PKS 1252+11	12 52 08	11 57 24	305.870	74.539
PG 1254+047	12 54 27	04 43 50	306.525	67.293
B 201	12 57 27	34 39 33	109.541	82.519
PG 1259+593	12 59 08	59 18 15	120.556	58.048
PKS 1302–102	13 02 56	–10 17 16	308.591	52.161
PG 1307+085	13 07 16	08 35 48	316.786	70.707

Table 1—Continued

Object Name	α (B1950)	δ (B1950)	l	b
B2 1308+32	13 08 08	32 36 43	85.705	83.345
TON 153	13 17 34	27 43 55	37.651	83.662
TON 156	13 18 55	29 03 02	48.815	83.209
PKS 1327–21	13 27 23	–21 26 31	314.737	40.284
PG 1333+176	13 33 37	17 40 33	351.925	75.850
PG 1338+416	13 38 52	41 38 19	90.584	72.484
1351+640	13 51 47	64 00 28	111.890	52.020
PG 1352+011	13 52 26	01 06 53	335.712	59.635
MRK 463	13 53 40	18 37 00	5.824	72.747
PKS 1354+19	13 54 42	19 33 46	8.993	73.042
PG 1358+04	13 58 00	04 19 29	341.537	61.662
1E 1401+0952	14 01 43	09 52 01	350.809	65.489
CSO 409	14 02 38	43 41 30	85.500	67.973
PG 1402+261	14 02 59	26 10 00	32.961	73.459
PG 1407+265	14 07 08	26 32 31	34.669	72.589
1411+422	14 11 51	44 14 24	83.831	66.350
PG 1415+451	14 13 04	45 10 01	85.264	65.597
M16.11	14 14 04	–25 10 18	326.206	33.576
PKS 1421–38	14 21 12	–38 13 11	322.227	20.923
MRK 813	14 25 06	20 03 18	19.701	66.861
B2 1425+26	14 25 22	26 45 40	36.868	68.574
PKS 1435–218	14 35 18	–21 51 55	333.228	34.436
S4 1435+63	14 35 37	63 49 38	105.175	49.729
PG 1444+407	14 44 50	40 47 41	69.900	62.717
PKS 1451–375	14 51 18	–37 35 21	328.227	18.964
3C 309 ^a	14 58 56	71 52 12	109.983	42.097
PKS 1510–08	15 10 09	–08 54 45	351.289	40.140
B2 1512+37	15 12 47	37 01 57	59.856	58.315
PG 1522+101	15 22 00	10 09 04	14.892	50.122
EX 1526+285	15 26 38	28 36 00	44.441	55.342
PKS 1538+477	15 38 01	47 45 16	76.448	51.488
PG 1543+489	15 44 00	48 55 31	77.779	50.202
3C 334	16 18 07	17 43 31	33.161	41.109
PG 1630+377	16 30 15	37 44 08	60.342	42.939
PG 1634+706	16 34 52	70 37 39	102.843	36.644
3C 345	16 41 17	39 54 11	63.455	40.949
1641.7+399	16 41 45	39 58 47	63.564	40.867

Table 1—Continued

Object Name	α (B1950)	δ (B1950)	l	b
PKS 1656+053	16 56 06	05 19 49	24.300	27.441
PG 1700+518	17 00 13	51 53 38	79.020	37.771
3C 351	17 04 03	60 48 31	90.084	36.382
PG 1715+535	17 15 31	53 31 25	80.966	35.410
PG 1718+481	17 18 17	48 07 11	74.375	34.829
V 396 Her	17 20 37	24 39 06	47.194	29.699
B2 1721+34	17 21 32	34 20 42	58.126	32.185
PKS 1725+044	17 25 56	04 29 28	27.294	20.478
4C50.43	17 29 49	50 09 45	76.990	33.092
MC 1745+163	17 45 55	16 20 13	40.996	21.160
OT 081	17 49 10	09 39 45	34.920	17.646
IRAS 1750+50	17 50 05	50 46 21	78.099	29.950
MC3 1750+17	17 50 33	17 34 59	42.691	20.641
PKS 1756+237	17 56 56	23 43 55	49.395	21.610
OU 401	18 00 03	44 04 20	70.943	27.084
KAZ 102	18 03 37	67 37 56	97.622	29.474
H 18217+643	18 21 42	64 19 03	94.003	27.417
3C 380.0	18 28 13	48 42 39	77.225	23.505
3C 395	19 01 02	31 55 13	63.028	11.757
IRAS 1910+84 ^a	19 10 24	84 36 53	116.992	26.769
4C 50.47	19 24 49	50 46 54	82.571	15.615
4C 73.18 ^a	19 28 49	73 51 47	105.626	23.541
Tex 1951+498	19 51 12	49 50 24	83.662	11.433
MS 20078–36	20 07 53	–36 22 04	5.097	–30.940
MS 20345–22	20 34 35	–22 53 15	22.241	–32.860
M509+U430 ^b	20 43 41	–10 24 05	36.770	–30.134
PKS 2044–168	20 44 31	–16 50 08	29.967	–32.934
MS 20532–50	20 53 16	–05 03 11	43.513	–29.793
PKS 2059+034	20 59 08	03 29 41	52.690	–26.648
PG 2112+059	21 12 23	05 55 14	57.040	–28.014
PKS 2115–30	21 15 11	–30 31 48	15.744	–43.563
Tex 2116+203	21 16 17	20 21 22	70.090	–19.802
3C 432	21 20 25	16 51 44	67.935	–22.825
PKS 2128–12	21 28 53	–12 20 18	40.539	–40.956
PKS 2134+004	21 34 05	00 28 26	55.473	–35.577
PKS 2135–14	21 35 01	–14 46 27	38.402	–43.333
RXJ 21397+02	21 37 12	02 32 28	58.087	–35.006

Table 1—Continued

Object Name	α (B1950)	δ (B1950)	l	b
OX 169	21 41 13	17 30 03	72.115	–26.084
PKS 2145+06	21 45 36	06 43 43	63.656	–34.071
PKS 2155–304	21 55 58	–30 27 54	17.731	–52.245
WA495	21 59 58	00 07 50	60.000	–40.999
B2 2201+31A	22 01 01	31 31 08	85.957	–18.778
PKS 2223+21	22 23 15	21 02 53	83.160	–30.087
MS 22241+20	22 24 07	20 56 29	83.273	–30.296
PG 2233+134	22 33 40	13 28 22	79.898	–37.586
PKS 2243–123	22 43 40	–12 22 39	53.868	–57.071
PKS2247+14	22 47 56	14 03 58	83.889	–39.196
2251–178	22 51 24	–17 50 57	46.191	–61.320
3C 454.3	22 51 29	15 52 56	86.111	–38.183
PKS 2251+11	22 51 40	11 20 40	82.783	–41.940
PKS 2254+074	22 54 46	07 27 11	80.425	–45.521
PKS 2255–282	22 55 22	–28 14 25	24.387	–64.920
PG 2302+029	23 02 12	02 55 35	78.455	–50.230
4C 09.72	23 08 46	09 51 59	86.450	–45.521
PKS 2310–322	23 10 28	–32 14 06	14.246	–68.139
3C 463	23 25 28	26 59 23	100.999	–32.026
4C 29.68	23 25 42	29 20 39	102.065	–29.856
B3 2327+407	23 27 43	40 47 53	106.831	–19.242
PKS 2340–036	23 40 22	–03 39 04	85.401	–61.151
PKS 2344+09	23 44 04	09 14 07	97.503	–50.131
PKS 2349–01	23 49 22	–01 25 52	91.665	–60.361
UM 186	23 50 48	–01 32 08	92.211	–60.618
PKS 2352–342	23 52 50	–34 14 37	359.941	–76.156
B2 2353+28	23 53 21	28 19 17	108.433	–32.704
4C 49.48	23 55 37	49 05 03	114.089	–12.592

Note. — Units of right ascension are hours, minutes, and seconds, and units of declination are degrees, arcminutes, and arcseconds. Units of Galactic longitude and latitude are degrees.

^aFlanking positions offset 13^m.5 in right ascension.

^bFlanking position at lower right ascension only.

Table 2. Summary of Experimental Parameters.

Mode	Hann ^a	ch. width ^b (km s ⁻¹)	median σ_b (mK)	Vel. coverage (km s ⁻¹)	Numb.
Pos-Sw	Y	10.0	3.1	1800	574
Pos-Sw	N	5.0	5.1	1800	221
Freq-Sw	Y	2.5	10.6	450	16
Freq-Sw	N	1.25	22.5	450	49

^aIs spectrum Hanning smoothed?

^bEffective velocity width of a single spectral channel.

Table 3. Detections of High-Velocity Hydrogen

#	Object	α (B1950)	δ (B1950)	l (deg)	b (deg)	T_{peak} (mK)	Δv (km s ⁻¹)	V_{LSR} (km s ⁻¹)	σ_g (mK)	σ_b (mK)	N_{HI} (10 ¹⁹)	$\langle V \rangle$ (km s ⁻¹)	Notes
1	B2 2353+28+	00 00 14	28 19 16	110.181	-33.065	21.0(2.0)	25.7(3.3)	-116.2(1.3)	2.3	3.2			H
2	4C 49.48+	00 02 29	49 05 04	115.219	-12.813	174.0(4.1)	31.9(0.8)	-190.0(0.4)	5.7	2.4			H,A
3	4C 49.48+	00 02 29	49 05 04	115.219	-12.813					2.4	0.27	-116	H,A
4	PKS 0003+15	00 03 25	15 53 08	107.318	-45.325	17.0(2.1)	29.8(4.2)	-326.9(1.8)	2.8	2.4			H
5	4C 40.01-	00 04 02	40 34 58	113.861	-21.220	13.3(1.4)	33.0(1.0)	-402.0(0.4)	1.9	2.4			H
6	4C 40.01-	00 04 02	40 34 58	113.861	-21.220	29.0(0.0)	100.0(0.0)	308.0(0.0)	0.0	2.4			UGC 00064
7	PKS 0005-239	00 05 27	-23 55 59	50.039	-79.599	835.0(11.0)	38.5(0.6)	-112.4(0.3)	49.0	45.0			F
8	PKS 0005-239+	00 12 19	-23 55 59	53.723	-81.042	570.0(10.0)	47.1(1.0)	-123.3(0.4)	48.0	43.0			F
9	Q 0022+0015-	00 15 18	00 15 44	105.307	-61.178					5.0	0.08	-100	H,A
10	4C 40.01+	00 17 47	40 34 58	116.629	-21.632					2.6	0.25	-117	H
11	Q 0022+0015	00 22 10	00 15 44	108.786	-61.597					4.5	0.13	-110	H,A
12	5C 03.44-	00 28 02	39 21 42	118.597	-23.059					2.8	0.60	-108	H,U
13	Q 0022+0015+	00 29 02	00 15 42	112.350	-61.926					4.4	0.09	-102	H,A
14	NAB 0024+22+	00 31 31	22 25 23	117.721	-39.980	33.0(1.4)	25.1(1.1)	-130.9(0.4)	1.6	2.3			H
15	E 0039-0158-	00 32 54	-01 58 16	113.700	-64.281					4.3	0.43	-165	H,A,U
16	5C 03.44	00 34 54	39 21 42	120.037	-23.157	3107.0(0.0)	185.0(0.0)	-512.0(0.0)	0.0	2.9			M31
17	PG 0043+039-	00 36 18	03 54 44	116.926	-58.539	178.6(2.4)	29.5(0.5)	-355.6(0.2)	4.6	5.0			
18	E 0039-0158	00 39 47	-01 58 17	117.646	-64.476					5.1	0.40	-148	H,A,U
19	5C 03.44+	00 41 47	39 21 42	121.481	-23.217	21.0(0.0)	235.0(0.0)	-475.0(0.0)	0.0	2.8			M31
20	PG 0043+039	00 43 11	03 54 42	120.207	-58.656	17.6(2.3)	47.9(7.2)	-367.8(3.1)	5.6	5.6			
21	B2 0051+29-	00 44 10	29 08 53	121.734	-33.440	16.8(1.1)	35.2(2.8)	-319.5(1.3)	1.8	3.7			H,A
22	B2 0051+29-	00 44 10	29 08 53	121.734	-33.440					3.7	0.13	-109	H,A
23	E 0039-0158+	00 46 39	-01 58 18	121.632	-64.565					4.4	0.44	-172	H,A,U
24	B2 0051+29	00 51 02	29 08 54	123.532	-33.450	29.3(1.7)	26.4(1.8)	-336.7(0.8)	2.2	3.2			H,A
25	B2 0051+29	00 51 02	29 08 54	123.532	-33.450	12.2(2.1)	17.2(3.7)	-291.4(1.6)	2.2	3.2			H,A
26	B2 0051+29	00 51 02	29 08 54	123.532	-33.450	11.6(1.7)	30.9(5.4)	-163.0(2.3)	2.2	3.2			H,A
27	B2 0051+29	00 51 02	29 08 54	123.532	-33.450					3.2	0.11	-113	H,A
28	UM 301-	00 53 46	02 05 07	125.420	-60.492	13.7(2.5)	29.7(7.4)	-123.6(2.8)	3.3	3.2			H,U
29	B2 0051+29+	00 57 54	29 08 54	125.329	-33.412	32.3(2.4)	29.3(2.8)	-397.4(1.1)	3.1	4.2			H,A
30	B2 0051+29+	00 57 54	29 08 54	125.329	-33.412	33.5(2.3)	30.0(2.7)	-349.4(1.1)	3.1	4.2			H,A
31	UM 301	01 00 38	02 05 07	128.892	-60.382	182.0(2.7)	23.9(0.4)	-239.6(0.1)	3.2	3.4			H
32	0107-3310-	01 01 20	-33 06 04	278.732	-83.709	48.2(2.7)	36.5(2.5)	-145.4(1.0)	7.7	9.2			F,H
33	B2 0110+29-	01 03 46	29 42 22	126.815	-32.785	226.0(7.0)	26.0(1.0)	-368.7(0.4)	25.3	23.9			F
34	B2 0110+29	01 10 38	29 42 24	128.582	-32.659	501.0(7.0)	25.9(0.4)	-386.7(0.2)	23.4	25.0			F
35	PG 0117+213-	01 10 42	21 18 06	129.706	-41.016	24.1(1.4)	35.6(2.5)	-107.5(1.0)	1.8	2.9			H

Table 3—Continued

#	Object	α (B1950)	δ (B1950)	l (deg)	b (deg)	T_{peak} (mK)	Δv (km s ⁻¹)	V_{LSR} (km s ⁻¹)	σ_g (mK)	σ_b (mK)	N_{HI} (10 ¹⁹)	$\langle V \rangle$ (km s ⁻¹)	Notes
36	II ZW 1-	01 12 34	-01 17 58	136.196	-63.296					3.1	0.09	-134	H
37	B2 0110+29+	01 17 31	29 42 25	130.341	-32.487	1040.0(10.0)	16.9(0.2)	-392.9(0.1)	30.4	25.4			F
38	MARK 992	01 22 00	31 51 45	131.106	-30.219	9.3(1.6)	18.8(3.5)	-491.8(1.6)	1.7	2.9			H
39	MARK 992	01 22 00	31 51 45	131.106	-30.219	9.2(2.1)	20.7(5.4)	465.3(2.3)	2.3	2.9			H
40	MARK 992	01 22 00	31 51 45	131.106	-30.219					2.9	0.10	-112	H,U
41	MARK 992+	01 28 52	31 51 45	132.770	-29.982	20.3(1.3)	56.7(4.9)	-269.7(2.0)	2.4	2.4			H
42	MARK 992+	01 28 52	31 51 45	132.770	-29.982	8.0(1.4)	47.7(13.6)	-187.2(4.7)	2.4	2.4			H,U
43	PKS 0130+24+	01 37 31	24 12 20	136.901	-37.084	20.8(1.3)	34.9(0.6)	-109.6(0.3)	1.8	2.8			H
44	TEX 0145+386	01 45 26	38 39 11	134.904	-22.642	28.8(2.3)	29.0(2.5)	-161.3(1.1)	2.9	2.8			H
45	B2 0141+33+	01 48 11	33 56 55	136.762	-27.069					2.0	0.10	-122	H
46	TEX 0145+386+	01 52 19	38 39 11	136.311	-22.309	68.4(2.3)	31.6(1.3)	-160.0(0.6)	3.2	2.7			H
47	3C 57-	01 52 38	-11 46 59	169.802	-68.403	15.4(1.0)	39.3(2.8)	-153.5(1.1)	1.4	2.4			H
48	3C 57-	01 52 38	-11 46 59	169.802	-68.403					2.4	0.01	-107	H
49	KUV 0201-08-	01 54 05	-08 58 11	165.891	-66.005	40.0(2.8)	36.5(3.1)	-138.6(1.3)	4.4	4.0			H
50	KUV 0150-074+	01 57 34	-07 43 41	165.708	-64.497	18.9(2.7)	30.1(5.1)	-111.1(4.8)	6.7	5.7			H
51	NAB 0205+02+	02 12 07	02 28 44	160.121	-54.037	234.0(5.6)	30.3(0.8)	-90.9(0.4)	10.7	5.9			
52	MS 02448+192+	02 51 44	19 28 24	158.717	-34.502	28.2(1.3)	32.1(2.3)	-311.7(1.0)	1.7	2.0			H
53	MS 02448+192+	02 51 44	19 28 24	158.717	-34.502	12.0(1.1)	35.3(5.7)	-266.0(2.3)	1.7	2.0			H
54	S4 0248+43+	02 55 11	43 03 00	146.184	-13.813					3.8	0.13	-151	H
55	NGC 1275+	03 23 08	41 19 54	151.637	-12.567					2.4	0.13	-131	H
56	NRAO 140-	03 26 30	32 03 38	157.775	-19.648					2.6	0.06	-113	H
57	NRAO 140	03 33 22	32 08 38	158.999	-18.765					2.3	0.06	-94	H
58	MS 03574+104-	03 50 35	10 46 47	178.342	-31.761	7.1(1.4)	28.1(6.8)	-236.9(2.8)	1.9	3.7			H,A
59	MS 03574+104-	03 50 35	10 46 47	178.342	-31.761	15.2(1.7)	20.5(2.7)	-160.6(1.1)	1.9	3.7			H,A
60	MS 03574+104	03 57 27	10 46 48	179.648	-30.496	25.8(2.0)	68.8(6.2)	-243.6(2.7)	4.2	3.9			H,A
61	MS 03574+104+	04 04 19	10 46 47	180.912	-29.214	39.8(2.5)	41.7(3.1)	-244.8(1.3)	4.1	3.6			H,A
62	3C 120-	04 23 53	05 15 00	189.299	-28.752	170.0(3.6)	24.2(0.6)	-210.1(0.3)	12.5	10.9			F
63	3C 120-	04 23 53	05 15 00	189.299	-28.752	43.2(2.3)	30.0(2.6)	-136.5(1.1)	12.5	10.9			F
64	3C 120	04 30 32	05 15 00	190.373	-27.397	28.8(3.8)	27.4(11.2)	-205.9(12.6)	3.1	3.8			H,U
65	S5 0437+78-	04 31 08	78 33 23	133.062	20.571	910.0(17.8)	33.2(1.0)	-117.7(0.3)	24.0	7.2			H,A
66	3C 120+	04 37 10	05 15 01	191.415	-26.032	30.0(2.4)	32.2(23.1)	-183.7(17.8)	3.1	3.8			H,U
67	3C 120+	04 37 10	05 15 01	191.415	-26.032	55.0(1.8)	56.0(4.5)	-129.3(1.7)	3.1	3.8			H,U
68	S5 0437+78	04 38 00	78 33 24	133.285	20.840	1804.0(36.8)	23.8(0.6)	-119.6(0.3)	43.0	7.9			H,A
69	S5 0437+78+	04 44 53	78 33 21	133.501	21.115	2052.0(58.0)	24.8(0.8)	-119.1(0.3)	70.0	7.3			H,A
70	PKS 0454+039-	04 47 17	03 56 17	194.159	-24.646					2.8	1.51	-114	H

Table 3—Continued

#	Object	α (B1950)	δ (B1950)	l (deg)	b (deg)	T_{peak} (mK)	Δv (km s $^{-1}$)	V_{LSR} (km s $^{-1}$)	σ_g (mK)	σ_b (mK)	N_{HI} (10 19)	$\langle V \rangle$ (km s $^{-1}$)	Notes
71	IR 0450–2958+	04 57 25	–29 58 29	231.560	–36.138	12.9(1.4)	27.4(3.5)	242.8(1.6)	1.9	2.4			H
72	PKS 0454–22+	05 00 40	–22 03 54	222.585	–33.193	59.0(2.0)	30.0(1.1)	141.3(0.6)	2.8	2.4			H
73	MS 05217+79–	05 14 52	79 18 38	133.625	22.734	436.0(10.0)	27.8(0.7)	–193.5(0.3)	13.0	3.6			H,A
74	MS 05217+79–	05 14 52	79 18 38	133.625	22.734	379.0(9.2)	35.2(1.3)	–118.2(0.4)	13.0	3.6			H,A
75	MS 05217+79	05 21 44	79 18 40	133.783	23.018	345.0(4.2)	31.0(0.4)	–180.4(0.1)	5.6	3.2			H,A
76	MS 05217+79	05 21 44	79 18 40	133.783	23.018	174.0(3.5)	51.3(2.1)	–114.0(0.7)	5.6	3.2			H,A
77	MS 05217+79+	05 28 37	79 18 39	133.933	23.305	273.0(4.2)	45.2(1.4)	–161.5(0.7)	7.5	3.2			H,A
78	MS 05217+79+	05 28 37	79 18 39	133.933	23.305					3.2	0.45	–115	H,A
79	3C 147–	05 31 51	49 49 44	161.103	9.351					2.9	2.96	–112	H,A
80	3C 147	05 38 43	49 49 46	161.686	10.298	1057.0(31.1)	19.4(0.7)	–121.2(0.3)	33.0	5.5			H,A
81	4C 16.14–	05 41 33	16 35 58	190.410	–6.623	26.1(1.7)	86.4(7.5)	–178.9(3.0)	3.9	6.0	0.48	–171	H,A,U
82	3C 147+	05 45 36	49 49 44	162.250	11.258	576.0(11.2)	20.6(0.7)	–115.2(0.3)	12.0	2.9			H,A
83	4C 16.14	05 48 25	16 35 58	191.260	–5.211					7.9	0.63	–172	H,A,U
84	4C 16.14+	05 55 17	16 35 59	192.095	–3.790					7.7	0.87	–155	H,A,U
85	3C 154+	06 17 36	26 05 31	186.328	5.365					3.6	0.51	–108	H
86	MARK 380–	07 06 37	74 33 27	140.416	27.499	605.0(121.6)	30.5(3.1)	–195.7(0.6)	20.0	3.5	4.87	–187	H,A
87	MARK 380–	07 06 37	74 33 27	140.416	27.499	93.0(12.7)	57.1(30.5)	–128.6(10.3)	20.0	3.5			H,A
88	MARK 380	07 13 29	74 33 27	140.441	27.956	840.0(21.0)	24.2(0.5)	–193.1(0.1)	14.4	5.3			A
89	MARK 380	07 13 29	74 33 27	140.441	27.956	312.0(10.0)	60.9(2.2)	–165.9(1.6)	14.4	5.3			A
90	3C 184–	07 16 23	81 52 43	132.146	28.069	13.1(1.1)	36.2(3.8)	–178.9(1.6)	1.6	2.6			H,A
91	3C 184–	07 16 23	81 52 43	132.146	28.069	17.2(1.4)	27.2(3.5)	–123.7(1.3)	1.6	2.6			H,A,U
92	MARK 380+	07 20 22	74 33 28	140.452	28.414	1956.0(80.0)	17.4(0.7)	–190.0(0.2)	56.0	5.1			A
93	MARK 380+	07 20 22	74 33 28	140.452	28.414	542.0(43.0)	48.7(3.7)	–171.0(2.8)	56.0	5.1			A
94	3C 185–	07 29 10	–01 57 32	219.409	7.989					3.3	0.07	103	H,A
95	3C 184	07 29 23	81 52 42	132.109	28.527					3.1	0.18	–117	H,A
96	PKS 0736+01–	07 29 50	01 44 02	216.181	9.858					3.7	0.54	126	H,A
97	3C 185	07 36 02	–01 57 28	220.226	9.504					3.3	0.25	114	H,A
98	PKS 0736+01	07 36 42	01 44 03	216.989	11.380					3.7	0.45	122	H,A
99	3C 184+	07 42 23	81 52 43	132.040	28.982	18.4(2.3)	20.1(3.0)	–121.1(1.3)	2.5	3.0			H,A
100	3C 185+	07 42 55	–01 57 30	221.054	11.015					3.2	0.23	109	H,A
101	PKS 0736+01+	07 43 35	01 44 01	217.805	12.901					3.7	0.40	125	H,A
102	MARK 1413–	07 45 04	73 19 07	141.792	30.169	130.0(4.0)	34.0(1.4)	–149.9(0.6)	10.9	9.0			F,H
103	MARK 1413–	07 45 04	73 19 07	141.792	30.169	36.5(5.4)	18.1(4.1)	–110.7(1.4)	10.9	9.0			F,H
104	PKS 0743+006+	07 50 13	00 36 54	219.620	13.844					3.9	0.12	104	H
105	MARK 1413	07 58 04	73 19 05	141.670	31.096					15.6	0.25	–113	F

Table 3—Continued

#	Object	α (B1950)	δ (B1950)	l (deg)	b (deg)	T_{peak} (mK)	Δv (km s ⁻¹)	V_{LSR} (km s ⁻¹)	σ_g (mK)	σ_b (mK)	N_{HI} (10 ¹⁹)	$\langle V \rangle$ (km s ⁻¹)	Notes
106	MS 08080+484-	08 01 09	48 40 29	170.635	31.810					3.0	0.06	-105	H
107	3C 196-	08 03 07	48 22 09	171.036	32.100					3.4	0.04	-105	H
108	4CP 62.12-	08 14 30	62 07 17	154.652	33.925	56.0(5.4)	24.9(2.8)	-186.1(1.1)	13.2	14.6			F,H
109	MS 08220+030-	08 15 13	03 09 51	220.352	20.554					2.8	0.21	110	H
110	4CP 62.12	08 21 23	62 07 17	154.556	34.724	82.0(6.0)	38.7(3.2)	-162.3(1.3)	24.0	26.0			F
111	0830+112-	08 23 43	11 15 31	213.506	26.076	252.0(29.0)	30.0(1.9)	106.5(0.9)	27.0	22.0			F
112	0830+112-	08 23 43	11 15 31	213.506	26.076	178.0(29.0)	11.1(1.6)	111.6(0.5)	27.0	22.0			F
113	4CP 62.12+	08 28 15	62 07 17	154.432	35.521	991.0(9.0)	21.3(0.2)	-171.4(0.1)	28.0	24.0			F
114	PKS 0837-12-	08 30 35	-12 03 53	236.198	16.033	62.3(3.8)	32.1(2.8)	123.6(1.0)	5.0	4.9			H,U
115	0830+112	08 30 36	11 15 31	214.309	27.601	42.0(4.0)	13.9(1.9)	109.1(0.7)	11.0	9.6			F
116	DW 0839+18-	08 32 22	18 46 29	206.584	30.964					4.1	0.28	119	H,A
117	US 1329	08 33 34	44 36 31	176.141	36.988					2.5	0.08	-113	H
118	4C 19.31	08 36 15	19 32 28	206.130	32.095					2.7	0.10	126	H
119	PKS 0837-12	08 37 28	-12 03 52	237.172	17.430	200.0(3.6)	32.9(1.3)	110.7(0.6)	9.8	11.6			F
120	TON 951-	08 37 56	34 56 11	188.255	36.578	15.3(1.6)	22.5(3.3)	-105.3(1.3)	1.8	1.6			H
121	DW 0839+18	08 39 14	18 46 28	207.275	32.480					4.1	0.08	97	H,A
122	PKS 0837-12+	08 44 20	-12 03 52	238.172	18.816	82.0(4.2)	28.6(1.7)	126.8(0.7)	5.6	4.3			H,U
123	CSO 199+	08 45 00	35 55 21	187.344	38.209	27.0(2.8)	33.0(3.7)	106.9(1.6)	3.6	2.0			H
124	DW 0839+18+	08 46 06	18 46 26	207.972	33.998					3.8	0.12	127	H,A
125	TON 951+	08 51 12	34 56 11	188.852	39.355	14.8(0.8)	50.6(3.5)	119.5(1.4)	1.4	2.1			H
126	PKS 0859-14-	08 53 02	-14 03 36	241.193	19.384	31.4(1.4)	20.8(1.6)	104.9(0.6)	1.4	3.2			H
127	US 2068+	09 02 52	46 49 00	173.315	42.114	12.7(3.7)	17.9(6.7)	-116.9(2.6)	5.3	3.3			
128	PKS 0859-14+	09 06 47	-14 03 37	243.339	22.044	10.3(1.7)	19.2(3.5)	-696.1(1.6)	1.8	2.8			H
129	NGC 2841 UB3-	09 11 42	51 11 19	167.198	43.088	27.8(1.7)	35.4(2.5)	-113.2(1.0)	3.4	3.4			
130	NGC 2841 UB3	09 18 35	51 11 19	166.944	44.149	100.0(0.0)	620.0(0.0)	630.0(0.0)	0.0	4.1			NGC 2841
131	RO2.37-	09 24 27	-16 55 42	248.675	23.512	150.0(4.2)	49.2(3.4)	104.6(1.7)	6.7	11.1			H,A
132	RO2.37	09 31 20	-16 55 41	249.869	24.742					10.9	0.52	126	H,A
133	PKS 0925-203+	09 32 12	-20 21 43	252.777	22.565	86.7(3.4)	28.1(2.1)	99.3(0.8)	4.2	2.3			H
134	RO2.37+	09 38 12	-16 55 41	251.100	25.953	247.0(4.2)	35.1(1.1)	103.6(0.4)	5.6	9.2			H
135	PG 0946+301-	09 39 54	30 09 21	197.511	48.766					4.9	0.11	-120	H,A
136	PG 0946+301	09 46 46	30 09 19	197.831	50.237					6.6	0.20	-107	A
137	3C 232-	09 48 33	32 38 24	194.005	50.879	33.8(4.0)	40.2(6.1)	-117.3(2.3)	7.6	4.4			
138	MARK 132-	09 51 15	55 09 05	159.490	47.723	173.0(7.4)	24.0(1.2)	-147.9(0.5)	25.2	24.6			F
139	0959+68W1-	09 52 17	68 27 49	142.953	41.437	173.0(0.0)	75.0(0.0)	-120.0(0.0)	0.0	2.0			M81/M82
140	MS 10067+814-	09 53 07	81 45 22	129.830	33.166					2.5	0.14	-130	H,A

Table 3—Continued

#	Object	α (B1950)	δ (B1950)	l (deg)	b (deg)	T_{peak} (mK)	Δv (km s $^{-1}$)	V_{LSR} (km s $^{-1}$)	σ_g (mK)	σ_b (mK)	N_{HI} (10 19)	$\langle V \rangle$ (km s $^{-1}$)	Notes
141	PG 0946+301+	09 53 39	30 09 21	198.133	51.710					6.2	0.55	−108	A
142	TON 28−	09 54 20	29 13 02	199.678	51.783					4.2	0.07	−117	
143	TON 28−	09 54 20	29 13 02	199.678	51.783	16.4(1.4)	13.0(1.3)	117.4(0.6)	1.8	2.5			
144	TON 28−	09 54 20	29 13 02	199.678	51.783	50.0(0.0)	125.0(0.0)	495.0(0.0)	0.0	4.2			UGC 5340
145	PKS 1004−217−	09 57 33	−21 44 45	258.468	25.719					3.4	0.25	145	H
146	MARK 132	09 58 08	55 09 07	158.904	48.624	95.3(7.2)	22.5(2.0)	−147.3(0.8)	23.8	22.4			F
147	0959+68W1	09 59 09	68 27 49	142.464	41.952	210.0(0.0)	125.0(0.0)	−100.0(0.0)	0.0	12.8			M81/M82
148	PKS 0953+415+	10 00 26	41 30 00	179.491	52.939	41.8(7.1)	21.3(4.5)	−97.0(2.7)	12.1	12.2			F
149	4C 41.21−	10 00 48	41 47 24	178.998	52.959	53.9(6.1)	21.1(3.2)	−97.0(1.2)	9.5	7.4			
150	PKS 1009−321−	10 02 49	−32 08 45	266.685	18.527	112.0(10.0)	16.7(1.9)	172.2(0.8)	29.6	30.7			F
151	PKS 1009−321−	10 02 49	−32 08 45	266.685	18.527	795.0(8.0)	28.5(0.3)	212.8(0.1)	29.6	30.7			F
152	PKS 1004−217	10 04 25	−21 44 42	259.800	26.776					2.5	0.25	124	H
153	PKS 1004−217	10 04 25	−21 44 42	259.800	26.776	20.0(2.8)	47.6(9.6)	175.1(4.9)	3.6	2.5			H
154	MARK 132+	10 05 00	55 09 06	158.265	49.512	35.1(3.4)	32.4(3.7)	−131.4(1.6)	9.4	9.5			F,H
155	0959+68W1+	10 06 02	68 27 48	141.949	42.454	36.0(0.0)	60.0(0.0)	−120.0(0.0)	0.0	2.3			M81/M82
156	Q 1013+0124−	10 06 30	01 24 14	239.705	43.230					2.8	0.17	147	H
157	MS 10067+814	10 06 37	81 45 23	129.425	33.511					4.1	0.14	−126	H,A
158	4C 41.21	10 07 26	41 47 24	178.641	54.178	24.9(3.7)	22.5(4.0)	−110.2(1.6)	6.0	5.6			U
159	PKS 1009−321	10 09 42	−32 08 45	267.901	19.417	392.0(9.0)	31.9(0.8)	202.9(0.3)	33.3	30.9			F
160	PKS 1011−282	10 11 12	−28 16 30	265.661	22.691	287.0(2.8)	30.4(0.4)	222.4(0.1)	3.8	3.0			H
161	PKS 1011−282	10 11 12	−28 16 30	265.661	22.691	15.6(3.4)	19.7(5.1)	275.9(2.1)	3.8	3.0			H
162	PKS 1004−217+	10 11 17	−21 44 43	261.171	27.806					12.0	0.43	120	F
163	PKS 1004−217+	10 11 17	−21 44 43	261.171	27.806	40.0(4.0)	41.1(5.7)	157.4(3.1)	12.0	12.0			F
164	B3 1019+397−	10 12 48	39 47 02	181.777	55.520					3.3	0.10	−110	H,A
165	PKS 1020−103−	10 13 12	−10 22 33	252.620	36.603	66.0(3.0)	48.6(3.0)	163.6(1.2)	16.6	15.4			F
166	Q 1013+0124	10 13 22	01 24 12	241.172	44.583					5.0	0.07	142	U
167	4C 41.21+	10 14 04	41 47 25	178.220	55.391	110.0(0.0)	150.0(0.0)	608.0(0.0)	0.0	7.4			NGC 3184
168	Ton 34	10 17 06	27 59 01	202.957	56.507	39.0(2.8)	23.2(1.6)	98.9(0.6)	2.6	3.0			H
169	PKS 1011−282+	10 18 04	−28 16 31	266.975	23.602	765.0(12.0)	23.3(0.4)	122.6(0.1)	14.4	2.7			H
170	PKS 1011−282+	10 18 04	−28 16 31	266.975	23.602	36.9(3.8)	26.5(3.1)	222.1(1.4)	4.9	2.7			H
171	B3 1019+397	10 19 40	39 47 03	181.380	56.821	262.0(3.0)	36.4(0.4)	−102.7(0.1)	4.3	3.2			H,A
172	PKS 1020−103	10 20 04	−10 22 33	254.161	37.764	24.9(3.4)	29.4(4.9)	160.2(2.0)	8.9	8.0			F,H
173	MS 10067+814+	10 20 07	81 45 23	128.993	33.836					3.9	0.20	−137	H,A
174	B3 1019+397+	10 26 33	39 47 02	180.909	58.117	222.5(4.0)	35.0(0.7)	−100.8(0.3)	5.8	3.3			H,A
175	PKS 1020−103+	10 26 56	−10 22 33	255.757	38.898	21.7(2.8)	48.5(10.2)	176.7(3.7)	5.2	2.5			H

Table 3—Continued

#	Object	α (B1950)	δ (B1950)	l (deg)	b (deg)	T_{peak} (mK)	Δv (km s $^{-1}$)	V_{LSR} (km s $^{-1}$)	σ_g (mK)	σ_b (mK)	N_{HI} (10 19)	$\langle V \rangle$ (km s $^{-1}$)	Notes
176	PKS 1034–29–	10 28 03	–29 18 25	269.578	24.021	225.0(8.0)	25.1(1.1)	152.1(0.5)	29.5	31.6			F
177	PKS 1034–29–	10 28 03	–29 18 25	269.578	24.021	190.0(10.0)	16.4(1.0)	228.6(0.4)	29.5	31.6			F
178	PKS 1034–29	10 34 56	–29 18 24	270.951	24.847	163.5(8.0)	26.8(1.7)	126.0(0.7)	30.0	33.0			F
179	IRAS 1047–28–	10 41 03	–28 07 44	271.514	26.558					14.0	0.06	111	F
180	IRAS 1047–28–	10 41 03	–28 07 44	271.514	26.558	48.0(4.0)	24.0(2.3)	132.7(1.0)	12.0	14.0			F
181	PKS 1034–29+	10 41 48	–29 18 26	272.356	25.639	150.0(6.8)	31.5(2.3)	118.2(1.0)	18.6	18.6			F,H
182	PKS 1034–29+	10 41 48	–29 18 26	272.356	25.639	67.8(6.5)	33.3(3.8)	181.5(1.6)	18.6	18.6			F,H
183	4C 61.20–	10 42 30	61 41 19	145.656	49.790	30.5(1.6)	28.7(1.7)	–155.3(0.7)	2.0	2.9			H
184	IRAS 1051–27–	10 44 17	–27 22 52	271.760	27.569					7.5	0.20	111	H,A
185	IRAS 1051–27–	10 44 17	–27 22 52	271.760	27.569	42.0(7.5)	24.5(5.8)	127.6(2.1)	4.5	7.5			H,A
186	IRAS 1051–27–	10 44 17	–27 22 52	271.760	27.569	90.0(3.1)	37.2(2.5)	164.4(1.1)	4.5	7.5			H,A
187	IRAS 1047–28	10 47 55	–28 07 44	272.971	27.338					8.6	0.11	109	F,H
188	IRAS 1047–28	10 47 55	–28 07 44	272.971	27.338	29.3(2.8)	36.8(2.4)	147.6(0.8)	8.0	8.6			F,H
189	IRAS 1051–27	10 51 09	–27 22 53	273.248	28.343	57.4(5.5)	25.5(4.1)	97.9(1.4)	3.9	7.5			H,A
190	IRAS 1051–27	10 51 09	–27 22 53	273.248	28.343	35.4(2.0)	69.8(4.1)	144.7(4.1)	3.9	7.5			H,A
191	PKS 1101–325–	10 54 16	–32 35 01	276.699	24.107	110.0(2.8)	43.9(2.0)	145.2(1.1)	3.9	2.7	1.34	150	H
192	PKS 1101–325–	10 54 16	–32 35 01	276.699	24.107	47.0(2.8)	27.4(2.7)	192.1(1.1)	3.9	2.7			H
193	IRAS 1047–28+	10 54 47	–28 07 43	274.461	28.085					3.6	0.33	111	H
194	4C 61.20+	10 56 15	61 41 18	143.817	50.920	13.6(2.4)	20.1(4.2)	–117.8(1.8)	2.7	2.9			H
195	IRAS 1051–27+	10 58 01	–27 22 52	274.770	29.082	139.0(4.5)	19.7(0.7)	92.2(0.1)	2.6	6.1			H,A
196	IRAS 1051–27+	10 58 01	–27 22 52	274.770	29.082	35.0(1.4)	66.5(6.4)	129.5(3.0)	2.6	6.1			H,A
197	PKS 1101–325	11 01 08	–32 35 03	278.115	24.765	187.0(5.0)	45.7(2.0)	115.7(0.8)	23.0	24.0			F
198	PKS 1101–325+	11 08 04	–32 35 02	279.557	25.390					2.6	0.25	107	H
199	PKS 1101–325+	11 08 04	–32 35 02	279.557	25.390	112.0(1.4)	35.3(1.0)	124.8(0.6)	1.3	2.6			H
200	PKS 1101–325+	11 08 04	–32 35 02	279.557	25.390	14.5(1.1)	22.6(4.7)	175.8(1.6)	1.3	2.6			H
201	MRK 421+	11 08 32	38 28 50	178.747	66.298					3.1	0.71	–117	H
202	1119+120–	11 12 19	12 00 47	242.420	62.625					4.0	0.16	–130	H
203	PKS 1127–14–	11 20 43	–14 32 52	273.230	42.903	25.3(1.4)	52.6(1.0)	128.2(0.4)	2.4	3.0			H
204	1130+106Y–	11 24 03	11 08 59	248.032	64.274	14.0(1.4)	29.4(6.2)	–110.2(2.4)	2.4	3.3			H
205	PKS 1117–248+	11 24 33	–24 51 40	279.807	33.917					2.2	0.03	107	H
206	PKS 1117–248+	11 24 33	–24 51 40	279.807	33.917	28.0(2.8)	22.8(2.5)	145.8(1.1)	3.2	2.2			H
207	3C 263.0–	11 30 31	66 04 29	135.091	49.446	60.6(2.4)	33.6(2.1)	–173.1(0.8)	3.4	3.6			H,A
208	3C 263.0–	11 30 31	66 04 29	135.091	49.446	41.9(2.4)	34.4(3.3)	–125.6(1.3)	3.4	3.6			H,A
209	3C 263.0	11 37 09	66 04 29	134.159	49.743	37.5(1.6)	40.3(4.2)	–171.6(2.3)	2.1	3.7			H,A
210	3C 263.0	11 37 09	66 04 29	134.159	49.743	23.6(5.5)	24.8(8.6)	–137.7(3.3)	2.1	3.7			H,A

Table 3—Continued

#	Object	α (B1950)	δ (B1950)	l (deg)	b (deg)	T_{peak} (mK)	Δv (km s ⁻¹)	V_{LSR} (km s ⁻¹)	σ_g (mK)	σ_b (mK)	N_{HI} (10 ¹⁹)	$\langle V \rangle$ (km s ⁻¹)	Notes
211	3C 263.0	11 37 09	66 04 29	134.159	49.743	18.0(2.7)	26.4(11.6)	-110.1(4.8)	2.1	3.7			H,A
212	3C 263.0+	11 43 47	66 04 27	133.205	50.017	27.2(2.0)	63.1(11.5)	-152.1(6.5)	2.9	3.3			H,A
213	3C 263.0+	11 43 47	66 04 27	133.205	50.017	87.5(7.2)	24.1(1.7)	-117.5(0.4)	2.9	3.3			H,A
214	PG 1148+549	11 48 42	54 54 16	140.614	60.391	37.1(3.7)	19.8(3.5)	-112.6(1.4)	7.7	10.6			F,H
215	4C 63.15-	11 49 12	63 11 10	134.124	52.906	117.0(5.0)	35.9(1.9)	-142.7(0.8)	10.9	4.4			A
216	J 08.06-	11 50 15	-19 42 41	284.624	40.788	19.9(1.1)	23.3(1.6)	115.4(0.7)	1.4	3.5			H,U
217	PG 1148+549+	11 55 35	54 54 13	138.811	60.830					3.6	0.23	-116	
218	4C 63.15	11 56 04	63 11 10	132.921	53.185	281.0(10.0)	21.0(0.8)	-145.1(0.4)	15.5	6.5			A
219	PKS 1207-399-	12 00 07	-39 59 29	292.951	21.655	118.0(5.7)	30.9(2.3)	116.3(0.8)	8.0	5.0			H,A
220	PKS 1207-399-	12 00 07	-39 59 29	292.951	21.655	15.0(2.1)	29.4(10.3)	188.1(4.1)	2.6	3.5			H
221	PKS 1207-399-	12 00 07	-39 59 29	292.951	21.655	26.5(3.5)	19.6(3.3)	215.6(1.7)	2.6	3.5			H
222	B2 1208+32A-	12 01 13	32 13 51	185.116	78.575	35.0(0.0)	300.0(0.0)	725.0(0.0)	0.0	5.5			NGC 4062
223	4C 63.15+	12 02 57	63 11 11	131.692	53.431	751.0(11.0)	20.8(0.4)	-148.1(0.2)	17.6	5.1			A
224	PG 1206+459	12 06 26	45 57 19	144.628	69.620					2.7	0.08	-109	
225	MARK 205-	12 06 33	75 35 17	126.510	41.522	97.7(12.0)	14.6(2.0)	-199.3(0.9)	31.0	28.8			F
226	PKS 1207-399	12 06 59	-39 59 27	294.343	21.904					5.7	0.69	112	
227	PG 1206+459+	12 13 19	45 57 19	141.508	70.144	13.0(0.0)	115.0(0.0)	518.0(0.0)	0.0	2.7			NGC 4242
228	PKS 1207-399+	12 13 52	-39 59 28	295.744	22.115	88.0(7.1)	33.6(5.4)	101.5(3.4)	6.2	5.6			H,A
229	PKS 1216-010	12 16 01	-01 03 14	286.091	60.461	9.3(0.8)	54.8(6.2)	143.3(2.5)	1.6	2.9			H
230	PG 1216+069	12 16 47	06 55 21	281.063	68.143	25.5(0.0)	20.5(0.0)	481.0(0.0)	0.0	5.4			VCC 0381
231	MARK 205	12 19 33	75 35 15	125.447	41.673	840.0(35.0)	7.1(0.3)	-207.5(0.1)	31.0	26.0			F
232	MARK 205	12 19 33	75 35 15	125.447	41.673	299.0(28.0)	18.0(0.9)	-202.2(0.7)	31.0	26.0			F
233	SBS 1234+607-	12 27 14	60 47 01	127.801	56.413	216.0(3.4)	38.4(0.9)	-125.1(0.3)	7.0	5.5			A
234	MARK 205+	12 32 33	75 35 18	124.371	41.768	82.1(1.4)	4.2(0.8)	-206.5(0.4)	14.6	17.7			F,H
235	SBS 1234+607	12 34 06	60 47 00	126.296	56.521	302.0(3.2)	37.0(0.6)	-125.8(0.2)	6.6	5.2			A
236	Q 1230+0947+	12 37 46	09 47 57	293.910	72.201	15.9(2.1)	44.1(6.9)	230.6(2.9)	5.0	5.1			
237	SBS 1234+607+	12 40 58	60 47 01	124.779	56.589	504.0(9.6)	21.4(0.4)	-144.3(0.3)	8.1	5.3			A
238	SBS 1234+607+	12 40 58	60 47 01	124.779	56.589	215.0(4.6)	30.8(2.1)	-116.2(0.8)	8.1	5.3			A
239	PG 1259+593-	12 52 30	59 18 16	122.156	58.090	537.0(24.0)	18.7(1.0)	-117.0(0.4)	36.0	6.3			
240	PG 1259+593	12 59 08	59 18 15	120.556	58.048	1360.0(13.0)	22.1(0.2)	-127.7(0.1)	41.0	21.7			F
241	PG 1259+593+	13 05 46	59 18 16	118.965	57.964	1040.0(12.0)	20.3(0.3)	-122.9(0.1)	18.2	5.6			
242	PG 1338+416	13 38 52	41 38 19	90.584	72.484					4.5	0.15	-123	U
243	1351+640-	13 44 55	64 00 29	113.030	52.299	409.0(8.5)	34.0(1.1)	-158.7(0.7)	6.9	6.7			H,A
244	1351+640-	13 44 55	64 00 29	113.030	52.299	276.0(7.1)	35.3(2.3)	-121.9(1.0)	6.9	6.7			H
245	PG 1338+416+	13 45 44	41 38 19	87.467	71.631					4.5	0.27	-131	U

Table 3—Continued

#	Object	α (B1950)	δ (B1950)	l (deg)	b (deg)	T_{peak} (mK)	Δv (km s $^{-1}$)	V_{LSR} (km s $^{-1}$)	σ_g (mK)	σ_b (mK)	N_{HI} (10 19)	$\langle V \rangle$ (km s $^{-1}$)	Notes
246	1351+640	13 51 47	64 00 28	111.890	52.020	755.0(22.6)	27.8(0.6)	-156.0(0.4)	8.3	6.7			H,A
247	1351+640	13 51 47	64 00 28	111.890	52.020	186.0(7.1)	39.8(5.7)	-123.0(2.3)	8.3	6.7			H,A
248	1351+640+	13 58 40	64 00 28	110.778	51.711	354.0(9.0)	34.0(1.3)	-157.3(0.5)	18.2	11.1			A
249	1351+640+	13 58 40	64 00 28	110.778	51.711	277.0(11.0)	22.8(1.4)	-116.3(0.5)	18.2	11.1			A
250	1411+422-	14 04 58	44 14 25	85.842	67.292	17.4(2.6)	29.7(5.4)	-99.5(2.2)	4.9	4.8			
251	M16.11-	14 07 12	-25 10 19	324.468	34.155					2.9	0.05	-104	H
252	M16.11	14 14 04	-25 10 18	326.206	33.576					3.2	0.12	-112	H
253	M16.11+	14 20 57	-25 10 19	327.910	32.954	106.0(2.8)	19.0(0.4)	-153.7(0.1)	2.6	2.9			H
254	PKS 1421-38	14 21 12	-38 13 11	322.227	20.923	18.4(3.5)	29.9(7.2)	119.0(2.8)	4.6	3.5			H
255	PKS 1421-38	14 21 12	-38 13 11	322.227	20.923	215.0(4.0)	22.3(0.4)	169.2(0.1)	4.6	3.5			H
256	PKS 1435-218-	14 28 26	-21 51 55	331.514	35.184	40.0(2.4)	33.9(2.4)	-91.8(1.0)	3.5	5.4			H
257	S4 1435+63-	14 28 45	63 49 38	106.117	50.184	66.7(3.2)	69.3(5.2)	-138.0(2.0)	8.9	7.0			A
258	B2 1425+26+	14 32 14	26 45 41	37.390	67.053					6.2	0.12	-123	U
259	PKS 1435-218	14 35 18	-21 51 55	333.228	34.436	12.9(2.3)	27.7(5.5)	-97.1(2.4)	2.9	4.2			H
260	S4 1435+63	14 35 37	63 49 38	105.175	49.729	96.5(4.9)	49.6(3.6)	-120.0(1.4)	11.6	7.8			A
261	S4 1435+63+	14 42 29	63 49 36	104.270	49.251	228.0(5.6)	44.2(1.6)	-117.2(0.6)	12.6	7.5			A
262	3C 309-	14 45 56	71 52 11	111.061	42.721	126.0(3.4)	38.7(1.3)	-135.1(0.5)	7.3	7.3			A
263	PKS 1451-375	14 51 18	-37 35 21	328.227	18.964					3.6	0.14	-108	H
264	PKS 1451-375+	14 58 10	-37 35 22	329.480	18.299	55.0(2.8)	34.6(1.8)	109.6(0.8)	3.8	4.8			H
265	PKS 1451-375+	14 58 10	-37 35 22	329.480	18.299					4.8	0.09	-121	H
266	3C 309	14 58 56	71 52 12	109.983	42.097	171.0(3.2)	35.2(0.8)	-141.8(0.3)	6.5	6.6			A
267	3C 309	14 58 56	71 52 12	109.983	42.097	100.0(0.0)	170.0(0.0)	457.0(0.0)	0.0	6.6			NGC 5832
268	3C 309+	15 11 57	71 52 09	108.973	41.423	66.6(3.6)	35.4(2.3)	-141.6(1.0)	7.6	6.2			A
269	PKS 1538+477-	15 31 08	47 45 17	77.009	52.591	40.0(1.7)	28.2(1.4)	-167.1(0.6)	2.2	2.5			H
270	PG 1634+706-	16 27 59	70 37 36	103.127	37.166	76.5(3.0)	31.9(2.0)	-161.7(1.0)	3.7	3.2	0.98	-140	H,A
271	PG 1634+706	16 34 52	70 37 39	102.843	36.644	135.0(3.3)	26.0(0.8)	-158.6(0.3)	3.1	3.6	1.23	-151	H,A
272	PG 1634+706+	16 41 44	70 37 35	102.578	36.115	97.5(4.9)	30.4(1.4)	-160.0(0.4)	2.8	2.7	1.04	-150	H,A
273	3C 345+	16 48 10	39 54 12	63.589	39.635					3.7	0.24	-121	
274	1641.7+399+	16 48 37	39 58 47	63.698	39.555	41.0(5.1)	26.7(3.9)	-118.8(1.2)	6.4	4.1			
275	PG 1700+518-	16 53 21	51 53 39	79.097	38.830	19.7(1.6)	37.0(4.7)	-169.2(1.8)	2.2	2.5	0.49	-134	H,A
276	PG 1700+518-	16 53 21	51 53 39	79.097	38.830	40.1(2.0)	23.1(1.8)	-130.0(0.7)	2.2	2.5			H,A
277	3C 351-	16 57 25	60 48 30	90.245	37.181	105.0(1.5)	62.5(1.4)	-154.7(0.5)	4.1	5.6			A
278	3C 351-	16 57 25	60 48 30	90.245	37.181	58.0(2.3)	30.4(2.1)	-90.6(0.7)	4.1	5.6			A
279	PG 1700+518	17 00 13	51 53 38	79.020	37.771	15.0(2.3)	43.6(15.7)	-158.2(8.2)	3.3	2.5	0.20	-106	H,A
280	PG 1700+518	17 00 13	51 53 38	79.020	37.771	17.2(7.2)	16.0(6.4)	-132.8(1.8)	3.3	2.5			H,A

Table 3—Continued

#	Object	α (B1950)	δ (B1950)	l (deg)	b (deg)	T_{peak} (mK)	Δv (km s ⁻¹)	V_{LSR} (km s ⁻¹)	σ_g (mK)	σ_b (mK)	N_{HI} (10 ¹⁹)	$\langle V \rangle$ (km s ⁻¹)	Notes
281	3C 351	17 04 03	60 48 31	90.084	36.382	50.0(3.0)	43.2(4.1)	-182.2(1.6)	6.5	5.8			A
282	3C 351	17 04 03	60 48 31	90.084	36.382	89.0(3.0)	34.8(2.8)	-128.2(0.9)	6.5	5.8			A
283	3C 351	17 04 03	60 48 31	90.084	36.382	70.0(4.0)	30.0(2.8)	-83.0(1.0)	6.5	5.8			A
284	PG 1700+518+	17 07 05	51 53 38	78.977	36.712	24.7(1.1)	34.3(2.3)	-181.3(0.8)	1.7	2.8	0.38	-143	H,A
285	PG 1700+518+	17 07 05	51 53 38	78.977	36.712	27.0(1.3)	28.2(2.0)	-132.9(0.8)	1.7	2.8			H
286	PG 1715+535-	17 08 38	53 31 26	80.997	36.431	154.0(14.1)	31.7(5.2)	-100.0(2.3)	20.0	2.7			H
287	3C 351+	17 10 42	60 48 32	89.951	35.580	116.0(12.0)	34.0(1.9)	-177.6(1.4)	4.6	5.1	1.14	-168	A
288	3C 351+	17 10 42	60 48 32	89.951	35.580	28.6(3.5)	48.7(22.6)	-139.5(8.3)	4.6	5.1			A
289	PG 1718+481-	17 11 25	48 07 12	74.301	35.975	54.3(1.6)	39.3(1.7)	-154.6(0.7)	2.3	3.1	0.53	-157	H,A
290	B2 1721+34-	17 14 40	34 20 42	57.751	33.568	138.0(5.0)	31.1(1.3)	-142.3(0.5)	19.0	18.0			F
291	PG 1715+535	17 15 31	53 31 25	80.966	35.410	77.0(22.6)	68.3(32.8)	-130.6(23.2)	17.0	2.4	1.79	-121	H
292	PG 1718+481	17 18 17	48 07 11	74.375	34.829	91.6(4.5)	35.4(2.1)	-132.2(0.8)	6.5	3.0	0.75	-145	H,A
293	V 396 Her	17 20 37	24 39 06	47.194	29.699	10.7(1.4)	52.5(9.3)	-147.2(3.7)	2.2	2.6			H
294	V 396 Her	17 20 37	24 39 06	47.194	29.699					2.6	0.01	-108	H
295	PG 1715+535+	17 22 23	53 31 27	80.967	34.390	671.0(10.0)	35.7(1.0)	-119.2(0.6)	27.0	24.0	4.34	-121	F
296	4C50.43-	17 22 57	50 09 45	76.904	34.190	42.5(4.0)	30.0(4.4)	-165.8(1.7)	10.4	10.9			F,H
297	4C50.43-	17 22 57	50 09 45	76.904	34.190	30.7(6.5)	25.6(8.1)	-125.9(3.0)	10.4	10.9			F,H
298	4C50.43-	17 22 57	50 09 45	76.904	34.190					10.9	0.13	-110	F,H
299	PG 1718+481+	17 25 10	48 07 11	74.478	33.686	29.1(2.3)	25.9(2.3)	-193.5(1.0)	2.8	3.6	0.43	-158	H,A
300	PG 1718+481+	17 25 10	48 07 11	74.478	33.686	36.8(2.0)	34.2(3.5)	-124.0(1.6)	2.8	3.6			H,A
301	PKS 1725+044	17 25 56	04 29 28	27.294	20.478					3.3	0.10	133	H
302	V 396 Her+	17 27 30	24 39 06	47.773	28.222	188.0(2.8)	30.5(0.6)	-153.5(0.3)	3.5	2.9			H
303	V 396 Her+	17 27 30	24 39 06	47.773	28.222	34.0(2.8)	30.7(3.1)	-105.9(1.3)	3.5	2.9			H
304	4C50.43	17 29 49	50 09 45	76.990	33.092	129.0(7.0)	27.0(1.7)	-127.8(0.7)	17.0	18.0	0.96	-127	F
305	PKS 1725+044+	17 32 48	04 29 30	28.135	18.959	91.3(5.4)	27.9(2.0)	-109.7(1.1)	3.5	3.1			H
306	PKS 1725+044+	17 32 48	04 29 30	28.135	18.959					3.1	0.04	91	H,U
307	4C50.43+	17 36 41	50 09 43	77.104	31.996	251.0(5.0)	32.3(0.8)	-98.9(0.3)	18.0	15.0			F
308	MC 1745+163-	17 39 03	16 20 13	40.286	22.672	70.0(6.0)	15.7(1.6)	-186.5(0.7)	18.0	16.0			F
309	MC 1745+163-	17 39 03	16 20 13	40.286	22.672	68.0(6.0)	19.3(2.1)	-140.0(0.8)	18.0	16.0			F
310	MC 1745+163-	17 39 03	16 20 13	40.286	22.672	300.0(5.0)	27.0(0.6)	-102.0(0.2)	18.0	16.0			F
311	IRAS 1750+50-	17 43 12	50 46 23	77.944	31.029	98.0(8.0)	27.1(4.6)	-147.2(2.2)	28.8	28.0			F
312	IRAS 1750+50-	17 43 12	50 46 23	77.944	31.029	363.0(55.0)	26.8(2.7)	-114.0(0.8)	28.8	28.0			F
313	IRAS 1750+50-	17 43 12	50 46 23	77.944	31.029					28.0	0.44	-112	F
314	MC3 1750+17-	17 43 41	17 34 58	41.997	22.146	32.0(1.8)	27.9(2.3)	-115.8(0.8)	2.3	3.5			H,A
315	MC3 1750+17-	17 43 41	17 34 58	41.997	22.146					3.5	0.06	88	H,A,U

Table 3—Continued

#	Object	α (B1950)	δ (B1950)	l (deg)	b (deg)	T_{peak} (mK)	Δv (km s $^{-1}$)	V_{LSR} (km s $^{-1}$)	σ_g (mK)	σ_b (mK)	N_{HI} (10^{19})	$\langle V \rangle$ (km s $^{-1}$)	Notes
316	MC 1745+163	17 45 55	16 20 13	40.996	21.160					17.0	0.38	-117	F
317	OT 081	17 49 10	09 39 45	34.920	17.646	156.0(12.7)	23.8(2.1)	-139.6(1.4)	7.1	3.1			H
318	OT 081	17 49 10	09 39 45	34.920	17.646	239.0(7.1)	29.1(2.0)	-112.8(1.1)	7.1	3.1			H
319	PKS 1756+237-	17 50 03	23 43 57	48.778	23.076	55.7(7.5)	50.0(12.6)	-122.5(4.8)	24.4	17.2			F,H
320	IRAS 1750+50	17 50 05	50 46 21	78.099	29.950	35.0(9.0)	24.6(5.4)	-157.1(1.2)	10.0	11.6			F
321	IRAS 1750+50	17 50 05	50 46 21	78.099	29.950					11.6	0.36	-129	F
322	MC3 1750+17	17 50 33	17 34 59	42.691	20.641	114.0(2.0)	40.5(1.6)	-110.7(0.7)	3.0	3.0			H,A
323	MC3 1750+17	17 50 33	17 34 59	42.691	20.641					3.0	0.08	97	H,A,U
324	MC 1745+163+	17 52 48	16 20 13	41.703	19.652	79.0(10.0)	16.3(2.3)	-136.7(0.7)	17.0	18.0			F
325	MC 1745+163+	17 52 48	16 20 13	41.703	19.652	165.0(6.0)	47.5(1.8)	-118.3(1.2)	17.0	18.0			F
326	OU 401-	17 53 11	44 04 18	70.642	28.289					22.6	0.19	-127	F
327	OT 081+	17 56 03	09 39 44	35.692	16.120	19.7(1.4)	37.8(3.8)	-136.1(1.4)	2.2	3.2			H
328	PKS 1756+237	17 56 56	23 43 55	49.395	21.610	62.6(5.1)	31.1(3.8)	-123.5(1.7)	12.1	15.5			F,H
329	IRAS 1750+50+	17 56 57	50 46 21	78.280	28.876	90.0(2.8)	34.8(1.6)	-139.8(0.6)	3.8	2.6	0.67	-137	H
330	MC3 1750+17+	17 57 26	17 34 59	43.386	19.139	46.0(1.7)	55.8(4.0)	-116.0(1.6)	3.1	3.1			H,A
331	MC3 1750+17+	17 57 26	17 34 59	43.386	19.139					3.1	0.09	88	H,A,U
332	OU 401	18 00 03	44 04 20	70.943	27.084					25.2	0.22	-112	F
333	PKS 1756+237+	18 03 48	23 43 58	50.019	20.150	330.0(7.0)	35.5(0.9)	-111.0(0.4)	27.4	24.2			F
334	OU 401+	18 06 56	44 04 19	71.265	25.883	74.0(10.0)	40.3(5.3)	-118.5(2.6)	20.9	22.2	0.59	-121	F
335	H 18217+643-	18 14 49	64 19 02	93.918	28.133					4.2	0.40	-103	H
336	3C 380.0-	18 21 21	48 42 41	76.908	24.601	900.0(25.5)	32.1(1.7)	-117.3(0.7)	33.9	6.6	5.43	-120	H,A
337	3C 380.0-	18 21 21	48 42 41	76.908	24.601					6.6	0.37	129	H,A,U
338	H 18217+643	18 21 42	64 19 03	94.003	27.417					20.0	0.48	-114	F
339	3C 380.0	18 28 13	48 42 39	77.225	23.505	1532.0(36.8)	34.3(1.0)	-110.8(0.4)	52.0	7.1	8.10	-116	H,A
340	3C 380.0	18 28 13	48 42 39	77.225	23.505					7.1	0.44	129	H,A,U
341	H 18217+643+	18 28 20	64 19 03	94.108	26.704					4.1	0.53	-114	H
342	3C 380.0+	18 35 06	48 42 42	77.564	22.415	1602.0(26.9)	32.8(0.7)	-105.8(0.3)	37.0	6.2	8.00	-119	H,A
343	3C 380.0+	18 35 06	48 42 42	77.564	22.415	60.3(3.5)	27.0(1.8)	-209.5(0.8)	4.5	6.2			H,A
344	3C 380.0+	18 35 06	48 42 42	77.564	22.415					6.2	0.43	126	H,A,U
345	3C 395-	18 54 10	31 55 14	62.404	13.082	1157.0(9.0)	32.9(0.6)	-108.6(0.3)	33.0	26.0			F
346	IRAS 1910+84-	18 57 24	84 36 54	116.954	27.072					2.4	0.28	-114	H,A
347	3C 395	19 01 02	31 55 13	63.028	11.757	200.0(6.4)	43.2(3.4)	-127.5(1.7)	26.7	29.5	2.32	-120	F
348	3C 395+	19 07 54	31 55 14	63.668	10.441	302.0(7.0)	48.8(2.3)	-122.6(0.9)	35.0	27.0	2.54	-126	F
349	IRAS 1910+84	19 10 24	84 36 53	116.992	26.769					3.3	0.47	-118	H,A
350	4C 73.18-	19 15 49	73 51 47	105.354	24.409	205.8(3.1)	37.5(1.3)	-111.3(0.6)	4.6	5.6			H,A

Table 3—Continued

#	Object	α (B1950)	δ (B1950)	l (deg)	b (deg)	T_{peak} (mK)	Δv (km s $^{-1}$)	V_{LSR} (km s $^{-1}$)	σ_g (mK)	σ_b (mK)	N_{HI} (10 19)	$\langle V \rangle$ (km s $^{-1}$)	Notes
351	4C 50.47−	19 17 56	50 46 52	82.114	16.609	38.6(7.6)	67.1(23.2)	−190.0(7.1)	14.1	4.6	4.31	−128	H,A
352	4C 50.47−	19 17 56	50 46 52	82.114	16.609	602.0(10.5)	32.1(1.4)	−115.8(0.6)	14.1	4.6			H,A
353	IRAS 1910+84+	19 23 24	84 36 54	117.050	26.469	41.9(4.0)	24.0(8.1)	−132.7(6.6)	3.6	3.5	0.46	−121	H,A
354	4C 50.47	19 24 49	50 46 54	82.571	15.615	548.0(32.5)	30.5(1.4)	−114.5(0.4)	12.8	4.9	3.54	−124	H,A
355	4C 73.18	19 28 49	73 51 47	105.626	23.541	336.0(4.2)	38.6(0.7)	−121.6(0.3)	6.3	6.1			H,A
356	4C 50.47+	19 31 41	50 46 52	83.046	14.631	549.0(15.3)	35.4(1.7)	−116.0(0.7)	21.4	5.2	3.80	−128	H,A
357	4C 73.18+	19 41 49	73 51 47	105.946	22.687	360.5(7.1)	38.8(1.0)	−125.9(0.4)	10.5	5.8			H,A
358	Tex 1951+498−	19 44 20	49 50 25	83.119	12.405	1446.0(58.0)	23.1(1.1)	−119.4(0.4)	68.0	3.0			H
359	Tex 1951+498	19 51 12	49 50 24	83.662	11.433	1185.0(9.0)	30.3(0.4)	−118.4(0.2)	33.0	24.0			F
360	Tex 1951+498+	19 58 04	49 50 24	84.223	10.472	1147.0(18.4)	36.4(0.8)	−115.5(0.3)	25.6	3.0			H
361	MS 20078−36+	20 14 46	−36 22 03	5.451	−32.289	41.2(2.0)	42.0(2.4)	−114.4(1.0)	3.2	3.4			H
362	M509+U430	20 43 41	−10 24 05	36.770	−30.134	516.0(11.7)	27.1(1.3)	97.0(0.7)	19.7	8.8			A
363	MS 20532−50	20 53 16	−05 03 11	43.513	−29.793	185.0(4.0)	48.2(1.3)	−222.4(0.5)	20.6	18.2			F
364	MS 20532−50+	21 00 08	−05 03 10	44.474	−31.289	49.5(3.4)	21.0(1.7)	−197.5(0.7)	7.5	10.0			F,H
365	Tex 2116+203−	21 09 25	20 21 23	68.984	−18.576					3.2	0.10	−138	H
366	PKS 2128−12−	21 22 14	−12 20 18	39.621	−39.493	71.8(4.3)	7.7(0.5)	−222.9(0.2)	8.3	9.3			F
367	RXJ 2139+02−	21 30 20	02 32 28	56.865	−33.617	27.0(2.3)	28.3(2.8)	−285.7(1.1)	3.0	3.2			H
368	PKS 2134+004	21 34 05	00 28 26	55.473	−35.577	41.6(4.8)	19.2(2.5)	114.1(1.1)	10.5	13.3			F,H
369	RXJ 21397+02	21 37 12	02 32 28	58.087	−35.006	12.0(2.0)	23.4(4.4)	−223.1(1.8)	2.4	2.6			H
370	PKS 2134+004+	21 40 57	00 28 25	56.702	−36.981					2.8	0.19	121	H
371	B2 2201+31A−	21 54 09	31 31 08	84.766	−17.847					2.8	0.05	−108	H
372	PKS 2155−304+	22 02 36	−30 27 52	17.994	−53.718	17.1(1.6)	39.1(4.3)	−115.1(1.8)	3.5	4.2			
373	PKS 2223+21−	22 16 22	21 02 51	81.711	−29.095	48.7(3.4)	34.4(2.8)	−405.2(1.2)	7.0	7.5			A
374	MS 22241+20−	22 17 15	20 56 29	81.817	−29.306	67.7(2.2)	29.1(1.1)	−408.8(0.5)	4.1	4.5			
375	PKS 2223+21	22 23 15	21 02 53	83.160	−30.087	14.6(4.2)	47.1(11.7)	−405.8(8.6)	2.1	3.5			H,A
376	MS 22241+20	22 24 07	20 56 29	83.273	−30.296	10.5(1.0)	60.5(6.5)	−416.1(2.8)	1.9	2.1			H
377	PKS 2223+21+	22 30 07	21 02 51	84.649	−31.049	7.1(1.1)	41.3(10.6)	−450.4(4.1)	1.8	3.0			H,A
378	PKS 2223+21+	22 30 07	21 02 51	84.649	−31.049	6.9(1.4)	27.4(8.1)	−402.1(3.4)	1.8	3.0			H,A
379	PKS 2243−123−	22 36 47	−12 22 40	52.290	−55.638					3.2	0.09	105	H
380	PKS 2251+11−	22 44 48	11 20 40	80.978	−40.937	16.0(1.1)	49.6(4.5)	−337.9(1.8)	2.0	2.6			H,A
381	3C 454.3−	22 44 51	15 52 56	84.445	−37.281	20.1(4.4)	15.8(4.5)	−428.2(1.8)	4.0	6.1			H,A
382	3C 454.3−	22 44 51	15 52 56	84.445	−37.281	20.5(2.8)	34.9(7.8)	−395.9(3.0)	4.0	6.1			H,A
383	PKS 2254+074−	22 47 54	07 27 12	78.529	−44.471	23.2(2.8)	50.9(6.9)	−328.2(3.0)	4.8	4.4			H,A
384	PKS2247+14	22 47 56	14 03 58	83.889	−39.196	100.0(2.4)	46.1(1.3)	−379.4(0.6)	4.0	3.2			H
385	PKS 2251+11	22 51 40	11 20 40	82.783	−41.940	76.8(3.1)	35.4(1.7)	−362.7(0.7)	4.5	2.4			H,A

Table 3—Continued

#	Object	α (B1950)	δ (B1950)	l (deg)	b (deg)	T_{peak} (mK)	Δv (km s ⁻¹)	V_{LSR} (km s ⁻¹)	σ_g (mK)	σ_b (mK)	N_{HI} (10 ¹⁹)	$\langle V \rangle$ (km s ⁻¹)	Notes
386	PKS 2254+074	22 54 46	07 27 11	80.425	-45.521	91.1(4.4)	47.0(2.5)	-336.0(1.1)	7.3	4.8			H,A
387	PKS 2254+074	22 54 46	07 27 11	80.425	-45.521	9.7(3.1)	34.1(13.3)	-269.2(5.5)	4.4	2.2			H
388	PKS 2247+14+	22 54 49	14 03 58	85.673	-40.140	30.2(1.4)	46.2(3.3)	-376.1(1.4)	3.1	3.0			H
389	3C 454.3+	22 58 08	15 52 56	87.826	-39.050	12.7(1.7)	66.7(10.6)	-377.9(4.5)	3.5	3.2			H
390	3C 454.3+	22 58 08	15 52 56	87.826	-39.050						0.06	131	H
391	PKS 2251+11+	22 58 34	11 20 41	84.653	-42.905	29.8(2.3)	50.9(4.4)	-349.7(1.8)	3.9	2.7			H
392	PKS 2254+074+	23 01 38	07 27 11	82.398	-46.534	15.5(2.5)	32.1(5.9)	-338.2(2.5)	3.5	3.9			H,A
393	4C 09.72-	23 01 54	09 51 59	84.447	-44.591	19.1(2.4)	23.9(3.5)	-105.1(1.4)	2.9	3.2			H
394	4C 09.72-	23 01 54	09 51 59	84.447	-44.591	10.9(2.0)	18.8(4.0)	-440.5(1.7)	2.1	3.0			H
395	PG 2302+029	23 02 12	02 55 35	78.455	-50.230	46.5(1.6)	36.1(1.4)	-324.3(0.6)	2.2	2.7			H
396	PKS 2255-282+	23 02 15	-28 14 26	24.680	-66.429	11.9(1.7)	43.9(7.8)	-155.0(3.3)	2.9	3.6			H
397	PKS 2310-322-	23 03 35	-32 14 06	14.623	-66.693	10.7(1.7)	32.2(6.1)	-159.9(1.8)	2.4	2.6			H
398	4C 09.72	23 08 46	09 51 59	86.450	-45.521	17.0(2.0)	28.5(3.8)	-351.0(1.7)	2.6	3.3			H
399	PG 2302+029+	23 09 04	02 55 34	80.600	-51.280	74.5(1.4)	34.3(1.0)	-321.0(0.4)	2.1	2.7			H
400	PG 2302+029+	23 09 04	02 55 34	80.600	-51.280	21.5(1.3)	50.5(4.4)	-262.8(1.7)	2.1	2.7			H
401	PKS 2310-322+	23 17 20	-32 14 08	13.750	-69.580	17.4(2.1)	37.0(5.4)	-109.3(2.3)	3.3	2.9			H
402	3C 463-	23 18 36	26 59 24	99.339	-31.434					2.4	0.05	-114	H,U
403	B3 2327+407-	23 20 50	40 47 52	105.537	-18.801	36.0(0.0)	260.0(0.0)	400.0(0.0)	0.0	2.9			NGC 7640
404	B3 2327+407	23 27 43	40 47 53	106.831	-19.242	150.0(0.0)	115.0(0.0)	420.0(0.0)	0.0	2.7			UGC 12632
405	3C 463+	23 32 20	26 59 23	102.688	-32.577	26.9(2.4)	21.8(2.3)	-438.1(1.0)	5.5	5.6			F,H
406	3C 463+	23 32 20	26 59 23	102.688	-32.577					5.6	0.17	-136	F,H,U
407	PKS 2340-036-	23 33 30	-03 39 05	82.502	-60.190	116.0(2.4)	49.6(1.7)	-266.2(0.7)	4.1	5.0			H,A
408	PKS 2340-036-	23 33 30	-03 39 05	82.502	-60.190	23.6(2.8)	35.8(6.6)	-210.8(3.0)	4.1	5.0			H,A
409	B3 2327+407+	23 34 35	40 47 52	108.141	-19.651	57.0(1.4)	28.0(0.8)	-131.9(0.3)	1.9	2.6			H
410	PKS 2344+09-	23 37 11	09 14 07	95.100	-49.445	107.0(2.4)	33.3(1.6)	-346.0(0.8)	3.0	3.3			H
411	PKS 2344+09-	23 37 11	09 14 07	95.100	-49.445	81.7(2.5)	32.1(1.8)	-309.2(1.0)	3.0	3.3			H
412	PKS 2340-036	23 40 22	-03 39 04	85.401	-61.151	39.0(2.7)	41.3(4.7)	-300.9(2.3)	3.7	5.6			H,A
413	PKS 2340-036	23 40 22	-03 39 04	85.401	-61.151	40.0(2.1)	51.4(5.8)	-246.5(2.7)	3.7	5.6			H,A
414	PKS 2349-01-	23 42 30	-01 25 53	88.659	-59.534	108.3(3.3)	29.2(1.0)	-296.2(0.4)	4.4	3.2			H
415	PKS 2344+09	23 44 04	09 14 07	97.503	-50.131	36.6(2.3)	51.6(5.1)	-374.6(2.0)	3.8	3.3			H
416	PKS 2344+09	23 44 04	09 14 07	97.503	-50.131	19.1(4.1)	17.8(4.8)	-332.4(1.8)	3.8	3.3			H
417	PKS 2340-036+	23 47 15	-03 39 05	88.472	-62.049	21.1(3.1)	40.4(10.2)	-284.8(5.4)	4.0	4.3			H,A
418	PKS 2340-036+	23 47 15	-03 39 05	88.472	-62.049	22.9(2.5)	46.2(11.0)	-235.6(5.5)	4.0	4.3			H,A
419	4C 49.48-	23 48 45	49 05 03	112.965	-12.341	18.4(2.0)	22.1(2.7)	-357.5(1.1)	2.3	3.8			H,A
420	4C 49.48-	23 48 45	49 05 03	112.965	-12.341	228.0(3.4)	23.3(0.4)	-180.4(0.1)	4.1	3.8			H,A

Table 3—Continued

#	Object	α (B1950)	δ (B1950)	l (deg)	b (deg)	T_{peak} (mK)	Δv (km s ⁻¹)	V_{LSR} (km s ⁻¹)	σ_g (mK)	σ_b (mK)	N_{HI} (10 ¹⁹)	$\langle V \rangle$ (km s ⁻¹)	Notes
421	4C 49.48–	23 48 45	49 05 03	112.965	–12.341					3.8	0.22	–120	H,A,U
422	PKS 2349–01	23 49 22	–01 25 52	91.665	–60.361	15.6(2.0)	31.9(4.8)	–302.2(2.0)	2.8	3.5			H
423	UM 186	23 50 48	–01 32 08	92.211	–60.618	22.7(2.4)	35.0(4.4)	–312.5(1.8)	3.6	3.0			H
424	PKS 2352–342	23 52 50	–34 14 37	359.941	–76.156	25.0(1.9)	24.5(2.3)	116.0(1.0)	3.0	3.1			
425	PKS 2352–342	23 52 50	–34 14 37	359.941	–76.156	17.3(1.2)	60.6(6.1)	172.3(2.3)	3.0	3.1			
426	4C 49.48	23 55 37	49 05 03	114.089	–12.592	180.0(4.0)	25.6(0.7)	–186.0(0.3)	2.8	3.2			H,A
427	UM 18–	23 55 54	05 07 30	99.477	–55.038	12.1(2.8)	35.5(8.1)	–343.8(4.6)	2.8	3.5			
428	UM 18–	23 55 54	05 07 30	99.477	–55.038	14.9(1.3)	52.3(10.8)	–299.5(5.8)	2.8	3.5			
429	PKS 0005–239–	23 58 35	–23 55 58	47.163	–78.129	192.0(9.0)	42.6(2.5)	–84.1(1.0)	42.0	42.0			F
430	PKS 2352–342+	23 59 43	–34 14 37	357.052	–77.414	24.4(1.4)	57.2(3.7)	118.5(1.6)	3.6	3.1			

Note. — Units of right ascension are hours, minutes, and seconds, and units of declination are degrees, arcminutes, and arcseconds. The quantities σ_b and σ_g are the rms noise of the data with respect to the polynomial baseline and the Gaussian, respectively. N_{HI} and $\langle V \rangle$ refer to emission in line wings (§3.1.1). The Notes indicate: “A” Alternate reference position used; “F” frequency-switched observations; “H” Hanning smoothed; “U” uncertain.

Table 4. High Velocity Gaussian Components

	ℓ	b	Name	α (B1950)	δ (B1950)	V_{pk}	N_{HI}	Complex
	(deg)	(deg)				(km s ⁻¹)	(cm ⁻²)	
(1)	(2)	(3)	(4)	(5)	(6)	(7)	(8)	(9)
1	5.451	-32.289	MS 20078-36+	20 14 46	-36 22 03	-114.4	3.36e+18	GCN?
2	13.750	-69.580	PKS 2310-322+	23 17 20	-32 14 08	-109.3	1.25e+18	GCN?
3	14.623	-66.693	PKS 2310-322-	23 03 35	-32 14 06	-159.9	6.69e+17	GCN?
4	17.994	-53.718	PKS 2155-304+	22 02 36	-30 27 52	-115.1	1.30e+18	GCN?
5	24.680	-66.429	PKS 2255-282+	23 02 15	-28 14 26	-155.0	1.01e+18	GCN?
6	28.135	18.959	PKS 1725+044+	17 32 48	04 29 30	-109.7	4.95e+18	C
7	34.920	17.646	OT 081	17 49 10	09 39 45	-139.6	7.21e+18	C
8	34.920	17.646	OT 081	17 49 10	09 39 45	-112.8	1.35e+19	C
9	35.692	16.120	OT 081+	17 56 03	09 39 44	-136.1	1.45e+18	C
10	36.770	-30.134	M509+U430	20 43 41	-10 24 05	97.0	2.71e+19	GCP?
11	39.621	-39.493	PKS 2128-12-	21 22 14	-12 20 18	-222.9	1.07e+18	GCN
12	40.286	22.672	MC 1745+163-	17 39 03	16 20 13	-186.5	2.13e+18	C
13	40.286	22.672	MC 1745+163-	17 39 03	16 20 13	-140.0	2.55e+18	C
14	40.286	22.672	MC 1745+163-	17 39 03	16 20 13	-102.0	1.57e+19	C
15	41.703	19.652	MC 1745+163+	17 52 48	16 20 13	-136.7	2.50e+18	C
16	41.703	19.652	MC 1745+163+	17 52 48	16 20 13	-118.3	1.52e+19	C
17	41.997	22.146	MC3 1750+17-	17 43 41	17 34 58	-115.8	1.73e+18	C
18	42.691	20.641	MC3 1750+17	17 50 33	17 34 59	-110.7	8.96e+18	C
19	43.386	19.139	MC3 1750+17+	17 57 26	17 34 59	-116.0	4.98e+18	C
20	43.513	-29.793	MS 20532-50	20 53 16	-05 03 11	-222.4	1.73e+19	GCN
21	44.474	-31.289	MS 20532-50+	21 00 08	-05 03 10	-197.5	2.02e+18	GCN
22	47.163	-78.129	PKS 0005-239-	23 58 35	-23 55 58	-84.1	1.59e+19	MS
23	47.194	29.699	V 396 Her	17 20 37	24 39 06	-147.2	1.09e+18	C
24	47.773	28.222	V 396 Her+	17 27 30	24 39 06	-153.5	1.11e+19	C
25	47.773	28.222	V 396 Her+	17 27 30	24 39 06	-105.9	2.03e+18	C
26	48.778	23.076	PKS 1756+237-	17 50 03	23 43 57	-122.5	5.41e+18	C
27	49.395	21.610	PKS 1756+237	17 56 56	23 43 55	-123.5	3.78e+18	C
28	50.019	20.150	PKS 1756+237+	18 03 48	23 43 58	-111.0	2.27e+19	C
29	50.039	-79.599	PKS 0005-239	00 05 27	-23 55 59	-112.4	6.24e+19	MS

Table 4—Continued

	ℓ	b	Name	α (B1950)	δ (B1950)	V_{pk}	N_{HI}	Complex
	(deg)	(deg)				(km s ⁻¹)	(cm ⁻²)	
(1)	(2)	(3)	(4)	(5)	(6)	(7)	(8)	(9)
30	53.723	-81.042	PKS 0005-239+	00 12 19	-23 55 59	-123.3	5.21e+19	MS
31	55.473	-35.577	PKS 2134+004	21 34 05	00 28 26	114.1	1.55e+18	GCP
32	56.865	-33.617	RXJ 2139+02-	21 30 20	02 32 28	-285.7	1.48e+18	GCN
33	57.751	33.568	B2 1721+34-	17 14 40	34 20 42	-142.3	8.33e+18	C
34	58.087	-35.006	RXJ 21397+02	21 37 12	02 32 28	-223.1	5.45e+17	GCN
35	62.404	13.082	3C 395-	18 54 10	31 55 14	-108.6	7.39e+19	R/OA
36	63.028	11.757	3C 395	19 01 02	31 55 13	-127.5	1.68e+19	R/OA
37	63.668	10.441	3C 395+	19 07 54	31 55 14	-122.6	2.86e+19	R/OA
38	63.698	39.555	1641.7+399+	16 48 37	39 58 47	-118.8	2.13e+18	C
39	71.265	25.883	OU 401+	18 06 56	44 04 19	-118.5	5.79e+18	C
40	74.301	35.975	PG 1718+481-	17 11 25	48 07 12	-154.6	4.14e+18	C
41	74.375	34.829	PG 1718+481	17 18 17	48 07 11	-132.2	6.30e+18	C
42	74.478	33.686	PG 1718+481+	17 25 10	48 07 11	-193.5	1.46e+18	C
43	74.478	33.686	PG 1718+481+	17 25 10	48 07 11	-124.0	2.44e+18	C
44	76.904	34.190	4C50.43-	17 22 57	50 09 45	-165.8	2.48e+18	C
45	76.904	34.190	4C50.43-	17 22 57	50 09 45	-125.9	1.53e+18	C
46	76.908	24.601	3C 380.0-	18 21 21	48 42 41	-117.3	5.61e+19	C
47	76.990	33.092	4C50.43	17 29 49	50 09 45	-127.8	6.76e+18	C
48	77.009	52.591	PKS 1538+477-	15 31 08	47 45 17	-167.1	2.19e+18	C
49	77.104	31.996	4C50.43+	17 36 41	50 09 43	-98.9	1.57e+19	C
50	77.225	23.505	3C 380.0	18 28 13	48 42 39	-110.8	1.02e+20	C/OA
51	77.564	22.415	3C 380.0+	18 35 06	48 42 42	-105.8	1.02e+20	C/OA
52	77.564	22.415	3C 380.0+	18 35 06	48 42 42	-209.5	3.16e+18	D
53	77.944	31.029	IRAS 1750+50-	17 43 12	50 46 23	-147.2	5.16e+18	C
54	77.944	31.029	IRAS 1750+50-	17 43 12	50 46 23	-114.0	1.89e+19	C
55	78.099	29.950	IRAS 1750+50	17 50 05	50 46 21	-157.1	1.67e+18	C
56	78.280	28.876	IRAS 1750+50+	17 56 57	50 46 21	-139.8	6.08e+18	C
57	78.455	-50.230	PG 2302+029	23 02 12	02 55 35	-324.3	3.26e+18	MS
58	78.529	-44.471	PKS 2254+074-	22 47 54	07 27 12	-328.2	2.29e+18	MS

Table 4—Continued

	ℓ	b	Name	α (B1950)	δ (B1950)	V_{pk}	N_{HI}	Complex
	(deg)	(deg)				(km s ⁻¹)	(cm ⁻²)	
(1)	(2)	(3)	(4)	(5)	(6)	(7)	(8)	(9)
59	78.977	36.712	PG 1700+518+	17 07 05	51 53 38	-181.3	1.64e+18	C
60	78.977	36.712	PG 1700+518+	17 07 05	51 53 38	-132.9	1.48e+18	C
61	79.020	37.771	PG 1700+518	17 00 13	51 53 38	-158.2	1.27e+18	C
62	79.020	37.771	PG 1700+518	17 00 13	51 53 38	-132.8	5.34e+17	C
63	79.097	38.830	PG 1700+518-	16 53 21	51 53 39	-169.2	1.42e+18	C
64	79.097	38.830	PG 1700+518-	16 53 21	51 53 39	-130.0	1.80e+18	C
65	80.425	-45.521	PKS 2254+074	22 54 46	07 27 11	-336.0	8.31e+18	MS
66	80.425	-45.521	PKS 2254+074	22 54 46	07 27 11	-269.2	6.42e+17	MS
67	80.600	-51.280	PG 2302+029+	23 09 04	02 55 34	-321.0	4.96e+18	MS
68	80.600	-51.280	PG 2302+029+	23 09 04	02 55 34	-262.8	2.11e+18	MS
69	80.966	35.410	PG 1715+535	17 15 31	53 31 25	-130.6	1.02e+19	C
70	80.967	34.390	PG 1715+535+	17 22 23	53 31 27	-119.2	4.65e+19	C
71	80.978	-40.937	PKS 2251+11-	22 44 48	11 20 40	-337.9	1.54e+18	MS
72	80.997	36.431	PG 1715+535-	17 08 38	53 31 26	-100.0	9.48e+18	C
73	81.711	-29.095	PKS 2223+21-	22 16 22	21 02 51	-405.2	3.25e+18	MS*
74	81.817	-29.306	MS 22241+20-	22 17 15	20 56 29	-408.8	3.82e+18	MS*
75	82.114	16.609	4C 50.47-	19 17 56	50 46 52	-190.0	5.03e+18	D
76	82.114	16.609	4C 50.47-	19 17 56	50 46 52	-115.8	3.75e+19	OA
77	82.398	-46.534	PKS 2254+074+	23 01 38	07 27 11	-338.2	9.66e+17	MS
78	82.502	-60.190	PKS 2340-036-	23 33 30	-03 39 05	-266.2	1.12e+19	MS
79	82.502	-60.190	PKS 2340-036-	23 33 30	-03 39 05	-210.8	1.64e+18	MS
80	82.571	15.615	4C 50.47	19 24 49	50 46 54	-114.5	3.25e+19	OA
81	82.783	-41.940	PKS 2251+11	22 51 40	11 20 40	-362.7	5.28e+18	MS
82	83.046	14.631	4C 50.47+	19 31 41	50 46 52	-116.0	3.77e+19	OA
83	83.119	12.405	Tex 1951+498-	19 44 20	49 50 25	-119.4	6.49e+19	OA
84	83.160	-30.087	PKS 2223+21	22 23 15	21 02 53	-405.8	1.34e+18	MS*
85	83.273	-30.296	MS 22241+20	22 24 07	20 56 29	-416.1	1.23e+18	MS*
86	83.662	11.433	Tex 1951+498	19 51 12	49 50 24	-118.4	6.97e+19	OA
87	83.889	-39.196	PKS2247+14	22 47 56	14 03 58	-379.4	8.95e+18	MS

Table 4—Continued

	ℓ	b	Name	$\alpha(\text{B1950})$	$\delta(\text{B1950})$	V_{pk}	N_{HI}	Complex
	(deg)	(deg)				(km s^{-1})	(cm^{-2})	
(1)	(2)	(3)	(4)	(5)	(6)	(7)	(8)	(9)
88	84.223	10.472	Tex 1951+498+	19 58 04	49 50 24	-115.5	8.11e+19	OA
89	84.445	-37.281	3C 454.3-	22 44 51	15 52 56	-428.2	6.17e+17	MS
90	84.445	-37.281	3C 454.3-	22 44 51	15 52 56	-395.9	1.39e+18	MS
91	84.447	-44.591	4C 09.72-	23 01 54	09 51 59	-105.1	8.86e+17	GCN?
92	84.447	-44.591	4C 09.72-	23 01 54	09 51 59	-440.5	3.98e+17	MS
93	84.653	-42.905	PKS 2251+11+	22 58 34	11 20 41	-349.7	2.94e+18	MS
94	85.401	-61.151	PKS 2340-036	23 40 22	-03 39 04	-300.9	3.13e+18	MS
95	85.401	-61.151	PKS 2340-036	23 40 22	-03 39 04	-246.5	3.99e+18	MS
96	85.673	-40.140	PKS 2247+14+	22 54 49	14 03 58	-376.1	2.71e+18	MS
97	85.842	67.292	1411+422-	14 04 58	44 14 25	-99.5	1.00e+18	
98	86.450	-45.521	4C 09.72	23 08 46	09 51 59	-351.0	9.41e+17	MS
99	87.826	-39.050	3C 454.3+	22 58 08	15 52 56	-377.9	1.64e+18	MS
100	88.472	-62.049	PKS 2340-036+	23 47 15	-03 39 05	-284.8	1.66e+18	MS
101	88.472	-62.049	PKS 2340-036+	23 47 15	-03 39 05	-235.6	2.05e+18	MS
102	88.659	-59.534	PKS 2349-01-	23 42 30	-01 25 53	-296.2	6.14e+18	MS
103	89.951	35.580	3C 351+	17 10 42	60 48 32	-177.6	7.66e+18	C
104	89.951	35.580	3C 351+	17 10 42	60 48 32	-139.5	2.70e+18	C
105	90.084	36.382	3C 351	17 04 03	60 48 31	-182.2	4.19e+18	C
106	90.084	36.382	3C 351	17 04 03	60 48 31	-128.2	6.01e+18	C
107	90.084	36.382	3C 351	17 04 03	60 48 31	-83.0	4.08e+18	C
108	90.245	37.181	3C 351-	16 57 25	60 48 30	-154.7	1.27e+19	C
109	90.245	37.181	3C 351-	16 57 25	60 48 30	-90.6	3.42e+18	C
110	91.665	-60.361	PKS 2349-01	23 49 22	-01 25 52	-302.2	9.66e+17	MS
111	92.211	-60.618	UM 186	23 50 48	-01 32 08	-312.5	1.54e+18	MS
112	95.100	-49.445	PKS 2344+09-	23 37 11	09 14 07	-346.0	6.92e+18	MS
113	95.100	-49.445	PKS 2344+09-	23 37 11	09 14 07	-309.2	5.09e+18	MS
114	97.503	-50.131	PKS 2344+09	23 44 04	09 14 07	-374.6	3.67e+18	MS
115	97.503	-50.131	PKS 2344+09	23 44 04	09 14 07	-332.4	6.60e+17	MS
116	99.477	-55.038	UM 18-	23 55 54	05 07 30	-343.8	8.34e+17	MS

Table 4—Continued

	ℓ	b	Name	$\alpha(\text{B1950})$	$\delta(\text{B1950})$	V_{pk}	N_{HI}	Complex
	(deg)	(deg)				(km s^{-1})	(cm^{-2})	
(1)	(2)	(3)	(4)	(5)	(6)	(7)	(8)	(9)
117	99.477	-55.038	UM 18-	23 55 54	05 07 30	-299.5	1.51e+18	MS
118	102.578	36.115	PG 1634+706+	16 41 44	70 37 35	-160.0	5.75e+18	C
119	102.688	-32.577	3C 463+	23 32 20	26 59 23	-438.1	1.14e+18	MS*
120	102.843	36.644	PG 1634+706	16 34 52	70 37 39	-158.6	6.81e+18	C
121	103.127	37.166	PG 1634+706-	16 27 59	70 37 36	-161.7	4.74e+18	C
122	104.270	49.251	S4 1435+63+	14 42 29	63 49 36	-117.2	1.96e+19	C
123	105.175	49.729	S4 1435+63	14 35 37	63 49 38	-120.0	9.29e+18	C
124	105.354	24.409	4C 73.18-	19 15 49	73 51 47	-111.3	1.50e+19	OA
125	105.626	23.541	4C 73.18	19 28 49	73 51 47	-121.6	2.52e+19	OA
126	105.946	22.687	4C 73.18+	19 41 49	73 51 47	-125.9	2.72e+19	OA
127	106.117	50.184	S4 1435+63-	14 28 45	63 49 38	-138.0	8.97e+18	C
128	107.318	-45.325	PKS 0003+15	00 03 25	15 53 08	-326.9	9.84e+17	MS*
129	108.141	-19.651	B3 2327+407+	23 34 35	40 47 52	-131.9	3.10e+18	G
130	108.973	41.423	3C 309+	15 11 57	71 52 09	-141.6	4.58e+18	C
131	109.983	42.097	3C 309	14 58 56	71 52 12	-141.8	1.17e+19	C
132	110.181	-33.065	B2 2353+28+	00 00 14	28 19 16	-116.2	1.05e+18	
133	110.778	51.711	1351+640+	13 58 40	64 00 28	-157.3	2.34e+19	C
134	110.778	51.711	1351+640+	13 58 40	64 00 28	-116.3	1.23e+19	C
135	111.061	42.721	3C 309-	14 45 56	71 52 11	-135.1	9.47e+18	C
136	111.890	52.020	1351+640	13 51 47	64 00 28	-156.0	4.08e+19	C
137	111.890	52.020	1351+640	13 51 47	64 00 28	-123.0	1.44e+19	C
138	112.965	-12.341	4C 49.48-	23 48 45	49 05 03	-357.5	7.89e+17	(EN)
139	112.965	-12.341	4C 49.48-	23 48 45	49 05 03	-180.4	1.03e+19	G
140	113.030	52.299	1351+640-	13 44 55	64 00 29	-158.7	2.70e+19	C
141	113.030	52.299	1351+640-	13 44 55	64 00 29	-121.9	1.89e+19	C
142	113.861	-21.220	4C 40.01-	00 04 02	40 34 58	-402.0	8.52e+17	MS?/EN
143	114.089	-12.592	4C 49.48	23 55 37	49 05 03	-186.0	8.95e+18	G
144	115.219	-12.813	4C 49.48+	00 02 29	49 05 04	-190.0	1.08e+19	G
145	116.926	-58.539	PG 0043+039-	00 36 18	03 54 44	-355.6	1.02e+19	MS?/EN

Table 4—Continued

	ℓ	b	Name	$\alpha(\text{B1950})$	$\delta(\text{B1950})$	V_{pk}	N_{HI}	Complex
	(deg)	(deg)				(km s^{-1})	(cm^{-2})	
(1)	(2)	(3)	(4)	(5)	(6)	(7)	(8)	(9)
146	117.050	26.469	IRAS 1910+84+	19 23 24	84 36 54	-132.7	1.95e+18	OA
147	117.721	-39.980	NAB 0024+22+	00 31 31	22 25 23	-130.9	1.61e+18	
148	118.965	57.964	PG 1259+593+	13 05 46	59 18 16	-122.9	4.10e+19	C
149	120.207	-58.656	PG 0043+039	00 43 11	03 54 42	-367.8	1.64e+18	MS?/EN
150	120.556	58.048	PG 1259+593	12 59 08	59 18 15	-127.7	5.84e+19	C
151	121.734	-33.440	B2 0051+29-	00 44 10	29 08 53	-319.5	1.15e+18	Wr
152	122.156	58.090	PG 1259+593-	12 52 30	59 18 16	-117.0	1.95e+19	C
153	123.532	-33.450	B2 0051+29	00 51 02	29 08 54	-336.7	1.50e+18	Wr
154	123.532	-33.450	B2 0051+29	00 51 02	29 08 54	-291.4	4.07e+17	Wr
155	123.532	-33.450	B2 0051+29	00 51 02	29 08 54	-163.0	6.96e+17	(EN)
156	124.371	41.768	MARK 205+	12 32 33	75 35 18	-206.5	6.69e+17	C
157	124.779	56.589	SBS 1234+607+	12 40 58	60 47 01	-144.3	2.09e+19	C
158	124.779	56.589	SBS 1234+607+	12 40 58	60 47 01	-116.2	1.29e+19	C
159	125.329	-33.412	B2 0051+29+	00 57 54	29 08 54	-397.4	1.84e+18	Wr
160	125.329	-33.412	B2 0051+29+	00 57 54	29 08 54	-349.4	1.95e+18	Wr
161	125.420	-60.492	UM 301-	00 53 46	02 05 07	-123.6	7.90e+17	
162	125.447	41.673	MARK 205	12 19 33	75 35 15	-207.5	1.16e+19	C
163	125.447	41.673	MARK 205	12 19 33	75 35 15	-202.2	1.04e+19	C
164	126.296	56.521	SBS 1234+607	12 34 06	60 47 00	-125.8	2.17e+19	C
165	126.510	41.522	MARK 205-	12 06 33	75 35 17	-199.3	2.77e+18	C
166	126.815	-32.785	B2 0110+29-	01 03 46	29 42 22	-368.7	1.14e+19	Wr
167	127.801	56.413	SBS 1234+607-	12 27 14	60 47 01	-125.1	1.61e+19	C
168	128.582	-32.659	B2 0110+29	01 10 38	29 42 24	-386.7	2.52e+19	Wr
169	128.892	-60.382	UM 301	01 00 38	02 05 07	-239.6	8.45e+18	
170	129.706	-41.016	PG 0117+213-	01 10 42	21 18 06	-107.5	1.67e+18	
171	130.341	-32.487	B2 0110+29+	01 17 31	29 42 25	-392.9	3.41e+19	Wr
172	131.106	-30.219	MARK 992	01 22 00	31 51 45	-491.8	3.39e+17	real?
173	131.106	-30.219	MARK 992	01 22 00	31 51 45	465.3	3.70e+17	real?
174	131.692	53.431	4C 63.15+	12 02 57	63 11 11	-148.1	3.03e+19	C

Table 4—Continued

	ℓ	b	Name	α (B1950)	δ (B1950)	V_{pk}	N_{HI}	Complex
	(deg)	(deg)				(km s ⁻¹)	(cm ⁻²)	
(1)	(2)	(3)	(4)	(5)	(6)	(7)	(8)	(9)
175	132.040	28.982	3C 184+	07 42 23	81 52 43	-121.1	7.18e+17	A?
176	132.146	28.069	3C 184-	07 16 23	81 52 43	-178.9	9.21e+17	A
177	132.146	28.069	3C 184-	07 16 23	81 52 43	-123.7	9.08e+17	A?
178	132.770	-29.982	MARK 992+	01 28 52	31 51 45	-269.7	2.23e+18	(EN)
179	132.770	-29.982	MARK 992+	01 28 52	31 51 45	-187.2	7.41e+17	(EN)
180	132.921	53.185	4C 63.15	11 56 04	63 11 10	-145.1	1.15e+19	C
181	133.062	20.571	S5 0437+78-	04 31 08	78 33 23	-117.7	5.87e+19	OA?
182	133.205	50.017	3C 263.0+	11 43 47	66 04 27	-152.1	3.33e+18	C
183	133.205	50.017	3C 263.0+	11 43 47	66 04 27	-117.5	4.09e+18	C
184	133.285	20.840	S5 0437+78	04 38 00	78 33 24	-119.6	8.34e+19	OA?
185	133.501	21.115	S5 0437+78+	04 44 53	78 33 21	-119.1	9.88e+19	OA?
186	133.625	22.734	MS 05217+79-	05 14 52	79 18 38	-193.5	2.35e+19	A
187	133.625	22.734	MS 05217+79-	05 14 52	79 18 38	-118.2	2.59e+19	OA?
188	133.783	23.018	MS 05217+79	05 21 44	79 18 40	-180.4	2.08e+19	A
189	133.783	23.018	MS 05217+79	05 21 44	79 18 40	-114.0	1.73e+19	OA?
190	133.933	23.305	MS 05217+79+	05 28 37	79 18 39	-161.5	2.40e+19	A
191	134.124	52.906	4C 63.15-	11 49 12	63 11 10	-142.7	8.15e+18	C
192	134.159	49.743	3C 263.0	11 37 09	66 04 29	-171.6	2.93e+18	C
193	134.159	49.743	3C 263.0	11 37 09	66 04 29	-137.7	1.14e+18	C
194	134.159	49.743	3C 263.0	11 37 09	66 04 29	-110.1	9.23e+17	C
195	134.904	-22.642	TEX 0145+386	01 45 26	38 39 11	-161.3	1.62e+18	H?
196	135.091	49.446	3C 263.0-	11 30 31	66 04 29	-173.1	3.95e+18	C
197	135.091	49.446	3C 263.0-	11 30 31	66 04 29	-125.6	2.80e+18	C
198	136.311	-22.309	TEX 0145+386+	01 52 19	38 39 11	-160.0	4.20e+18	H?
199	136.901	-37.084	PKS 0130+24+	01 37 31	24 12 20	-109.6	1.41e+18	
200	140.416	27.499	MARK 380-	07 06 37	74 33 27	-195.7	3.58e+19	A
201	140.416	27.499	MARK 380-	07 06 37	74 33 27	-128.6	1.03e+19	A
202	140.441	27.956	MARK 380	07 13 29	74 33 27	-193.1	3.95e+19	A
203	140.441	27.956	MARK 380	07 13 29	74 33 27	-165.9	3.69e+19	A

Table 4—Continued

	ℓ	b	Name	α (B1950)	δ (B1950)	V_{pk}	N_{HI}	Complex
	(deg)	(deg)				(km s^{-1})	(cm^{-2})	
(1)	(2)	(3)	(4)	(5)	(6)	(7)	(8)	(9)
204	140.452	28.414	MARK 380+	07 20 22	74 33 28	-190.0	6.61e+19	A
205	140.452	28.414	MARK 380+	07 20 22	74 33 28	-171.0	5.12e+19	A
206	140.614	60.391	PG 1148+549	11 48 42	54 54 16	-112.6	1.43e+18	M/C
207	141.792	30.169	MARK 1413-	07 45 04	73 19 07	-149.9	8.58e+18	A
208	141.792	30.169	MARK 1413-	07 45 04	73 19 07	-110.7	1.28e+18	A
209	143.817	50.920	4C 61.20+	10 56 15	61 41 18	-117.8	5.31e+17	C
210	145.656	49.790	4C 61.20-	10 42 30	61 41 19	-155.3	1.70e+18	C/A
211	154.432	35.521	4CP 62.12+	08 28 15	62 07 17	-171.4	4.10e+19	A
212	154.556	34.724	4CP 62.12	08 21 23	62 07 17	-162.3	6.16e+18	A
213	154.652	33.925	4CP 62.12-	08 14 30	62 07 17	-186.1	2.71e+18	A
214	158.265	49.512	MARK 132+	10 05 00	55 09 06	-131.4	2.21e+18	A
215	158.717	-34.502	MS 02448+192+	02 51 44	19 28 24	-311.7	1.76e+18	ACVHV
216	158.717	-34.502	MS 02448+192+	02 51 44	19 28 24	-266.0	8.22e+17	ACVHV
217	158.904	48.624	MARK 132	09 58 08	55 09 07	-147.3	4.16e+18	A
218	159.490	47.723	MARK 132-	09 51 15	55 09 05	-147.9	8.06e+18	A
219	160.121	-54.037	NAB 0205+02+	02 12 07	02 28 44	-90.9	1.38e+19	ACHV
220	161.686	10.298	3C 147	05 38 43	49 49 46	-121.2	3.98e+19	OA
221	162.250	11.258	3C 147+	05 45 36	49 49 44	-115.2	2.30e+19	OA
222	165.708	-64.497	KUV 0150-074+	01 57 34	-07 43 41	-111.1	1.10e+18	
223	165.891	-66.005	KUV 0201-08-	01 54 05	-08 58 11	-138.6	2.83e+18	
224	167.198	43.088	NGC 2841 UB3-	09 11 42	51 11 19	-113.2	1.91e+18	A
225	169.802	-68.403	3C 57-	01 52 38	-11 46 59	-153.5	1.18e+18	
226	173.315	42.114	US 2068+	09 02 52	46 49 00	-116.9	4.41e+17	A
227	178.342	-31.761	MS 03574+104-	03 50 35	10 46 47	-160.6	6.05e+17	ACVHV
228	178.641	54.178	4C 41.21	10 07 26	41 47 24	-110.2	1.09e+18	M
229	178.998	52.959	4C 41.21-	10 00 48	41 47 24	-97.0	2.21e+18	M
230	179.491	52.939	PKS 0953+415+	10 00 26	41 30 00	-97.0	1.73e+18	M
231	179.648	-30.496	MS 03574+104	03 57 27	10 46 48	-243.6	3.45e+18	ACVHV
232	180.909	58.117	B3 1019+397+	10 26 33	39 47 02	-100.8	1.51e+19	M

Table 4—Continued

	ℓ	b	Name	$\alpha(\text{B1950})$	$\delta(\text{B1950})$	V_{pk}	N_{HI}	Complex
	(deg)	(deg)				(km s^{-1})	(cm^{-2})	
(1)	(2)	(3)	(4)	(5)	(6)	(7)	(8)	(9)
233	180.912	-29.214	MS 03574+104+	04 04 19	10 46 47	-244.8	3.22e+18	ACVHV
234	181.380	56.821	B3 1019+397	10 19 40	39 47 03	-102.7	1.85e+19	M
235	187.344	38.209	CSO 199+	08 45 00	35 55 21	106.9	1.73e+18	
236	188.255	36.578	TON 951-	08 37 56	34 56 11	-105.3	6.68e+17	
237	188.852	39.355	TON 951+	08 51 12	34 56 11	119.5	1.45e+18	
238	189.299	-28.752	3C 120-	04 23 53	05 15 00	-210.1	7.99e+18	ACVHV
239	189.299	-28.752	3C 120-	04 23 53	05 15 00	-136.5	2.52e+18	ACHV
240	190.373	-27.397	3C 120	04 30 32	05 15 00	-205.9	1.53e+18	ACVHV
241	190.410	-6.623	4C 16.14-	05 41 33	16 35 58	-178.9	4.38e+18	ACVHV
242	191.415	-26.032	3C 120+	04 37 10	05 15 01	-183.7	1.88e+18	ACVHV
243	191.415	-26.032	3C 120+	04 37 10	05 15 01	-129.3	5.98e+18	ACHV
244	194.005	50.879	3C 232-	09 48 33	32 38 24	-117.3	2.64e+18	M
245	199.678	51.783	TON 28-	09 54 20	29 13 02	117.4	4.14e+17	
246	202.957	56.507	Ton 34	10 17 06	27 59 01	98.9	1.76e+18	
247	213.506	26.076	0830+112-	08 23 43	11 15 31	106.5	1.47e+19	WB?
248	213.506	26.076	0830+112-	08 23 43	11 15 31	111.6	3.84e+18	WB?
249	214.309	27.601	0830+112	08 30 36	11 15 31	109.1	1.13e+18	WB?
250	222.585	-33.193	PKS 0454-22+	05 00 40	-22 03 54	141.3	3.44e+18	
251	231.560	-36.138	IR 0450-2958+	04 57 25	-29 58 29	242.8	6.86e+17	
252	236.198	16.033	PKS 0837-12-	08 30 35	-12 03 53	123.6	3.88e+18	WB
253	237.172	17.430	PKS 0837-12	08 37 28	-12 03 52	110.7	1.28e+19	WB
254	238.172	18.816	PKS 0837-12+	08 44 20	-12 03 52	126.8	4.55e+18	WB
255	241.193	19.384	PKS 0859-14-	08 53 02	-14 03 36	104.9	1.27e+18	WB
256	243.339	22.044	PKS 0859-14+	09 06 47	-14 03 37	-696.1	3.84e+17	real?
257	248.032	64.274	1130+106Y-	11 24 03	11 08 59	-110.2	7.99e+17	
258	248.675	23.512	RO2.37-	09 24 27	-16 55 42	104.6	1.43e+19	WB
259	251.100	25.953	RO2.37+	09 38 12	-16 55 41	103.6	1.68e+19	WB
260	252.620	36.603	PKS 1020-103-	10 13 12	-10 22 33	163.6	6.23e+18	WA
261	252.777	22.565	PKS 0925-203+	09 32 12	-20 21 43	99.3	4.73e+18	WB

Table 4—Continued

	ℓ	b	Name	$\alpha(\text{B1950})$	$\delta(\text{B1950})$	V_{pk}	N_{HI}	Complex
	(deg)	(deg)				(km s^{-1})	(cm^{-2})	
(1)	(2)	(3)	(4)	(5)	(6)	(7)	(8)	(9)
262	254.161	37.764	PKS 1020-103	10 20 04	-10 22 33	160.2	1.42e+18	WA
263	255.757	38.898	PKS 1020-103+	10 26 56	-10 22 33	176.7	2.04e+18	WA
264	259.800	26.776	PKS 1004-217	10 04 25	-21 44 42	175.1	1.85e+18	WA/WB
265	261.171	27.806	PKS 1004-217+	10 11 17	-21 44 43	157.4	3.19e+18	WA/WB
266	265.661	22.691	PKS 1011-282	10 11 12	-28 16 30	222.4	1.69e+19	WD?
267	265.661	22.691	PKS 1011-282	10 11 12	-28 16 30	275.9	5.97e+17	WD?
268	266.685	18.527	PKS 1009-321-	10 02 49	-32 08 45	172.2	3.63e+18	WD?
269	266.685	18.527	PKS 1009-321-	10 02 49	-32 08 45	212.8	4.40e+19	WD?
270	266.975	23.602	PKS 1011-282+	10 18 04	-28 16 31	122.6	3.46e+19	WB?/WD?
271	266.975	23.602	PKS 1011-282+	10 18 04	-28 16 31	222.1	1.90e+18	WD?
272	267.901	19.417	PKS 1009-321	10 09 42	-32 08 45	202.9	2.43e+19	WD?
273	269.578	24.021	PKS 1034-29-	10 28 03	-29 18 25	152.1	1.10e+19	WD?
274	269.578	24.021	PKS 1034-29-	10 28 03	-29 18 25	228.6	6.05e+18	WD?
275	270.951	24.847	PKS 1034-29	10 34 56	-29 18 24	126.0	8.51e+18	WD
276	271.514	26.558	IRAS 1047-28-	10 41 03	-28 07 44	132.7	2.24e+18	WD
277	271.760	27.569	IRAS 1051-27-	10 44 17	-27 22 52	127.6	2.00e+18	WD
278	271.760	27.569	IRAS 1051-27-	10 44 17	-27 22 52	164.4	6.50e+18	WD?
279	272.356	25.639	PKS 1034-29+	10 41 48	-29 18 26	118.2	9.17e+18	WD
280	272.356	25.639	PKS 1034-29+	10 41 48	-29 18 26	181.5	4.38e+18	WD?
281	272.971	27.338	IRAS 1047-28	10 47 55	-28 07 44	147.6	2.09e+18	WD?
282	273.230	42.903	PKS 1127-14-	11 20 43	-14 32 52	128.2	2.58e+18	WA/W?
283	273.248	28.343	IRAS 1051-27	10 51 09	-27 22 53	97.9	2.84e+18	WD
284	273.248	28.343	IRAS 1051-27	10 51 09	-27 22 53	144.7	4.80e+18	WD?
285	274.770	29.082	IRAS 1051-27+	10 58 01	-27 22 52	92.2	5.32e+18	WD
286	274.770	29.082	IRAS 1051-27+	10 58 01	-27 22 52	129.5	4.52e+18	WD
287	276.699	24.107	PKS 1101-325-	10 54 16	-32 35 01	145.2	9.38e+18	WD
288	276.699	24.107	PKS 1101-325-	10 54 16	-32 35 01	192.1	2.50e+18	WD?
289	278.115	24.765	PKS 1101-325	11 01 08	-32 35 03	115.7	1.66e+19	WD
290	278.732	-83.709	0107-3310-	01 01 20	-33 06 04	-145.4	3.42e+18	MS

Table 4—Continued

	ℓ	b	Name	$\alpha(\text{B1950})$	$\delta(\text{B1950})$	V_{pk}	N_{HI}	Complex
	(deg)	(deg)				(km s^{-1})	(cm^{-2})	
(1)	(2)	(3)	(4)	(5)	(6)	(7)	(8)	(9)
291	279.557	25.390	PKS 1101-325+	11 08 04	-32 35 02	124.8	7.68e+18	WD
292	279.557	25.390	PKS 1101-325+	11 08 04	-32 35 02	175.8	6.36e+17	WD?
293	279.807	33.917	PKS 1117-248+	11 24 33	-24 51 40	145.8	1.24e+18	WD?
294	284.624	40.788	J 08.06-	11 50 15	-19 42 41	115.4	9.00e+17	WD?
295	286.091	60.461	PKS 1216-010	12 16 01	-01 03 14	143.3	9.89e+17	
296	292.951	21.655	PKS 1207-399-	12 00 07	-39 59 29	116.3	7.08e+18	WD
297	292.951	21.655	PKS 1207-399-	12 00 07	-39 59 29	188.1	8.56e+17	WD?
298	292.951	21.655	PKS 1207-399-	12 00 07	-39 59 29	215.6	1.01e+18	WD?
299	293.910	72.201	Q 1230+0947+	12 37 46	09 47 57	230.6	1.36e+18	
300	295.744	22.115	PKS 1207-399+	12 13 52	-39 59 28	101.5	5.74e+18	WD
301	322.227	20.923	PKS 1421-38	14 21 12	-38 13 11	119.0	1.07e+18	
302	322.227	20.923	PKS 1421-38	14 21 12	-38 13 11	169.2	9.31e+18	
303	327.910	32.954	M16.11+	14 20 57	-25 10 19	-153.7	3.91e+18	L?
304	329.480	18.299	PKS 1451-375+	14 58 10	-37 35 22	109.6	3.69e+18	
305	331.514	35.184	PKS 1435-218-	14 28 26	-21 51 55	-91.8	2.63e+18	L?
306	333.228	34.436	PKS 1435-218	14 35 18	-21 51 55	-97.1	6.94e+17	L?
307	357.052	-77.414	PKS 2352-342+	23 59 43	-34 14 37	118.5	2.71e+18	MS?
308	359.941	-76.156	PKS 2352-342	23 52 50	-34 14 37	116.0	1.19e+18	MS?
309	359.941	-76.156	PKS 2352-342	23 52 50	-34 14 37	172.3	2.04e+18	MS?

Note. — Units of right ascension are hours, minutes, and seconds, and units of declination are degrees, arcminutes, and arcseconds. Values of N_{HI} refer to the entire Gaussian even if part of it lies at $|V_{LSR}| < 100 \text{ km s}^{-1}$.

Table 5. High-velocity Gaussian Components

N_{HI} range (10^{18})	Numb. ^a	Percent ^b	ΣN_{HI} (10^{20}) ^c	% Total N_{HI} ^d
(1)	(2)	(3)	(4)	(5)
0-1	42	14	0.3	1.0
1-2	64	21	0.9	2.9
2-3	34	11	0.8	2.5
3-4	23	7	0.8	2.5
4-5	17	5	0.8	2.3
5-6	10	3	0.5	1.7
6-8	16	5	1.1	3.3
8-10	17	5	1.5	4.5
10-15	22	7	2.6	8.0
15-20	18	6	3.0	9.3
20-30	16	5	3.9	11.9
30-40	10	3	3.6	10.9
40-50	5	2	2.1	6.5
50-75	10	3	6.1	18.9
> 75	5	2	4.5	14.2

^aThe number of detected high-velocity H I lines in the particular N_{HI} range.

^bThe percentage of the total number of lines in the particular N_{HI} range.

^cThe sum of the H I column density of all lines in the given range of N_{HI} .

^dThe percentage of the total observed N_H contributed by lines in this range of N_{HI} .

Table 6. Average Velocity of HI Lines

Ref. Frame	$\langle V_{em} \rangle$ (km s ⁻¹)	$\langle V_{pk} \rangle$ (km s ⁻¹)
LSR	-109 ± 120	-118 ± 165
Gal Center	-4 ± 96	-52 ± 117
Local Group	$+15 \pm 106$	-40 ± 121

Note. — The quantity $\langle V_{em} \rangle$ is the average velocity weighted by the amount of emission at each velocity, i.e. by the value of N_{HI} . The quantity $\langle V_{pk} \rangle$ is the average velocity of the line peaks, regardless of their strength.

Table 7. Angular Structure in Low- N_{HI} Lines

Source	ℓ (deg)	V_{LSR} (km s $^{-1}$)	$N_{HI}(-, S, +)$ (10^{18} cm $^{-2}$)	$\Delta\theta$ (deg)	Complex
MC1750+17	42	-120	1.7, 9.0, 5.0	1.6	C
4C 50.43	77	-130	1.5, 6.8, 16.7	1.1	C
PKS 2254+074	80	-330	2.3, 8.3, 1.0	1.7	MS
Mrk 205	124	-206	2.8, 11.6, 0.7	0.9	C
PG 1700+518	79	-170	1.4, 1.3, 1.6	1.1	C
B2 0051+29	122	-335	1.2, 1.5, 2.0	1.5	Wr
MS03574+104	178	-240	0.4, 3.4, 3.2	1.7	ACVHV
PKS 1020-103	254	+160	6.2, 1.4, 2.0	1.7	WA

Table 8. Angular Structure in Triples

Detections	Percent
All Positions	26
Two Adjacent	16
Edge Only	49
Center Only	7
All but Center	2

Table 9. Triples with H I only at the Central Position

Object	ℓ (deg)	b (deg)	V_{LSR} (km s ⁻¹)	N_{HI} (10 ¹⁸)	Complex
PKS 2352-342	359.941	-76.156	172.3	2.0	MS?
UM 186	92.211	-60.618	-312.5	1.5	MS
PKS 1216-010	286.091	60.461	143.3	1.0	
UM 301	128.892	-60.382	-239.6	8.4	
RXJ 21397+02	58.087	-35.006	-223.1	0.5	GCN
PKS 2254+074	80.425	-45.521	-269.2	0.6	MS
OT 081	34.920	17.646	-112.8	13.5	C
4C 09.72	86.450	-45.521	-351.0	0.9	MS
PKS 0003+15	107.318	-45.325	-326.9	1.0	MS*
Ton 34	202.957	56.507	98.9	1.8	
B2 0051+29	123.532	-33.450	-291.4	0.4	Wr
B2 0051+29	123.532	-33.450	-163.0	0.7	